Characterization of the Exhaust Flow through the Diesel Oxidation Catalyst

by

Giffin Symko

A thesis submitted in partial fulfillment of the requirements for the degree of

Master of Science

Department of Mechanical Engineering
University of Alberta

Abstract

The result of adding an insulation ring to the interior of the Diesel oxidation catalyst on pressure drop and light-off characteristics is investigated by injecting a ceramic material into the channels of the monolith forming a circular ring. The steady state pressure drop is recorded as a function of the mass flow rate while the transient temperature response is recorded as a function of time. The experimental results are compared with a numerical model created using ANSYS Fluent.

The experimental results show no statistical difference in pressure drop with the addition of an insulation ring as the pulsations in the exhaust flow, created by the engine, results in uncertainty larger than the expected difference in pressure drop. The numerical model shows an increase in pressure drop that corresponds to the decrease in flow area which results in an increase in viscous resistance through the remaining channels of the monolith.

The experimental results indicate that the addition of an insulation ring increases the heat capacity of the DOC requiring more energy and time to reach steady state. However, the numerical model indicates that the increase in time to reach steady state is due to the slow rate of heating of the insulation ring, while the rate of heating of the monolith is increased, with the exception of a small area directly adjacent to the insulation ring.

The experimental results show no statistical difference in pressure drop while the numerical model indicates an increase in pressure drop with the addition of an insulation ring. The light-off characteristics of the DOC with the addition of an insulation ring may be improved as the rate of heating is increased across the monolith, with the exception of directly adjacent to the insulation ring. Whether the decrease in the rate of heating adjacent to the insulation ring offsets the benefits of the increase for the remainder of the monolith needs to be further explored.

Table of Contents

List of Tables

List of Figures

Nomenclature

Acronyms

BDC	Bottom Dead Centre
BSFC	Brake Specific Fuel Consumption
CI	Compression Ignition
CPSI	Cells per Square Inch
DEF	Diesel Exhaust Fluid
DNS	Direct Numerical Simulation
DOC	Diesel Oxidation Catalyst
DPF	Diesel Particulate Filter
EGR	Exhaust Gas Recirculation
EPA	Environmental Protection Agency
GHG	Greenhouse Gas
HC	Hydrocarbons
HCCI	Homogeneous Charge Compression Ignition
HFM	Hot Film Mass
IC	Internal Combustion
LES	Large Eddy Simulation
LNT	Lean NO_x Trap
MAF	Mass Air Flow
NHTSA	National Highway Traffic Safety Administration

NO_x	Oxides of Nitrogen
PID	Proportional Integral Derivative
PM	Particulate Matter
PPCI	Partially Premixed Compression Ignition
R	Universal Gas Constant
RANS	Reynolds Averaged Navier-Stokes
SCR	Selective Catalytic Reduction
SI	Spark Ignition
SST	Shear-Stress Transport
TDC	Top Dead Centre

Symbols

α	Permeability ($1/\alpha$ is the Viscous Resistance Factor)
α	Cut-Off Ratio
δ	Kroneker delta
ΔP	Differential pressure
ϵ	Porosity
η	Engine Efficiency
γ	Ratio of Gas Specific Heats
μ	Dynamic Viscosity
μ_{T}	Dynamic Turbulent Viscosity
ρ	Density
ω	Specific Dissipation Rate
A	Cross-Sectional Area
$C_P(T)$	Temperature dependent specific heat capacity
C_0	Discharge Coefficient
C_2	Inertial Resistance Factor
D_c	Hydraulic Diameter
d_{m}	Mean Particle Diameter
$\mathrm{h_v}$	Energy associated with Sunlight
E	Energy
$\mathrm{E_A}$	Activation Energy
f	Frequency
G_ω	Generation of Turbulent Kinetic Energy
G_k	Generation of Specific Dissipation Rate
k	Turbulence Kinetic Energy

k_{T}	Reynolds Stress Tensor
k^{+}	Forward Reaction Rate Constant
k^{-}	Backward Reaction Rate Constant
k_{eff}	Effective Thermal Conductivity
k_f	Fluid Thermal Conductivity
k_{sf}	Solid Thermal Conductivity
L	Length
$\dot{m}$	Mass Flow Rate
P	Pressure
$\dot{Q}$	Volumetric Flow Rate
r	Radius
Re	Reynolds Number
r_{v}	Compression Ratio
$\vec{S}$	Porous Zone Source Term
S	User-Defined Source Term
S_ω	User-Defined Source of Turbulent Kinetic Energy
S_k	User-Defined Source of Specific Dissipation Rate
t	Time
T	Temperature
u	Velocity
v	Kinematic Viscosity
v_{T}	Turbulent Kinematic Viscosity
V_{out}	Output Voltage
W_{power}	Work produced
W_{pump}	Pumping work
Y	Molar Concentration
Y_ω	Dissipation of Turbulent Kinetic Energy
Y_k	Dissipation of Specific Dissipation Rate

Chapter 1

Introduction

This Chapter details the problem addressed in this thesis, why it should be addressed, and how it is investigated.

1.1 Diesel Exhaust Aftertreatment

Since the 1970s, legislation governing the emissions from automobiles has become increasing stringent which has required auto manufacturers to rely on advances in aftertreatment systems to ensure compliance. Advances in combustion control strategies, such as exhaust gas recirculation and injection timing, have become insufficient at reducing tailpipe emissions to meet legislated levels of emissions, this has required auto manufacturers to rely on advances in aftertreatment devices, such as catalysts and filters, to ensure compliance of tailpipe emissions.

Aftertreatment systems for Diesel engines are often composed of two catalysts, the Diesel Oxidation Catalyst (DOC) and Selective Catalytic Reduction Catalyst (SCR), used to oxidize hydrocarbons (HC) and reduce oxides of nitrogen (NO_x). The addition of a Diesel Particulate Filter (DPF) is used in conjunction with the catalysts to remove particulate matter (PM) from the exhaust. The addition of each component reduces regulated emissions such as HC, NO_x, and PM but increases the back pressure on the engine reducing the efficiency of the engine and leading to increased fuel consumption

and increased CO_2 tailpipe emissions.

1.2 Problem Statement

The objective of this research is to characterize the flow of exhaust gas through the DOC. To understand the flow through the DOC and its effect on the DOC, a number of key aspects are observed including the pressure drop, the heating characteristics affecting the light-off temperature, and the effect of altering the internal geometry. The experimental results are compared to numerical simulations for a greater understanding of the internal flows inside the monolith and to aid in developing a numerical model of the DOC for future work.

1.3 Motivation

Governments worldwide are acting to decrease harmful emissions and decrease the amount of CO_2 produced by automotive engines, requiring manufacturers to both optimize current systems to minimize the emissions produced and to develop new methods of eliminating emissions produced by the engine. The Environmental Protection Agency (EPA) and the National Highway Traffic Safety Administration (NHTSA) have issued rules to reduce greenhouse gases (GHG) emissions for model year vehicles 2017-2025. The EPA regulations are expected to result in an average combined production of no more than 101.28 g/km (163 g/mile) of CO_2, equivalent to an average fuel consumption of 4.32 L/100 km (54.5 mpg) by the end of 2025 [EPA, 2012].

Over the last several years, efforts to achieve high efficiency combustion engines while simultaneously reducing exhaust emissions using low temperature combustion have been made. One way to do this is by taking a spark ignition (SI) engine and producing a homogeneous charge that autoignites [Yao et al., 2009] and usually requires control [Ghazimirsaied and Koch, 2012; Strandh et al., 2004; Ebrahimi and Koch,

2015]. Mazda is now implementing this technology into their production automobiles [Mazda, 2017]. Another way to achieve high efficiency and low emissions is by taking a Diesel engine and using a partially premixed charge [Manente et al., 2011]. The advances in engine technology, particularly the use of low temperature combustion, will require corresponding advances in exhaust aftertreatment technology.

By characterizing the flow through the DOC, the DOC construction can be optimized to minimize the pressure drop and improve the light-off characteristics. By decreasing the pressure drop, the back pressure on the engine is reduced improving the overall efficiency and leading to a decrease in fuel consumption. Improved light-off characteristics can lead to a significant reduction in tailpipe emissions, as it has been found that as much as 50% to 80% of emissions are produced during cold start prior to the catalyst reaching light-off temperature [Hadavi et al., 2013; Shen et al., 1999; Cho et al., 1998].

Finally, by characterizing the flow through the DOC, the results can be used to validate the numerical models. These models will provide a greater understanding of the flow characteristics and will allow for better optimization of the DOC by manufacturers and provide more efficient control of the system by the engine controller. As it is expected that auto manufacturers will meet emissions regulations through improvements in engine control and aftertreatment systems [EPA, 2012], the ability to optimize these systems is crucial to meeting regulations.

1.4 Thesis Organization

The thesis begins with the experimental results used to characterize the flow of exhaust across the DOC both with and without the addition of insulation rings in the monolith. This includes the overall pressure drop and radial temperature profile at steady state and during heating and cooling of the DOC.

The results from the numerical analysis are compared against the experimental results to determine the validity of the numerical model. The numerical model is used to determine the effect of adding an insulation ring to the monolith and to help validate the experimental results. The experimental and numerical results are compared for steady state and transient tests to determine whether any conclusions can be drawn and show the insulating ring exibits marginal improvements. The benefits or drawbacks of adding an insulation ring to the monolith are examined in detail.

1.5 Contributions

The major contributions of this study are:

- Characterizing the flow of exhaust gas through the DOC, including the pressure drop and temperature profile for various DOC configurations.
- Developing a simple 2D axisymmetric numerical model for optimizing the construction of the DOC.
- Creating a Diesel engine exhaust setup with sensors and analysis software. The engine and exhaust aftertreatment setup will be an excellent testing facility for future aftertreatment studies.

Chapter 2

Background

An overview of the topics of this thesis are discussed in the context of research in the literature.

2.1 Compression Ignition Engines

Compression ignition (CI) engines are attractive due to their higher efficiency in comparison to spark ignition (SI) engines, leading to reduced CO_2 production and fuel consumption. Despite the benefits, CI engines produce emissions that are difficult to reduce and often in quantities much greater than SI engines, including oxides of nitrogen, particulate matter, and hydrocarbons. Various strategies are employed to reduce these emissions but most increase the complexity of the system and reduce the overall efficiency.

Power in a modern CI engine is produced by drawing air into the cylinder and then compressing it, increasing the air temperature above the ignition temperature of the fuel. The fuel is then injected and ignites, further increasing the cylinder pressure and pushing the piston downward. During fuel injection, mass transfer causes the air and fuel to mix by means of diffusion and turbulence. During mixing, the fuel combusts at the interface where the mixture reaches an equivalence ratio that is within combustible limits.

CI engines are capable of much higher compression ratios as the charge is not premixed prior to compression and are therefore not subject to the same constraints as SI engines, where the charge is premixed. The theoretical engine efficiency for SI, η_{SI}, and CI, η_{CI}, engines are given by,

$$\eta_{\mathrm{SI}} = 1 - \frac{1}{{r_{\mathrm{v}}}^{\gamma-1}} \tag{2.1}$$

$$\eta_{\mathrm{CI}} = 1 - \frac{1}{{r_{\mathrm{v}}}^{\gamma-1}}\left[\frac{\alpha^{\gamma}-1}{\gamma(\alpha-1)}\right] \tag{2.2}$$

where r_{v} is the compression ratio, α is the cut-off ratio, and γ is the ratio of gas specific heats [Stone, 2012]. Comparing Equations 2.1 and 2.2, for the same compression ratio, SI engines will have a higher efficiency due to the factor in square brackets in Equation 2.2 since the cut-off ratio, α, will always fall within the range $1 < \alpha < r_{\mathrm{v}}$, making the term in square brackets always greater than one [Stone, 2012]. However, since CI engines are capable of operating at much higher compression ratios, they are typically more efficient than SI engines. This makes CI engines attractive as increased engine efficiency leads to lower CO_2 production and fuel consumption.

The main drawback of CI engines is related to the mode of combustion occuring in the cylinder. Unlike SI engines where the charge is premixed, in CI engines the charge is injected into the cylinder after the air in the cylinder has been compressed and the ignition temperature of the fuel has been exceeded. During injection a combustion interface between the air and fuel occurs since the time dependency of mass transfer limits the flame to an interface where blending results in a local equivalence ratio sufficient for combustion, with the primary mechanisms of mass transfer being diffusion and turbulence. The time dependency of mass transfer limits the maximum engine speed and is the cause for many of the emissions produced by CI engines.

Because the diffusion flame is locally rich and lean, it produces emissions associated with both, along with particulate matter and hydrocarbons [Shum-Kivan et al., 2016].

The theoretical work produced by an IC engine is related to the difference between the maximum and minimum cylinder pressures, known as the compression ratio, r_v. Equations 2.1 and 2.2 demonstrate that increasing r_v increases η and is illustrated in Figure 2.1. As the compression ratio is the difference between the maximum and minimum cylinder, the compression ratio can be altered by careful design. An increase in compression ratio from 16 to 17 for a typical Diesel engine results in a 1% increase in theoretical efficiency. This increase in efficiency over the lifecycle of a typical vehicle results in a corresponding reduction in overall fuel consumption and CO_2 emissions.

Limitations in engine design limit the maximum cylinder pressure and as a consequence limit the maximum work that can be produced by the engine. Factors that limit the maximum cylinder pressure include material properties, mechanical friction losses that increase as the cylinder pressure increases, and emissions production since NO_x, HC, CO, and PM production are all affected by cylinder pressure [MacMillan et al., 2012].

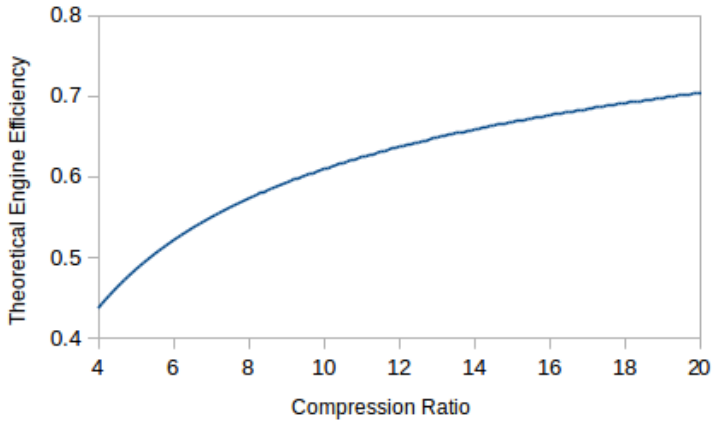

Figure 2.1: Relationship between compression ratio and theoretical engine efficiency

The minimum cylinder pressure is directly related to the downstream pressure drop from the engine to tailpipe. With the addition of catalysts and filters, the back pressure on the engine is increased. Figure 2.2 shows a 4-stroke mechanical Diesel cycle with the maximum cylinder pressure shown as $P_{\max}$, the engine out pressure as P_0, the area containing W_{power} is the power produced by the compression/expansion stroke, while the area containing W_{pump} is the pumping work required during the exhaust/intake stroke.

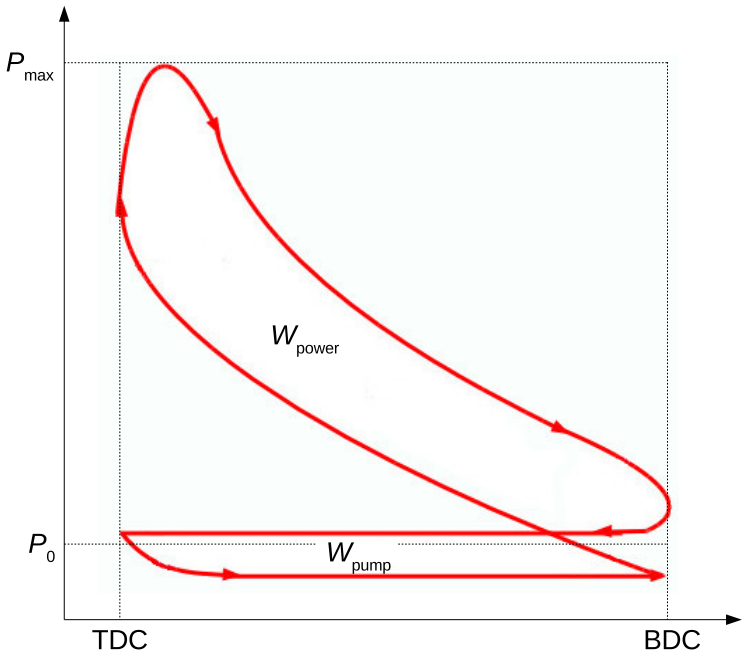

Figure 2.2: P-V diagram of a 4-stroke mechanical Diesel cycle

The addition of aftertreatment devices increases P_0 and reduces W_{power} by decreasing the compression ratio, r_{v}, calculated by $P_{\max} - P_0$, causing the area in Figure 2.2 containing W_{power} to be reduced. Furthermore, the addition of aftertreatment devices increases W_{pump} reducing the overall power output of the engine, $W_{\text{power}} - W_{\text{pump}}$. By minimizing the pressure drop between the engine and the tailpipe, the overall power output of the engine can be increased, increasing the overall engine efficiency.

2.2 Exhaust Emissions

The stoichiometric combustion of any hydrocarbon produces CO_2 and H_2O by the following reaction,

$$C_xH_y + (x + \frac{y}{2})O_2 \rightarrow xCO_2 + \frac{y}{2}H_2O \tag{2.3}$$

however the actual combustion of hydrocarbons in IC engines produce other compounds that are harmful to the environment and health as well as reduce the overall efficiency of the engine. Of particular interest are carbon monoxide (CO), particulate matter (PM), hydrocarbons (HC), and oxides of nitrogen (NO_x). Because of their negative effects, stringent government regulations are in place to limit the tailpipe emission gases produced by IC engines.

2.2.1 Carbon Monoxide

In IC engines, CO is produced primarily during rich combustion when insufficient oxygen is available for complete oxidation of the fuel. In CI engines which operate under lean conditions, the amount of CO produced is minimal and the primary source occurs when the local temperature is insufficient and the rates of reaction are too slow for oxidation to occur. This occurs in regions where the local temperature is unable to achieve high combustion temperatures, such as next to the cylinder walls which act as a heat sink [Barbosa, 2016]. CO production is an intermediate step in the production of CO_2 from a hydrocarbon and is given by,

$$RH \rightarrow R \rightarrow RO_2 \rightarrow RCHO \rightarrow RCO \rightarrow CO \tag{2.4}$$

where R is the hydrocarbon radical [Valério et al., 2003; Heywood et al., 1988]. CO is then oxidized through the following reactions,

$$\mathrm{CO} + \mathrm{OH} \underset{k_1^-}{\overset{k_1^+}{\rightleftarrows}} \mathrm{CO_2} + \mathrm{H} \tag{2.5}$$

$$\mathrm{CO_2} + \mathrm{O} \underset{k_2^-}{\overset{k_2^+}{\rightleftarrows}} \mathrm{CO} + \mathrm{O_2} \tag{2.6}$$

where k is the rate constant with the + or - indicating the forward and backwards reaction direction, respectively [Valério et al., 2003]. The rate constants can be found using the Arrnhenius equation, given by,

$$k = A\mathrm{e}^{\frac{-E_\mathrm{A}}{R_\mathrm{c}T}} \tag{2.7}$$

where A is a reaction specific constant, E_A is the activation energy, R_c is the universial gas constant, and T is the temperature. Equation 2.7 demonstrates the strong temperature dependence of Equations 2.5 and 2.6. At low temperatures the rates of reaction become negligible not allowing the reaction to progress and equilibrium to be achieved, this results in incomplete oxidation and the production of CO from the engine.

2.2.2 Oxides of Nitrogen

NO_x is produced at high temperatures during lean combustion when excess oxygen is available, increasing exponentially with temperature [Barbosa, 2016]. NO_x are toxic gases with adverse respiratory effects [WHO, 2006] and leads to the formation of smog in the atmosphere [Carpenter et al., 1998; Muilwijk et al., 2016]. Smog is produced

by photolysis of NO_2 in the presence of sunlight (h_v) through the following reactions [Heywood et al., 1988; Carpenter et al., 1998; Barbosa, 2016],

$$NO_2 \xrightarrow{h_v} NO + O \tag{2.8}$$

$$O + O_2 \longrightarrow O_3 \tag{2.9}$$

leading to the production of the ozone (O_3), which is responsible for the formation of smog.

The kinetic mechanisms by which NO_x is produced include [Barbosa, 2016],

1. thermal NO_x (also known as the extended Zeldovich mechanism)
2. prompt NO_x (also known as the Fenimore mechanism)
3. fuel NO_x

The first two mechanisms convert atmospheric nitrogen to NO_x while the last converts fuel based nitrogen to NO_x. The primary mechanism of NO_x production in IC engines is thermal NO_x, by which over 90% of all NO_x emissions are produced [Barbosa, 2016; Hernández et al., 2007]. Thermal NO_x is produced by the following three reactions [Bowman, 1975; Merryman and Levy, 1975],

$$O + N_2 \leftrightarrows NO + N \tag{2.10}$$

$$N + O_2 \leftrightarrows NO + O \tag{2.11}$$

$$N + OH \leftrightarrows NO + H \tag{2.12}$$

The rates of reaction are strongly temperature dependent, with temperatures greater than 2200 K required for reactions to proceed [Barbosa, 2016]. At high temperatures, production is favoured while at low temperatures the reverse reactions are favoured. Since the rates of reaction are too small for the reaction to proceed at low temperatures the NO produced during cylinder peak temperatures remain as the temperature drops during the expansion stroke.

The $(NO_2)/(NO)$ ratio produced in IC engines is typically very small [Bowman, 1975], however some studies have shown that NO_2 can account for up to 30% of the NO_x emissions [Hilliard and Wheeler, 1979]. Despite NO being formed in much greater quantities than NO_2, NO is oxidised at low temperatures to NO_2 resulting in nearly all NO emissions being converted to NO_2 in the environment after being exhausted [Stone, 2012].

2.2.3 Hydrocarbons

Hydrocarbons (HC) are the result of the incomplete combustion of fuel. It has been found that many of the HC found in the exhaust are not present in the fuel, which indicates that the fuel undergoes cracking and synthesis occuring during the high cylinder temperatures during compression and combustion [Bowman, 1975]. Not all HC emissions are harmful since some are inert, however, some of the HC emissions lead to photochemical reactions causing smog, others are potent greenhouse gases (methane), while others are directly toxic to human health [Pachauri et al., 2014; Andrews et al., 2007; Bowman, 1975].

HC emissions from IC engines are often produced during rich combustion where all of the fuel fails to combust, but since CI engines operate lean, HC emissions tend to be minimal [Barbosa, 2016]. HC emissions from CI engines tend to be the result of three sources [Heywood et al., 1988]:

- undermixing
- quenching
- absorption/desorption.

HC emissions from undermixing occur when the fuel inadequately mixes during injection resulting in locally rich regions where the fuel fails to mix during combustion. One main source of undermixing is the result of fuel remaining in the injector nozzle sac and vaporizing after the cylinder pressure drops and the exhaust valve opens. HC emissions from quenching occur when fuel reaches areas where the temperature is insufficient for combustion and the flame is quenched. HC emissions from quenching occur along the cylinder walls or between the cylinder and piston where the space is too small for the flame to propagate [Bowman, 1975]. Finally, emissions from absorption/desorption occur as a result of hydrocarbons absorbing into the engine oil at high pressure when the piston is near top dead centre (TDC) and desorbing as the pressure drops and the piston nears bottom dead centre (BDC).

2.2.4 Particulate Matter

From Diesel engines, PM is composed primarily of carbanaceous material with attached organic molecules, known as black carbon [Bond et al., 2013; Heywood et al., 1988]. PM has been linked to an increased risk of cardiopulmonary mortality and long term chronic health problems [Pope III and Dockery, 2006; WHO et al., 2012]. It has been found that even increases as small as 50 μg/m^3 were found to increase mortality by 2% to 4% [Künzli et al., 2000; Katsouyanni et al., 1997]. Furthermore, the effect of black carbon on climate change is significant as it absorbs more sunlight than it reflects, leading to increased atmospheric temperatures [Bond et al., 2013].

PM is the result of incomplete combustion in locally rich areas where insufficient oxygen is available. Particulate matter varies in composition containing 50% to 90%

carbon along with other components including oxygen, sulphur, phosphorous, iron, calcium, and zinc, depending on availability during PM formation [Clague et al., 1999].

The formation of PM is a two step process; nucleation and agglomeration [Dhal et al., 2017]. Nucleation occurs with the formation of an aromatic ring structure at high temperature, as the hydrogen bonds are broken, leaving carbon chains. The carbon chains then undergo polycyclic aromatic ring growth which results in particle nucleation [Dhal et al., 2017; Heywood et al., 1988]. The particles then grow primarily by surface growth involving the attachment of available gas phase particles and through agglomeration where individual soot particles collide [Dhal et al., 2017].

Once PM enters into the atmostphere, Leung et al. [2017] have shown its growth to occur in three phases. In the first phase the density of the particles increases due to surface growth of secondary organic aerosols while the shape of the black carbon/soot remains unchanged. The second stage involves soot restructuring while surface growth of the particle continues with the addition of secondary organic aerosols. The third stage involves continued growth of the particle while the shape of the particle tends towards becoming spherical [Leung et al., 2017]. The coating on the particle continues to grow while the shape of the particle continues to restructure until the particle becomes nearly spherical with a shape factor approaching one [Ghazi and Olfert, 2013].

Coating black carbon with organic components has an important effect on climate forcing, increasing the radiative absorption of black carbon by up to a factor of 2 [Cappa et al., 2012]. The increase in radiative absorption is a result of the organic coating refracting sunlight towards the black carbon core, increasing the effective absorptive area of the particle [Bond and Bergstrom, 2006] and increasing the energy absorbed.

2.3 Control of Engine Emissions

Control of tailpipe emissions from Diesel engines is difficult and involves numerous strategies and additional equipment. Strategies can be divided into two broad categories; combustion control strategies and exhaust aftertreatment strategies. Combustion control strategies involve limiting the cylinder conditions that result in the production of emissions, for example, controlling injection timing, rate of fuel injection, and exhaust gas recirculation (EGR) [Barbosa, 2016]. A number of low temperature combustion strategies exist that attempt to reduce the cylinder pressure and temperature to minimize emission production and include homogeneous charge compression ignition (HCCI) [Price et al., 2007] and partially premixed compression ignition (PPCI) [Noehre et al., 2006]. However, decreasing one emission often results in an inadvertent increase in another, resulting in a tradeoff between two emissions [Barbosa, 2016]. For example, EGR decreases NO_x emissions by reducing the peak cylinder temperature but also causes an increase in PM due to the decrease in available oxygen and decrease in temperature.

To meet emission regulations, combustion control strategies need ultimately be combined with exhaust aftertreatment strategies. Aftertreatment strategies include the use of catalysts and filters to reduce or eliminate specific components in the exhaust. The drawback of using aftertreatment strategies is the increase in back pressure on the engine which results in a decrease in engine efficiency and increase in fuel consumption.

2.4 Diesel Exhaust Aftertreatment

The typical CI engine relies on multiple catalysts and a filter to reduce engine-out emissions to meet tailpipe emission regulations. This is unlike SI engines which are capable of meeting tailpipe emissions regulations with the use of a single three-way

catalyst. A typical exhaust setup for a CI engine will include a Diesel Oxidation Catalyst (DOC) to reduce HC emissions, Selective Catalytic Reduction (SCR) catalyst or Lean NO_x Trap (LNT) to reduce NO_x emissions, and Diesel Particulate Filter (DPF) to reduce PM emissions. Figure 2.3 is the schematic for a 2015 6.7L Ford F-150 Diesel pickup and is representative of the aftertreatment system used on the majority of vehicles with a CI engine [Ford Motor Company, 2014].

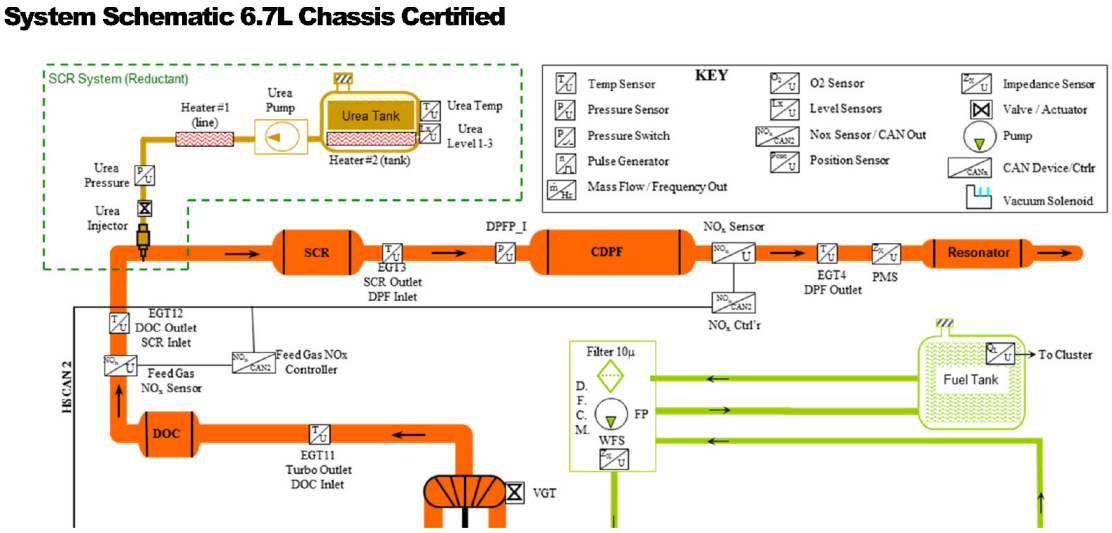

Figure 2.3: Exhaust aftertreatment schematic for a 6.7L Ford F-150 Diesel pickup

Catalysts and filters are complex, expensive, and require multiple sensors for monitoring and control. In addition to the increased cost and complexity, the addition of aftertreatment systems increases the overall pressure drop from engine to tailpipe and leads to an increase in back pressure on the engine. An increase in back pressure leads directly to a reduction in engine efficiency, an increase in fuel consumption, and an increase in CO_2 production.

2.4.1 Diesel Particulate Filter

One of the greatest challenges in the design of IC engines is effectively reducing PM to meet emissions regulations. Engine control strategies have become insufficient at reducing PM making aftertreatment strategies necessary. The addition of a DPF to the aftertreatment system is an effective way of reducing tailpipe PM emissions, however, the addition of a filter to the exhaust system increases the back pressure on the engine.

The DPF is designed to trap up to micrometre sized particles and increase the reactivity of these particles during DPF regeneration [Konstandopoulos et al., 2000]. Regeneration of the DPF can be accomplished via one of three primary methods; passive regeneration, active regeneration, and mixed passive-active regeneration [Chen et al., 2014].

Passive regeneration uses a catalyst coated DPF where PM matter is oxidized on the surface of the catalyst with NO_2 [Kotrba et al., 2013]. The advantages of the passive regeneration system are that it requires lower exhaust temperatures and is independent of the engine functioning, thereby not requiring a complicated control strategy. The disadvantages of the system are that it requires a catalyst coating and a specific exhaust NO_2/NO_x ratio, requiring an upstream catalyst such as a DOC to ensure a proper ratio [Kotrba et al., 2013].

Active regeneration requires high exhaust temperatures ($> 550°C$) so that PM oxidation occurs with oxygen available in the exhaust [Chen et al., 2014]. Because Diesel engine exhaust temperatures rarely achieve the required temperature, various strategies need to employed to increase the exhaust temperature. Strategies include locating the DOC directly upstream of the DPF and increasing the HC in the exhaust, either by direct injection or late post-injection in the cylinder, and having them oxidise in the DOC, which creates heat that is transferred to the DPF for regeneration [Chen

et al., 2014].

Mixed passive-active DPF regeneration is a blend of both the passive and active strategies, using a catalysed DPF and locating a DOC directly upstream of the DPF to oxidise HC and transfer heat to the DPF [Chen et al., 2014].

2.4.2 Selective Catalytic Reduction Catalyst

Reducing NO_x emissions is often accomplished by the use of urea injection and a SCR catalyst, normally containing either a Cu-zeolite catalyst, Fe-zeolite catalyst, or a combination of both [Nishiyama et al., 2015]. There are advantages to using either the Cu-zeolite or Fe-zeolite catalysts depending on the operating conditions, for example Cu-zeolite has better conversion efficiency at temperatures below 350°C with the converse being true for temperatures above 350°C [Cavataio et al., 2007]. For this reason a combined catalyst is often used to take advantage of the benefits of both catalysts, where it has been shown that a Fe : Cu ratio of 2 : 1 provides an optimal NO_x conversion [Nishiyama et al., 2015].

Using NH_3 (ammonia) as the reductant in the SCR allows NO_x to be converted to N_2 [Nishiyama et al., 2015]. Three different reactions occur in the SCR to convert NO_x and include the Fast-SCR reaction which occurs most readily at low temperatures, and the Standard-SCR and Slow-SCR reactions which occur at temperatures above 200°C and 275°C , respectively. Each of the three reactions are shown below [Nishiyama et al., 2015].

$$NO + NO_2 + NH_3 \rightarrow 2N_2 + 3H_2O \quad \text{(Fast-SCR)} \tag{2.13}$$

$$4NO + 4NH_3 + O_2 \rightarrow 4N_2 + 6H_2O \quad \text{(Standard-SCR)} \tag{2.14}$$

$$6NO_2 + 8NH_3 \rightarrow 7N_2 + 12H_2O \quad \text{(Slow-SCR)} \tag{2.15}$$

Due to the toxicity of ammonia, NH_3, and the difficulties associated with its handling, Diesel exhaust fluid (DEF) or urea is instead added to the exhaust stream which decomposes at high temperatures after being injected into the exhaust stream, and forms NH_3 by the reactions listed below [Nishiyama et al., 2015].

$$CO(NH_2)_2 \rightarrow NH_3 + HCNO \tag{2.16}$$

$$HCNO + H_2O \rightarrow NH_3 + CO_2 \tag{2.17}$$

2.4.3 Diesel Oxidation Catalyst

The primary function of the DOC is to oxidize CO, HC and portions of the NO emissions. As the oxidation of NO is equilibrium limited, the DOC oxidizes only portions of the NO to alter the NO/NO_2 ratio in the exhaust to meet the downstream requirements of the SCR or LNT [Watling et al., 2012; Russell and Epling, 2011]. Precious metals are the most commonly used catalysts in the DOC, typically platinum or palladium [Russell and Epling, 2011]. Each provide different advantages and disadvantages depending on the operating conditions of the engine and the exhaust composition and temperature.

The reactions occurring in the DOC are not fully understood as species interactions and the competition for available O_2 causes numerous intermediary reactions. Watling et al. [2012] have developed a model of the reaction kinetics occurring inside the DOC that illustrates the complicated species interactions that occur [Watling et al., 2012].

The light-off temperature of a catalyst is normally defined by the inlet gas temperature at which the catalyst can convert 50% of the intended reactant, known as the T50 point (although other points may be cited) [Martin et al., 1998]. The light-off

temperature for the DOC is approximately 250°C but depends on exhaust composition, the catalyst being used, and the construction of the DOC [Martin et al., 1998]. The importance of the light-off temperature is best exemplified by government legislated test cycles, where it has been shown that 50% to 80% of emissions are produced in the first 100 to 150 seconds prior to the catalyst reaching the light-off temperature [Jeong and Kim, 1998; Shen et al., 1999; Cho et al., 1998]. Variables affecting the light-off temperature of the DOC are the [Martin et al., 1998; Hayes et al., 2009]:

- composition of the catalyst
- age of the catalyst
- mass flow rate of exhaust gas
- exhaust gas temperature
- effective conductivity of the monolith
- flow maldistribution within the monolith
- bulk density of the monolith
- rate at which the inlet gas temperature increases

The complex interaction of all the variables involved in affecting the light-off temperature of the catalyst make optimisation of the DOC difficult. Furthermore, as the development of engines progresses, exhaust temperatures are becoming lower leading to increased time before light-off is achieved [Bartley, 2015].

2.5 Catalyst Construction

This section details the construction and function of the DOC, providing a detailed overview of the research that has focused on characterising the flow of exhaust through the DOC.

2.5.1 Monolith Geometry

DOC design requirements vary from vehicle to vehicle depending on the manufacturers requirements and optimization goals. The most common type of catalyst support structure used in the automotive industry is the honeycomb monolith. The monolith is composed of small channels in a honeycomb-like pattern running axially with the flow of the exhaust, as shown in Figure 2.4. The shape of the channels can vary depending on the requirements and benefits of each of the shapes. The cell geometry affects the mass and strength of the substrate, the heat and mass transfer characteristics, and flow resistance [Goralski and Chanko, 2001].

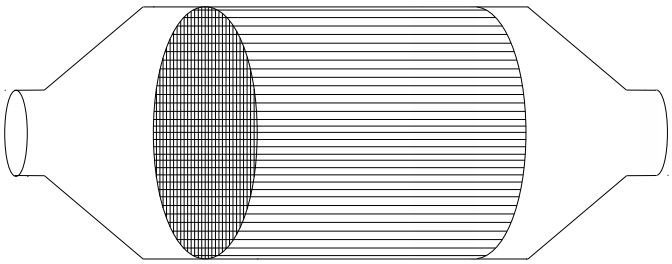

Figure 2.4: DOC showing the interior honeycomb like structure

Square, triangular, and hexagonal cells are the most common cell structures, however the final cell geometry is produced by the application of the washcoat to the monolith. Numerous studies have shown that the washcoat is not applied uniformly onto the substrate, rounding the corners of the cell and having a significant effect on the performance of the monolith [Hayes et al., 2009; Goralski and Chanko, 2001]. Goralski and Chanko performed a series of tests to determine the optimal cell geometry with washcoat applied and found that the hexagonal cells tend to have a higher conversion efficiency while each of the channel geometries showed a similar maximum effective loading [Goralski and Chanko, 2001]. Furthermore, they showed that hexagonal and square channels would show a similar pressure drop for exhaust flow rates typical of those seen in automobiles [Goralski and Chanko, 2001].

2.5.2 Flow Distribution

The flow through the DOC is complex and finding an optimal overall geometry difficult. The DOC can be broken into five sections and are shown in Figure 2.5; the inlet pipe (1), the inlet cone (2), the body (3), the outlet cone (4), and the outlet pipe (5).

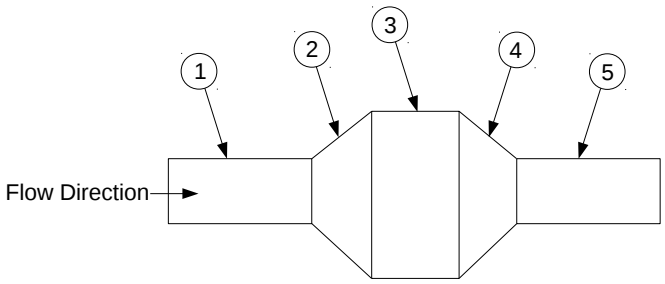

Figure 2.5: Schematic of the components that make up the DOC (axisymmetric)

The inlet and outlet pipes are the exhaust pipes that connect the DOC to the engine and the tailpipe, respectively. The inlet cone is an expansion cone (axisymmetric conical diffuser) that increases the diameter from that of the inlet pipe to that of the monolith. The body is composed of the honeycomb structure containing the catalyst, known as the monolith. The outlet cone is a compression cone (axisymmetric contraction) that decreases the diameter from the diameter of the body back to the diameter of the exhaust pipe.

2.5.3 Inlet/Outlet Flow

As the flow enters the inlet diffusers upstream of the monolith, the flow becomes even more turbulent and non-uniform as it expands with the increasing pipe diameter, resulting in a flow maldistribution over the radial profile of the DOC [Litto et al., 2016; Cho et al., 1998]. The flow through a diffuser is affected by three parameters: the half angle of the diffuser, the diffuser length to width ratio, and the turbulence of the flow into the diffuser, while the Reynolds number of the inlet flow was found to have

no effect for turbulent flow [Fox and Kline, 1962]. Fox and Kline [1962] demonstrated the relationlship between the diffuser half angle and the length to width ratios [Fox and Kline, 1962].

Fox and Kline [1962] were able to demonstrate that with increasing diffuser angle there exists a threshold where stall occurs. The greater the increase in half angle above the transition results in more fluid undergoing stall leading to larger degrees of turbulence. The stalled fluid along the walls creates a blockage that forces the flow to detour around the blockage and at sufficiently large amounts of stall a jet is created through the centre of the diffuser [Kline and Johnston, 1986]. The resulting flow maldistribution leads to the following negative effects [Cho et al., 1998; Jeong and Kim, 1998; Martin et al., 1998]:

- poor catalyst conversion efficiency
- premature ageing of the catalyst
- increased time to reach catalyst light-off
- increased pressure drop across the DOC

The flow maldistribution is often characterized by the flow uniformity index, γ, given by,

$$\gamma = 1 - \frac{1}{2\mathrm{n}} \sum_{\mathrm{i}=1}^{\mathrm{n}} \frac{\sqrt{(u_{\mathrm{i}} - \bar{u})^2}}{\bar{u}} \tag{2.18}$$

where u_{i} is the local flow velocity of the i^{th} area, $\bar{u}$ is the average velocity, and n is the total number of areas being considered [Cho et al., 1998]. Flow uniformity index values range from 0.7 to 0.98 for most catalytic converters, with values under 0.8 being considered poor [Cho et al., 1998].

Increasing the flow uniformity has been the subject of ongoing research and typically involves optimizing the inlet geometry. Replacing a portion of the monolith channels with a 3 mm thick ceramic insulating ring positioned at a radial distance from the centre of the monolith, as shown in Figure 2.6, in numerical simulations resulted in an increased flow uniformity [Litto et al., 2016]. The insulation ring showed a reduction in pressure drop across the DOC, despite decrease in flow area, as well as improving the light-off characteristics of the catalyst [Litto et al., 2016].

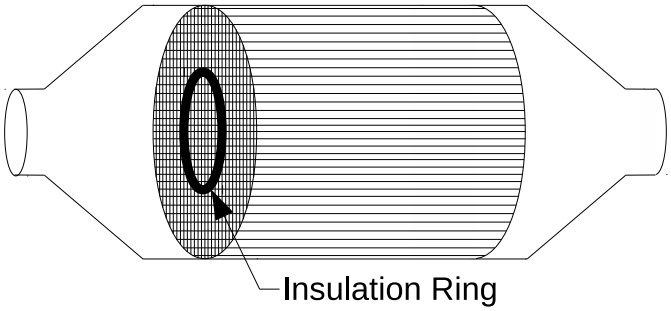

Figure 2.6: Positioning of the insulation ring inside the monolith of the DOC

Simulations showed that the decrease in pressure drop was due to a reduction in the turbulence in the inlet cone resulting in increased flow to the peripheral regions of the monolith [Litto et al., 2016]. Furthermore, as the flow exits the monolith, it is recompressed in the outlet cone causing increased fluid shear and turbulence. As the insulation ring helps to increase the flow uniformity, the shear during recompression in the outlet cone is reduced, decreasing the turbulence and ultimately the pressure drop [Litto et al., 2016].

2.5.4 Pressure Drop

The pressure drop across the DOC is the product of two major contributors; the resistance of exhaust gases passing through the small channels of the monolith, caused by fluid shear along the walls of the channel, and turbulence occurring in the inlet

and outlet cones, due to the sudden expansion and contraction of the exhaust gases. The pressure drop due to shear along the walls of the monolith is proportional to the fluid velocity, increasing as the velocity increases [Karvounis and Assanis, 1993].

It is common for numerical simulations to approximate the flow through the monolith as being fully-developed laminar flow over its entire length and to ignore turbulence. Turbulence in the monolith is primarily the result of three sources; turbulence originating upstream of the monolith in the diffuser, turbulence created by the channel walls at the entrance to the monolith, and turbulence caused by the surface roughness along the length of the channel walls [Holmgren and Andersson, 1998].

When laminar flow through the monolith channel is assumed, the flow through the monolith is Hagen-Poiseuille flow and the pressure drop in the channels of the monolith is the result of viscous forces [Ozhan et al., 2014] and the pressure drop, ΔP, can be approximated by Poiseuille's law,

$$\Delta P = \frac{8\mu L_c \dot{Q}_c}{\pi {D_c}^4} \tag{2.19}$$

where L_c and D_c is the monolith channel length and hydraulic diameter, respectively, μ is the fluid viscosity, and $\dot{Q}_c$ is the average volumetric flow rate in a single channel [Ozhan et al., 2014].

However, the pressure drop across the DOC is affected by turbulence in the inlet diffuser and outlet nozzle. Turbulence models commonly used to simulate flow across the DOC include the k-ϵ model [Karvounis and Assanis, 1993; Holmgren et al., 1997; Hayes et al., 2012] and the k-ω model [Litto et al., 2016].

To reduce the computational requirements of modeling the flow through each of the monolith channels, the monolith is modeled as a porous region consisting of strictly laminar flow [Karvounis and Assanis, 1993]. The assumption of laminar flow in the

monolith is not entirely valid as turbulence has been found to persist beyond the entrance of the monolith, however the effect on the pressure drop across the monolith has been shown to be very small [Cornejo et al., 2017]. The Forcheimer's modified formulation of Darcy's equation is included as a source term, $\vec{S}$, in the conservation of momentum equation and is given by,

$$\vec{S} = \left(\frac{\mu}{\alpha} + \frac{\rho C_2 |\vec{v}|}{2}\right)\vec{v} \tag{2.20}$$

where μ is the dynamic viscosity, $1/\alpha$ and C_2 are the viscous and inertial resistance factors. With the flow through the monolith being assumed laminar, the inertial resistance factor is set to zero as turbulence is not present. The viscous factor can be found either theoretically or empirically by either calculating the pressure drop using Equation 2.19 or by using experimental pressure drop data. Knowing the pressure drop, the viscous resistance factor can be related to the source term by simplifying the momentum equation to yield [ANSYS, Inc., 2006]

$$\Delta P = -S \cdot L = -\frac{\mu}{\alpha}\vec{v} \cdot L \tag{2.21}$$

where L is the length of the channel.

To simulate the unidirectional flow through the monolith, the viscous resistance terms in the radial direction are set to a minimum of three orders of magnitude larger than the axial direction [Karvounis and Assanis, 1993].

2.5.5 Monolith Temperature

The radial temperature profile of the monolith is affected by the exhaust gas temperature, the effective conductivity of the monolith, the exhaust composition, and the flow uniformity. Reactions occurring along the surface of the monolith channels which contain the catalyst are limited by two factors; the rate of reaction and the rate of mass transfer [Karvounis and Assanis, 1993]. While the monolith is initially at ambient temperature, the conversion rate of the catalyst is limited by the rate of reaction. Once the exhaust gases have sufficiently heated the monolith, the rate limiting factor in the conversion rate switches from rate of reaction to rate of mass transfer. Due to the difficulty in determining the exact temperature in which this switch occurs, the light-off temperature is often used as an approximation of this switch.

A number of factors can affect the ability for the catalyst to reach light-off, including the exhaust temperature and the flow uniformity. The exhaust gas temperature has a large affect on the time required for the catalyst to reach light-off and as automotive exhaust temperatures become lower, there is evidence that vehicles are unable to meet emissions standards due to their inabiliy to reach light-off in a reasonable time [Bartley, 2015]. The exhaust composition can also play a role in the time required to reach light-off, as certain molecules inhibit the ability of reactants to react on the catalyst, leading to a decrease in conversion efficiency and an increase in the light-off temperature [Bartley, 2015].

The radial temperature profile of the monolith is affected by the effective conductivity of the monolith and the flow uniformity. The effective conductivity of the monolith can be approximated using the electrical resistances analogy [Hayes et al., 2009]. When the monolith construction is changed, for example by adding an insulation ring, as discussed in Section 2.5.3, the effective conductivity causes a change in the radial temperature profile [Hayes et al., 2009]. The insulation ring results in a

decrease in time required to reach light-off as the insulation ring maintains the heat in the central region of the monolith and at low load (as is typical during vehicle warm-up) the majority of the exhaust gases are directed through the central region of the monolith [Litto et al., 2016] due to the effect of a jet being created in the inlet diffuser (see Section 2.5.2. As the central region of the monolith heats up faster and the majority of the flow passes through the central region, emissions can be reduced.

Chapter 3

Experimental Setup

This Chapter details the experimental setup used and includes a detailed explanation of the Diesel engine along with modifications, the engine dynamometer, the exhaust setup, the geometry and assembly of the DOC, and the sensors used for data collection.

3.1 Experimental Setup

The primary objective of the experiment was to characterize the flow of exhaust gas as it passed through the DOC and to determine the heating characteristics of the DOC. The DOC is connected to a stock Cummins 4-cylinder Diesel engine (see Section 3.2) and a Tornado centrifugal fan with 6.5 HP electric motor, giving the option of directing hot exhaust gas from the engine or cold air from the blower through the DOC. By opening or closing the correct configuration of valves, as shown in Figures 3.1 and 3.2, the gas passing through the DOC can be easily switched between hot from the engine or cold from the blower.

The hot exhaust gas can be bypassed around the DOC allowing the engine to reach steady state operation with a constant exhaust temperature prior to directing the gas through the DOC. After passing through the DOC, the exhaust gasses pass through a muffler and then are exhausted into an open exhaust conduit drawing exhaust in at slightly lower pressure than the ambient room pressure, as shown in Figure 3.2.

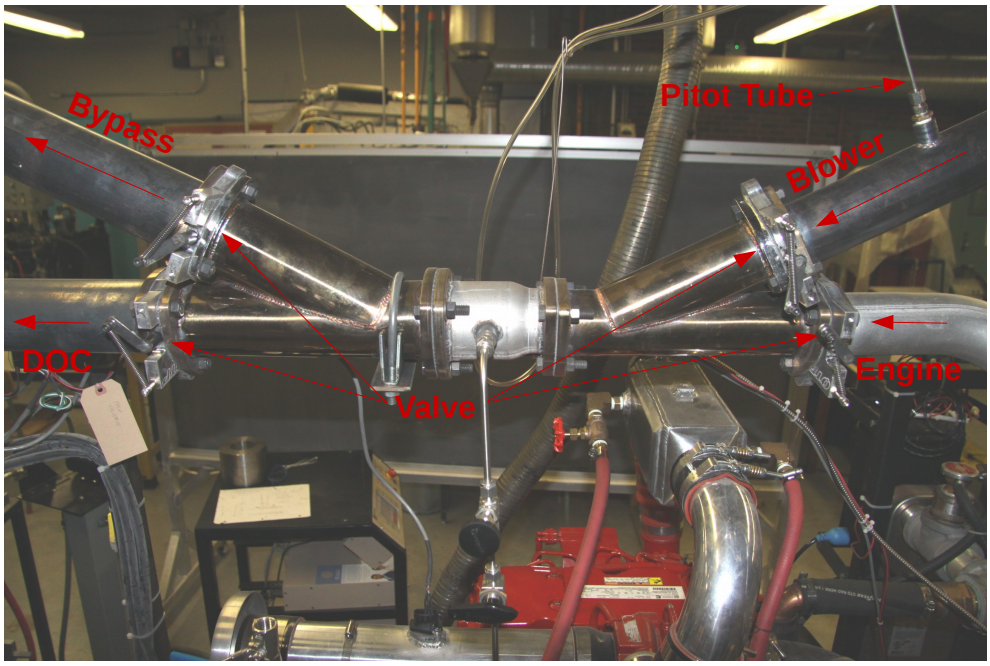

Figure 3.1: Exhaust bypass setup

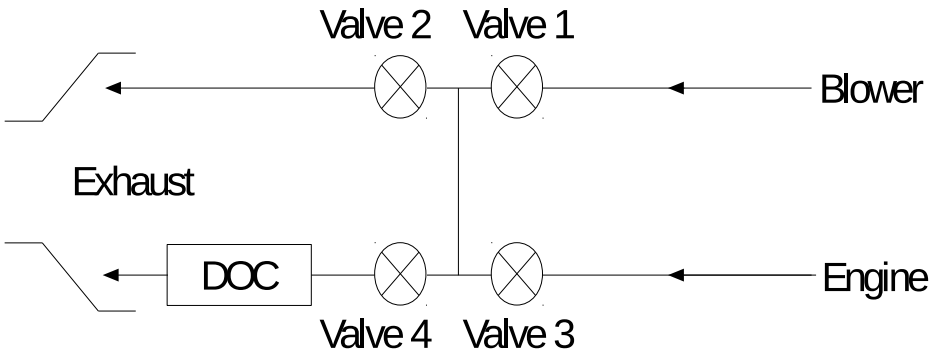

Figure 3.2: Schematic of the experimental setup

3.2 Engine Specifications

A stock Cummins 4-cylinder QSB4.5 (Tier 3) Diesel engine is used for the tests. The engine specifications are outlined in Table 3.1 and the engine is shown in Figure 3.3. Changes to the stock engine included a custom air intake (see Section 3.2.1), the addition of a liquid-cooled intercooler (see Section 3.2.2), and a flat-plate heat exchanger for engine cooling (see Section 3.2.3).

Table 3.1: Engine Specifications

Orientation	In-Line
Cylinders	4-Cylinder
Displacement	4.5 L
Horsepower	109-170 hp (81-127 kW)
Torque	360-460 ft-lb (488-624 kW)
Aspiration	Turbocharged

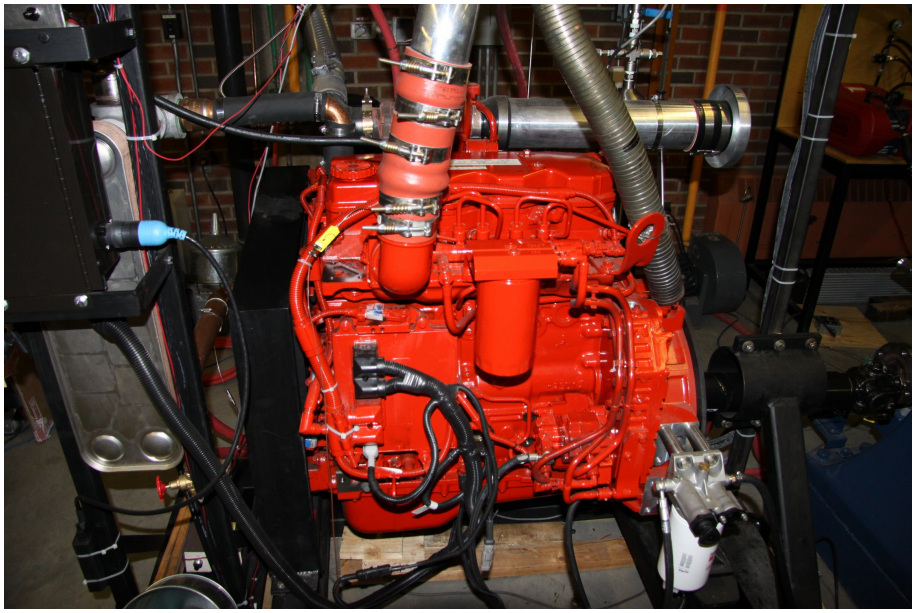

Figure 3.3: Cummins 4-cylinder QSB4.5 (Tier 3) Diesel Engine

3.2.1 Air Intake

The air intake is constructed from a 0.61 m (2') long pipe, 0.10 m (4") in diameter, connected upstream of the engine turbocharger. The inlet to the pipe had the edges rounded to minimize turbulence at the intake of the pipe, as shown in Figure 3.4. The inlet tube is outfitted with a stock Ford automotive digital hot film mass flow (HFM) sensor (AFLS-166), also known as a Mass Air Flow (MAF) sensor, located 0.30 m (12") (approximately 3 diameters) from the entrance of the inlet tube.

The HFM sensor located in the air intake is a thermal flow meter containing a heated surface running parallel with the air flow direction. The heated surface expe-

Figure 3.4: Custom air intake with HFM sensor

riences a temperature gradient in the direction of the air flow, proportional to the air flow rate [Stone, 2012]. Temperature resistors are located just upstream and downstream of the heating strip and as air passes over the sensor it creates a temperature differential between the two strips, a larger temperature differential is the result of a smaller flow rate as the air passing is exposed to the heating strip for a longer time allowing a greater overall heat transfer from the strip to the air. The sensor was externally calibrated giving the relationship between the volumetric flow rate of air, $\dot{Q}$, (in cfm) at 20°C as,

$$\dot{Q} = 1.6169 f^{2.7551} \tag{3.1}$$

where f is the sensor output frequency (in Hz).

3.2.2 Air Intake Temperature Control

The intake air was maintained at a constant temperature using a liquid cooled intercooler, as shown in Figure 3.5a, located downstream of the engine turbocharger. The liquid cooled intercooler was equipped with an OMEGA CNi8 series PID controller, shown in Figure 3.5b, allowing the intake air temperature to be maintained at 35 $\pm$ 3°C by controlling the mass flow of water into the intercooler, using an OMEGA electronically controlled proportioning valve.

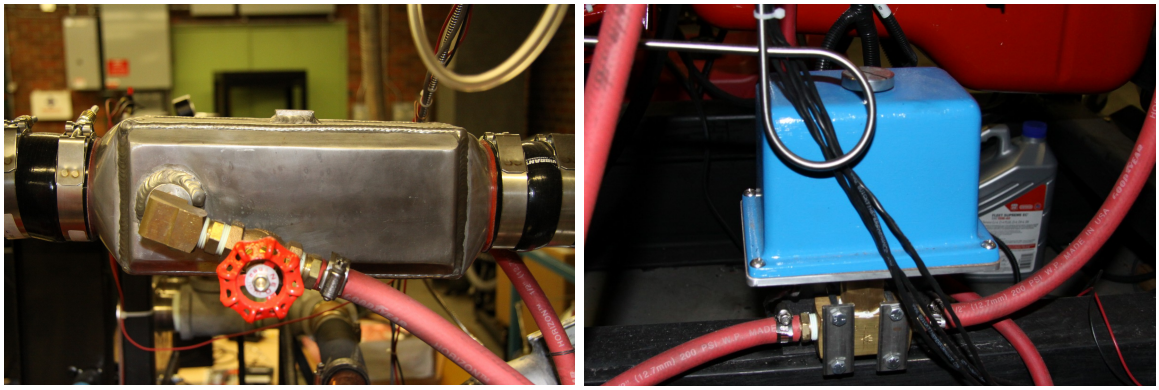

(a) Intake air intercooler (b) OMEGA proportioning valve

Figure 3.5: Air intake temperature control system

3.2.3 Engine Temperature Control

The engine temperature was controlled by the stock engine controller. Engine coolant was circulated through an Alfa Laval CB100-24L flat plate heat exchanger and maintained the engine coolant temperature between 80°C and 85°C, shown in Figure 3.6. A constant flow of cold water at ~10°C is supplied from an external source and is used as the counterflow fluid to the engine coolant.

Figure 3.6: CB100-24L flat plate heat exchanger

3.3 Dynamometer

The engine is connected to a Dyne Systems 1014 W passive eddy current dynamometer. Engine speed is controlled by the stock engine controller and the dynamometer controller maintains the user specified back torque on the engine. The engine is capable of producing a maximum torque of 625 Nm (460 ft-lbs) at 1900 rpm while the dynamometer is capable of producing a maximum back torque of 710 Nm (525 ft-lbs) at 2500 rpm. Figure 3.7 shows the torque curve for the dynamometer [Dyne Systems, 2014].

3.4 Exhaust Setup

The exhaust setup consisted of a 0.06 m (2.5”) diameter flex pipe leading from the exhaust side of the turbocharger to a 0.08 m (3”) diameter straight pipe where it passes through a series of valves allowing the gases to bypass the DOC, if required (see Section 3.1). The exhaust would then pass through a 1 m (3.25’) length of straight pipe intended to induce fully developed flow prior to entering the DOC.

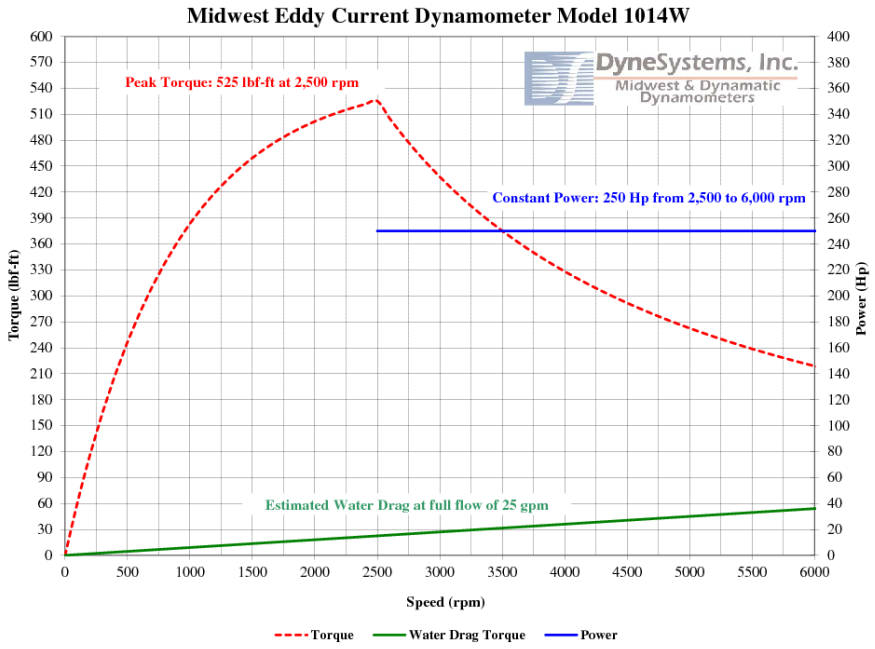

Figure 3.7: Dyne Systems 1014 W Torque/Power Curves

Figure 3.8 illustrates the components that form the DOC and includes the inlet diffuser, an internally insulated 0.20 m (8") diameter length of pipe containing the DOC monolith (shaded region), and an outlet nozzle (the construction of the DOC is further explained in Section 3.5.

The exhaust flow from the outlet nozzle is exhausted via a 1 m (3.25') length of 0.05 m (2") straight pipe and leads to a section of 0.06 m (2.5") flex pipe. The flex pipe connected to a muffler before exhausting to a central exhaust system. It is known that both the diffuser angle, θ_{Diffuser}, and nozzle angle, θ_{Nozzle}, affect the flow of exhaust gases into the monolith and result in a change in the pressure drop across the DOC. An increase in the diffuser angle results in more exhaust passing through the central core of the DOC [Hayes et al., 2012; Kline and Johnston, 1986]. The impact of the diffuser and nozzle angles on pressure drop is not explored in this study and the angles are kept constant.

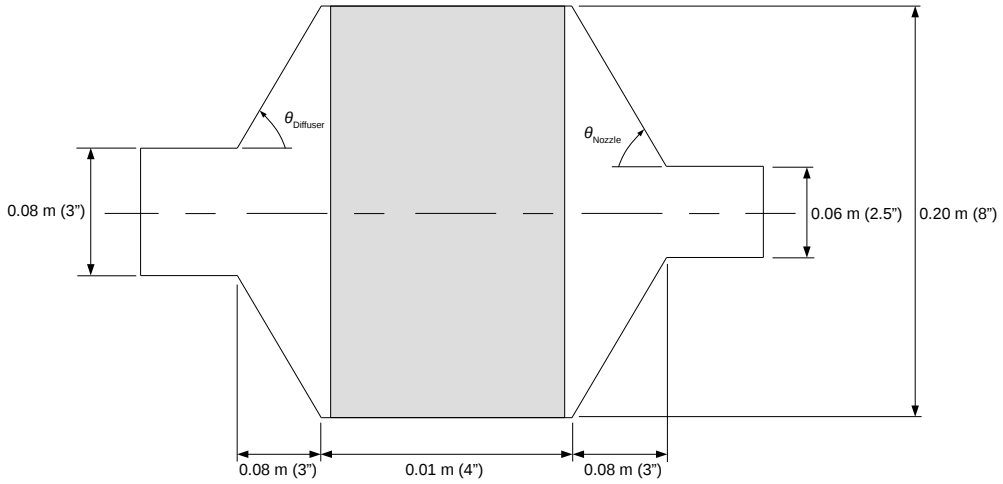

Figure 3.8: DOC dimensions with monolith represented by the shaded area

3.5 Diesel Oxidation Catalyst

The DOC is composed of an 0.20 m (8") diameter stainless steel pipe with the monolith located inside. The monolith is composed of a ceramic substrate constructed of square cells in a honeycomb like manner (channels running longitudinally with the flow) and a cell density of 0.62 cells/mm^2 (400 cpsi). Figure 3.9 illustrates the DOC assembly with a layer of Pyrotek expanding insulation between the monolith and pipe, 8 mm in thickness, which both reduces the energy lost from the DOC and ensures the monolith remains centered inside the DOC.

Four monoliths are used for testing with similar construction with the exception that three of the monoliths contain an insulation ring, each of a different diameter. The insulation ring is a ceramic material injected into the square channels of the monolith creating a ring approximately 5 mm in thickness. The diameters of the insulation rings are specified in Table 3.2 and Figure 3.9 illustrates the location of the insulation ring.

A typical automotive DOC will contain a catalyst applied to the monolith by

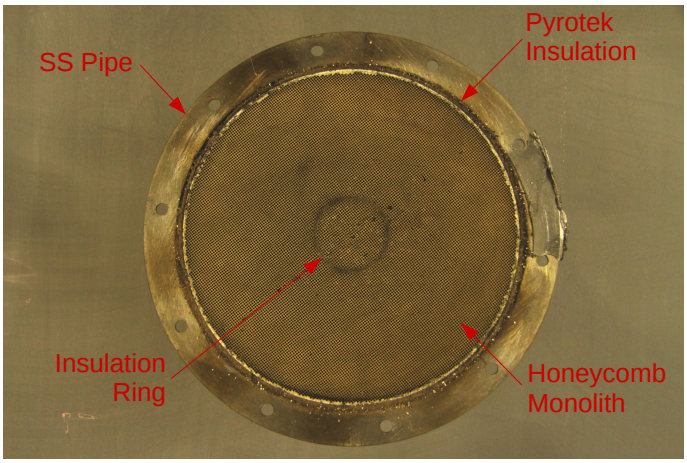

Figure 3.9: Structure of the DOC (shown in cross section)

Table 3.2: Inside and outside diameters of monolith insulation rings

DOC	Description	ID (mm)	OD (mm)
1	No Insulation Ring	N/A	N/A
2	Small Insulation Ring	41 ± 2	46 ± 2
3	Medium Insulation Ring	70 ± 2	75 ± 2
4	Large Insulation Ring	99 ± 2	104 ± 2

submersing the monolith in a liquid containing the catalyst, known as the washcoat, which is then cured onto the monolith. None of the four monolith have had a washcoat applied as the flow characteristics through the monolith are the parameters of interest and not the reaction kinetics, therefore no active catalyst is present. The DOC construction (without diffuser/nozzle) is shown in Figure 3.9.

3.6 Sensors

Exhaust composition is determined using NOxCANt ECM sensors, shown in Figure 3.10a, and includes a NO_x sensor, NH_3 sensor, and O_2 sensor. The sensors are located 0.30 m, 0.35 m, and 0.40 m upstream of the entrance to the diffuser, respectively. The ECM sensors are connected via an ECM CAN line, shown in Figure 3.10b, to the computer for data collection using Kvaser Leaf Light HS.

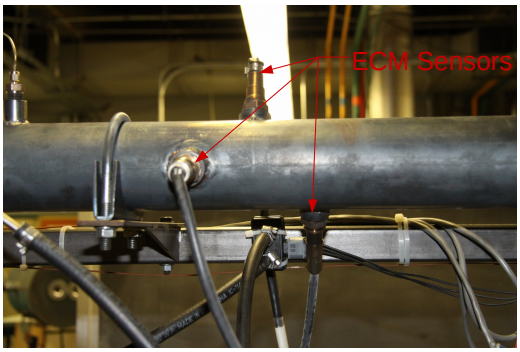

(a) ECM Sensors

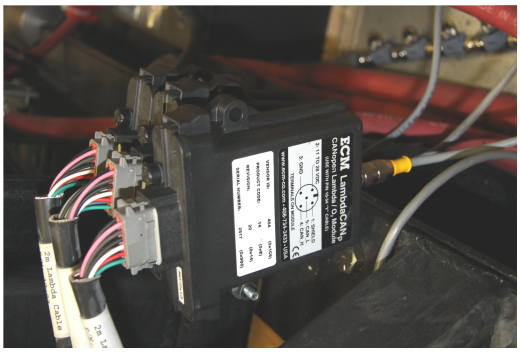

(b) ECM DAQ Boxes

Figure 3.10: ECM sensors for NO_x, NH_3, and $\%O_2$

Engine data is collected using a Cummins INLINE 6 Data Link Adapter, shown in Figure 3.11, allowing the computer to access the stock engine control module and download the engine parameters in real time to the computer. Data is collected using INLINE 6, commercial software distributed by Cummins.

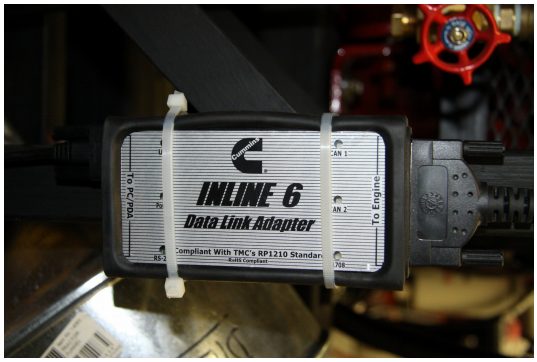

Figure 3.11: INLINE 6 Data Link Adapter from Cummins

The thermocouple used are OMEGA 20G K-Type thermocouples and are connected to a NI9213 analog input module and read by the computer using LabVIEW. Eleven thermocouples are located at known radial locations across the downstream side of the monolith, as shown in Figure 3.12. The radial distance of each thermocouple is the same for all of the transient tests (outlined in Table 3.3) allowing comparison of the heating characteristics for each of the 4 DOC configurations tested (see Section 3.5) . Locations of the thermocouples are placed directly on either side

of the insulation as well as midway between the insulation rings (if they were to all be superimposed onto the same monolith). There are also three thermocouples located in the exhaust piping; one thermocouple is located immediately downstream of the exhaust manifold, one 0.15 m upstream of the entrance to the diffuser, and one 0.15 m downstream of the exit to the diffuser, as shown in Figure 3.13.

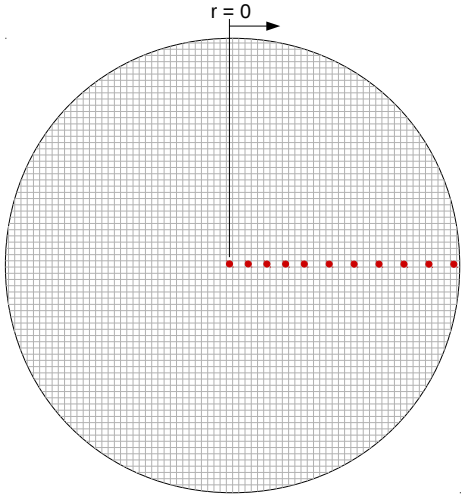

Figure 3.12: Locations of thermocouples in the monolith (shown in cross section)

Table 3.3: Radial location of thermocouples in monolith

Thermocouple	Radial Location (mm)
1	0
2	18
3	22
4	28
5	34
6	40
7	43
8	47
9	53
10	71
11	90

The differential pressure sensor is a stock automotive pressure sensor with a linear relationship between the voltage output and a change in pressure. The pressure taps are located 0.15 m upstream and downstream of the DOC, as shown in Figure 3.13. The pressure sensor is calibrated to give the following relationship between the output voltage, V_{out}, (in Volts) and the differential pressure, ΔP, (in kPa),

$$\Delta P = 2.7185 V_{\text{out}} - 6.9283 \tag{3.2}$$

The output voltage from the pressure sensor is collected via a NI9205 analog input module and collected by a computer using the commercial software LabVIEW. The sampling rate for all of the variables was set to 1 Hz as the time constant of the DOC temperature is much longer than 1 Hz allowing the dynamic response of the DOC to be easily captured.

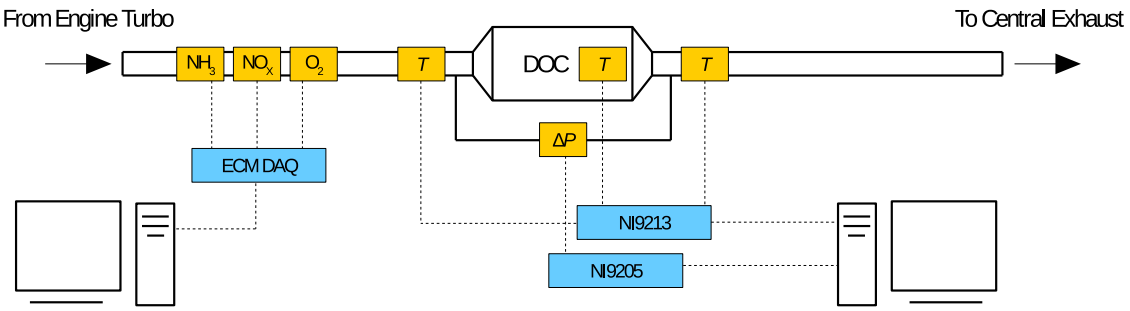

Figure 3.13: Exhaust setup showing the sensors and data acquisition equipment

3.7 Operating Points

Engine operating points were selected to span the engines operating range by varying both the speed and load. The operating points are outlined in Table 3.4. Engine speed

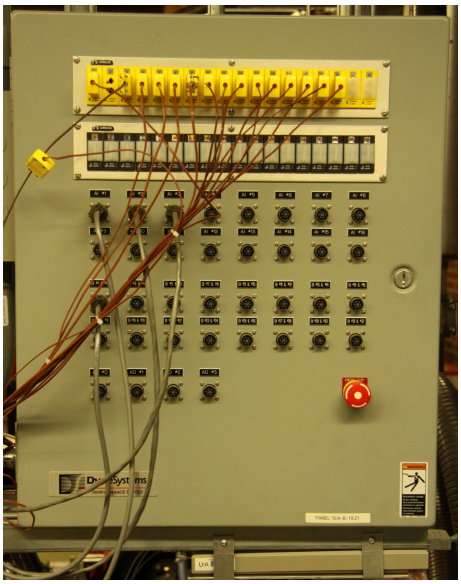

Figure 3.14: DAQ Box used for the thermocouples and pressure sensor

was controlled using the stock engine controller while a back torque was applied via the dynamometer in torque mode. Uncertainty in the engine speed is a product of the engine controllers response to internal changes in conditions and the inability to select a precise engine speed as speed input into the stock engine controller is only allowed in 10 rpm increments, giving the ability to only select an engine speed to within $\pm$ 10 rpm of the desired speed. Uncertainty in the dynamometer torque is assumed to be $\pm$ 1.36 Nm (1 ft-lbs) as the dynamometer is highly responsive to disturbances in loading and testing is being done at with the engine operating at steady state.

3.8 Post Processing and Output Calculations

In this section, details of how the measured data are post processed are given. Some of the parameters can be calculated directly from the data while others are estimated using iterative methods.

Table 3.4: Experimental operating points (± is based on maximum deviation)

Point	Engine Speed (rpm)	Dyno Torque (ft-lbs)	Exhaust Flow (g/s)
1	1000 ± 18	50 ± 1	32.1 ± 2.5
2	1000 ± 50	100 ± 1	32.8 ± 3.9
3	1500 ± 13	50 ± 1	53.9 ± 9.3
4	1500 ± 12	100 ± 1	59.0 ± 9.2
5	1500 ± 13	200 ± 1	79.5 ± 20.6
6	2000 ± 4	450 ± 1	114.5 ± 18.0
7	2000 ± 24	50 ± 1	89.5 ± 4.8
8	2000 ± 5	100 ± 1	106.3 ± 18.9
9	2000 ± 24	200 ± 1	157.3 ± 45.5
10	1950 ± 235	450 ± 1	176.0 ± 25.5
11	2500 ± 18	50 ± 1	136.1 ± 13.9
12	2500 ± 14	100 ± 1	179.8 ± 34.0
13	2500 ± 12	200 ± 1	209.7 ± 9.2
14	2500 ± 32	275 ± 1	207.0 ± 8.9

3.8.1 Intake Air Mass Flow Rate

The mass flow of air into the engine is estimated from the measured volumetric flow of air into the engine (as measured by the HFM sensor). The mass flow rate of air can be used to determine an estimate of the engine fuel consumption and exhaust mass flow rate. Measuring the exhaust flow rate directly is difficult as the exhaust gas temperatures are high and the presence of contaminants easily fouls sensors.

To determine the mass flow rate of air into the engine, the density of the air at the HFM sensor, ρ_2, is needed and can be determined by iterating between the ideal gas law and the Bernoulli equation, rearranged to give,

$$\rho_2 = \rho_1 \frac{P_2}{P_1} \frac{T_1}{T_2} \tag{3.3}$$

$$\rho_2 = \frac{2(P_1 - P_2)}{{V_2}^2} \tag{3.4}$$

where P_1, T_1, and ρ_1 are the atmospheric air pressure, temperature, and density,respectively, and P_2, T_2, and ρ_2 are the air pressure, temperature, and density, respectively, at the HFM sensor inside the air intake. The velocity of air at the HFM sensor, V_2, is calculated using the volumetric flow rate and cross-sectional area. The form of the Bernoulli equation assumes incompressible flow and as the velocity of the air at the HFM sensor is less than 1/10th the speed of sound, the error introduced is known to be small [Yunus and Cimbala, 2006]. The atmospheric pressure, P_1, and temperature, T_1 are measured at the beginning of each test and the temperature in the intake was assumed to be the same as the atmospheric temperature, as expansion effects are assumed to be minimal. The velocity of air into the intake, V_1, is approximated to be zero (large reservoir assumption).

3.8.2 Exhaust Mass Flow Rate

The mass flow rate of exhaust was estimated using the sum of the intake air mass flow rate and the mass flow rate of fuel into the engine. The flow rate of exhaust is difficult to measure directly as the conditions in the exhaust are not conducive to mass flow sensors since the exhaust contains large amounts of particulate, which rapidly foul the sensor, and the high temperature which affect the material properties of the sensor. The mass flow rate of fuel into the engine can be be estimated by using the intake air mass flow rate and finding the difference in oxygen concentration between the exhaust and atmosphere.

The exhaust oxygen concentration is measured by the ECM sensors, located in the exhaust pipe just upstream of the DOC, while the atmospheric oxygen concentration is assumed to be 20%. Furthermore, combustion is assumed to be stoichiometric and the fuel is assumed to be composed solely $C_{12}H_{23}$. The mass flow rate of the exhaust is then estimated by,

$$\dot{m}_{\text{exhaust}} = \dot{m}_{\text{air,in}}\left[1 + \left(Y_{\text{O}_2,\text{in}} - Y_{\text{O}_2,\text{exhaust}}\right)\left(17.75\frac{\text{mol}_{\text{O}_2}}{\text{mol}_{\text{C}_{12}\text{H}_{23}}}\right)\frac{\text{M}_{\text{O}_2}}{\text{M}_{\text{C}_{12}\text{H}_{23}}}\right] \tag{3.5}$$

where $Y_{\text{O}_2,\text{in}}$ is the molar atmospheric oxygen concentration, $Y_{\text{O}_2,\text{exhaust}}$ is the molar exhaust oxygen concentration, 17.75 $\text{mol}_{\text{O}_2}/\text{mol}_{\text{C}_{12}\text{H}_{23}}$ is the molar ratio of oxygen to fuel in stoichiometric combustion of $\text{C}_{12}\text{H}_{23}$.

Many assumptions were made in determining the mass flow rate of exhaust and to validate the results of the calculation, an engine test was performed measuring the intake air flow rate via the HFM sensor while the mass flow rate of fuel was measured by placing the fuel tank on a scale and measuring its weight over time. Figure 3.15 illustrates the mass flow rates of fuel and air, showing that the mass flow rate of air into the engine is one to two orders of magnitude larger, depending on the operating point, suggesting that error introduced into the calculation of the mass flow rate of fuel is small compared to the overall mass flow rate of exhaust. Furthermore, as the fuel consumption is nearly identical between each of the four DOC configurations for a given operating point, the error introduced will be similar allowing comparison between the DOC configurations.

3.9 Engine Facility Setup

This section details additions to the engine facility that will be used for future experimental testing.

3.9.1 Ammonia Injection

An ammonia injection system was added to the Diesel exhaust setup for future SCR catalyst testing and ammonia sensor testing. The setup consist of a reservoir containing 30% aqueous ammonia (although any concentration could be used). Compressed

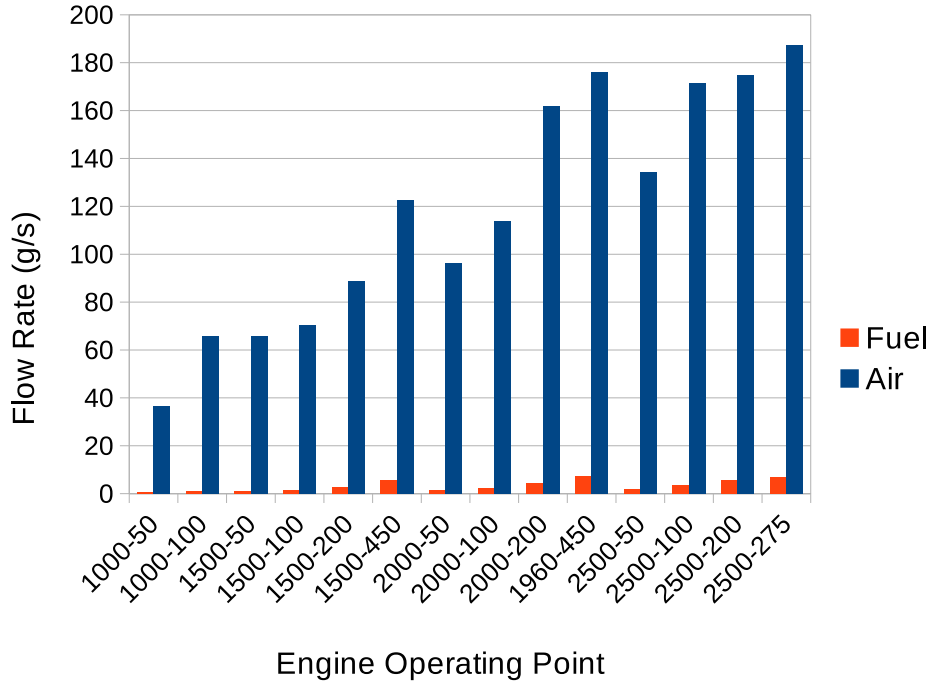

Figure 3.15: Comparison of engine fuel and air consumption

air flows into the bottom of the reservoir and flows upwards through the aqueous ammonia. Desorption of ammonia from the water to the air stream results in an increase in gaseous ammonia. The flow of air and ammonia is then exhausted from the reservoir to the Diesel exhaust stream. Figure 3.16 illustrates the ammonia injection system setup.

To confirm the sufficiency of the ammonia injection system, a series of tests were performed to determine the ability of the ammonia injection system to reach sufficiently high levels of ammonia in the exhaust stream. Figure 3.17 shows the ammonia concentration in the exhaust stream as measured by the ECM NH_3 sensor (see Section 3.6). The test was performed with a flow rate of 207 $\pm$ 9 g/s, corresponding to an engine operating point of 2500 rpm and 373 Nm (275 ft-lbs). The initial volume of 30% aqueous ammonia in the reservoir was 278 mL and compressed air was used in place of nitrogen.

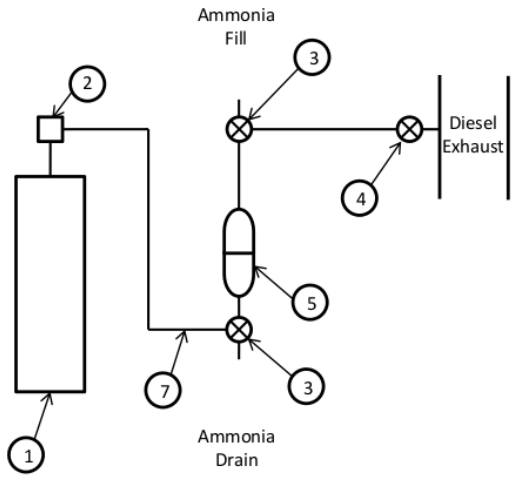

ITEM	DESCRIPTION	QTY
1	Pressurized Nitrogen Cylinder	1
2	Regulator	1
3	SS 3-Way Ball Valve	2
4	SS 2-Way Ball Valve	3
5	Pressure Sample Cylinder (Edm Valve and Fitting)	1
6	SS 1/4in Tubing	-

Figure 3.16: Schematic of the ammonia injection system

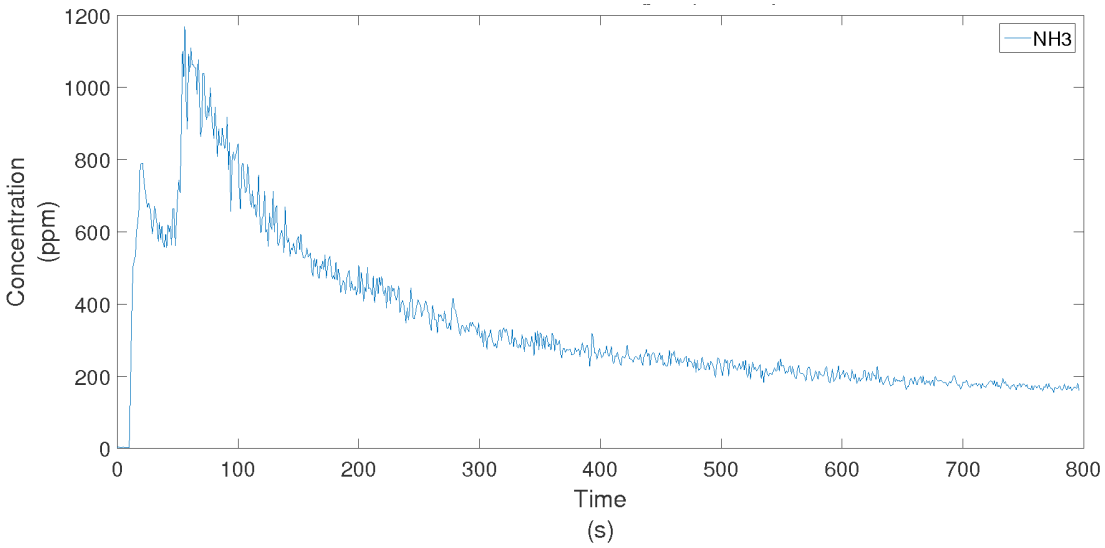

Figure 3.17: Ammonia concentration in the exhaust stream

Figure 3.17 illustrates that the ammonia injection system is easily capable of delivering the required 300 ppm of ammonia to the exhaust stream. With the addition of a controller, using the ammonia concentration in the exhaust as the reference and the nitrogen regulator regulating the flow into the reservoir, as the actuator.

Chapter 4

Simulation Setup

This Chapter details the setup used to simulate the flow through the Diesel Oxidation Catalyst using ANSYS software Fluent 16.2

4.1 Simulation Setup

ANSYS Fluent 16.2 was used to simulate the flow of exhaust gas through the DOC and the heat transfer from the system using a two-dimensional axisymmetic model. The DOC was modeled and meshed using ANSYS ICEM CFD. The monolith is composed of square channels approximately 0.81 mm^2 seperated by cordierite walls approximately 1 mm in thickness. To simplify the model, the exhaust flow through the DOC is assumed to be:

- a variable density ideal gas
- incompressible for the purpose of flow modeling
- steady state such that flow pulsations are ignored
- premixed such that diffusion is ignored

4.2 Geometry and Meshing

The geometry of the model is shown in Figures 4.1 and 4.2 with dimensions listed in Table 4.1. All four of the DOC insulation rings were combined into a single model, leaving only the boundary conditions to be altered to give each of the different models. This ensured an identical mesh for each of the four simulations.

Table 4.1: Dimensions of DOC as illustrated in Figures 4.1 and 4.2

Dimension	Length (mm)
A	225
B	75
C	105
D	75
E	220
F	35
G	20
H	95
I	20
J	3
K	12
L	3
M	12
N	3
O	37
P	5

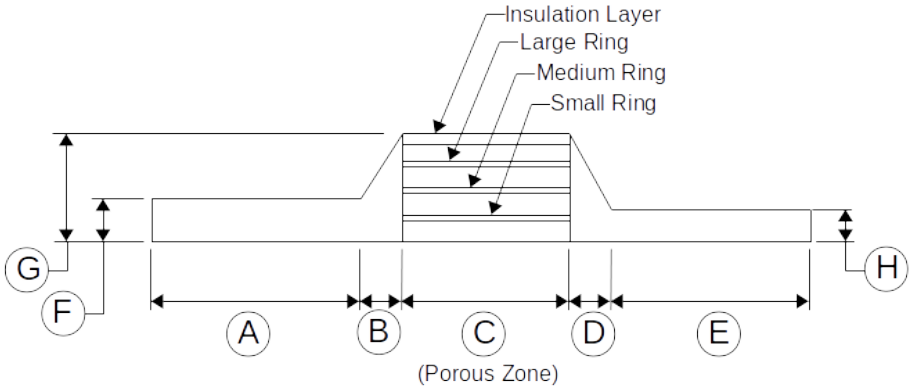

Figure 4.1: Axisymmetric model used for numerical model of DOC

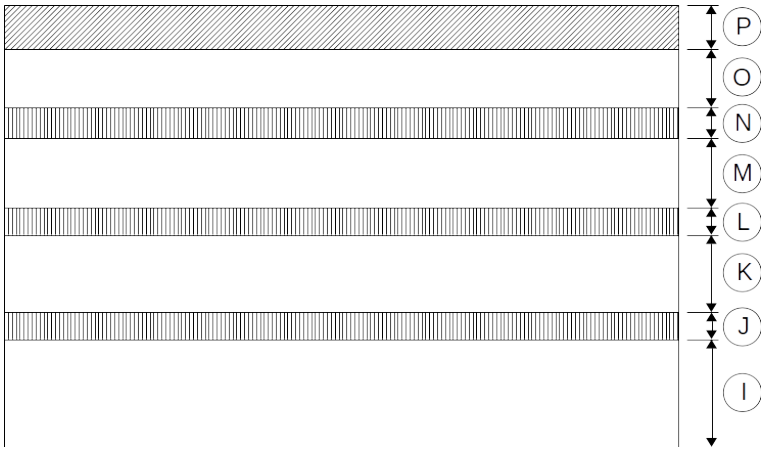

Figure 4.2: Detailed geometry of porous zone (see Figure 4.1)

The geometry is broken into a series of blocks for meshing. Along the horizontal axis the mesh is broken into five blocks, corresponding to each of the regions labelled A through E in Figure 4.1. Along the vertical axis the mesh is broken into eight blocks corresponding to each of the regions labelled I through P in Figure 4.2. The mesh is sized to obtain a maximum mesh sizing of 0.5 mm within the monolith of the DOC (region C) while the mesh inside the inlet and outlet pipe (regions A and E) is sized proportionally to the monolith and ensures that the elements remain the same size regardless of the vertical location, resulting in elements that are evenly spaced along both the vertical and horizontal axes. The mesh sizes are outlined in Table 4.2.

4.2.1 Material Properties

The material properties for each of the components of the DOC are listed in Table 4.3. As the material properties are not known accurately, they were adjusted slightly to improve the fit between the numerical analysis and experimental results. The shell of the DOC is constructed from 1/32" stainless steel (SS310), the insulation between the shell and monolith is 3/16" Pyrotek® IR-3, the monolith is cordierite, and the insulation ring is created by injecting ceramic into the channels of the monolith.

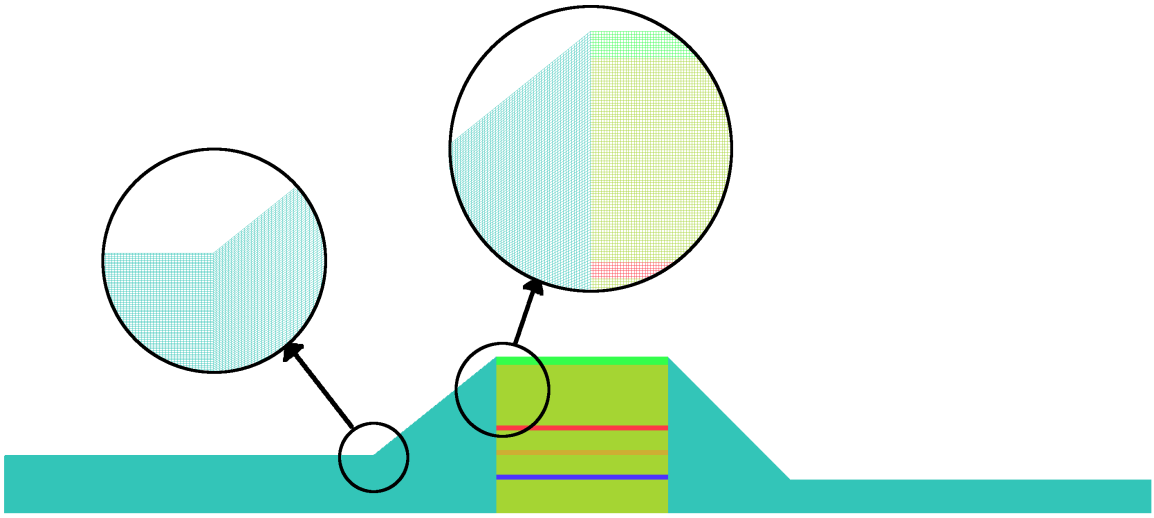

Figure 4.3: DOC meshing using ANSYS ICEM to create structured mesh

Table 4.2: Mesh sizing by component

Dimension	Nodes	Max Mesh Size (mm)	Min Mesh Size
A	751	0.30	0.30
B	164	0.49	0.30
C	211	0.51	0.51
D	164	0.48	0.29
E	734	0.30	0.30
I	41	0.50	0.19
J	7	0.50	0.19
K	25	0.50	0.18
L	7	0.50	0.18
M	25	0.50	0.18
N	7	0.50	0.18
O	75	0.50	0.19
P	11	0.50	0.18

4.3 Heat Transfer

The heat transfer from the DOC to the surroundings was modeled using a natural convection model. The wall was constructed of stainless steel (SS310), an overall heat transfer coefficient of 15 W/(m-K) was used along with a free stream temperature of 305 K. Radiation from the DOC was ignored as it was assumed to be small.

Table 4.3: DOC material properties

Material	Density (kg/m3)	Specific Heat (J/(kg-K))	Thermal Conductivity (W/(m-K))	Viscosity (kg/(m-s))
Exhaust	0.650	1050	0.06	3.00E-05
SS310	7750	520	18	N/A
Pyrotek	115	900	0.15	N/A
Ceramic	480	1200	0.2	N/A
Cordierite	2300	850	1.8	N/A

4.4 Turbulence

A SST k-omega turbulence model with production limiter was used to model the flow through the system. The recommended Fluent model constants were used in the simulation and are listed in Table 4.4.

Table 4.4: SST k-omega turbulent flow parameters

Constant	Value
${\alpha^*}_\infty$	1.0
α_∞	0.52
${\beta^*}_\infty$	0.09
a_1	0.31
$\beta_{i,1}$	0.075
$\beta_{i,2}$	0.0828
$\sigma_{k,1}$	1.176
$\sigma_{k,2}$	1.0
$\sigma_{\omega,1}$	2.0
$\sigma_{\omega,2}$	1.168
Pr_t	0.85
Pr_θ	0.85
C_{lim}	10.0

The inlet turbulence levels were specified using an inlet and outlet turbulent intensity of 5% with backflow hydraulic diameters of 70 mm and 40 mm, based on the actual diameters of the inlet and outlet, respectively.

4.5 Porous Zone

To model the flow through the monolith, a porous model is used in Fluent by including a source term in the momentum equation [Mladenov et al., 2010; ANSYS, Inc., 2006]. The equation used by Fluent is the Forcheimer modified formulation of Darcy's equation, given by Equation 2.20. Because the flow through the monolith is assumed to be laminar, the inertial resistance factor is set to zero. The method used to estimate the viscous resistance factor is explained in Section 4.6. To impose unidirectional flow in the monolith, the viscous resistance factor in the radial direction is set to a minimum of three orders of magnitude larger than the axial direction [Karvounis and Assanis, 1993].

The heat transfer in the monolith is calculated using a homogeneous energy model. The homogeneous model uses the effective thermal conductivity, k_{eff}, which is calculated automatically by the software for a homogeneous porous region by,

$$k_{\text{eff}} = \epsilon k_{\text{f}} + (1 - \epsilon) k_{\text{s}} \tag{4.1}$$

where ϵ is the porosity and can be found to be 0.75 for a cordierite monolith [Hayes et al., 2009], k_{f} is the thermal conductivity of the fluid and k_{s} is the thermal conductivity of the solid. As the monolith is not a homogeneous porous region, the effective thermal conductivity can be calculated using [Hayes et al., 2009],

$$k_{\text{eff}} = \left[1 - \sqrt{\epsilon} + \frac{\sqrt{\epsilon}}{1 - \sqrt{\epsilon} + (k_{\text{s}}/k_{\text{f}})\sqrt{\epsilon}} \right] k_{\text{s}} \tag{4.2}$$

and the required thermal conductivity of the solid can be solved for using Equation 4.1 to give the required k_{eff} when inputed into the homogeneous model.

4.6 Viscous Resistance Factors

The Fluent User's Guide [ANSYS, Inc., 2006] provides a empirical means of determining the inertial and viscous resistance terms using the pressure drop as a function of fluid velocity obtained from experimental data. The velocity of the fluid through the monolith, $\vec{v}$ is plotted as a function of the pressure drop across the monolith, ΔP. Figure 4.4 shows the trend between the exhaust velocity with the pressure drop. Fitting the data with a second order polynomial gives $\Delta P = 311v^2 + 134v$.

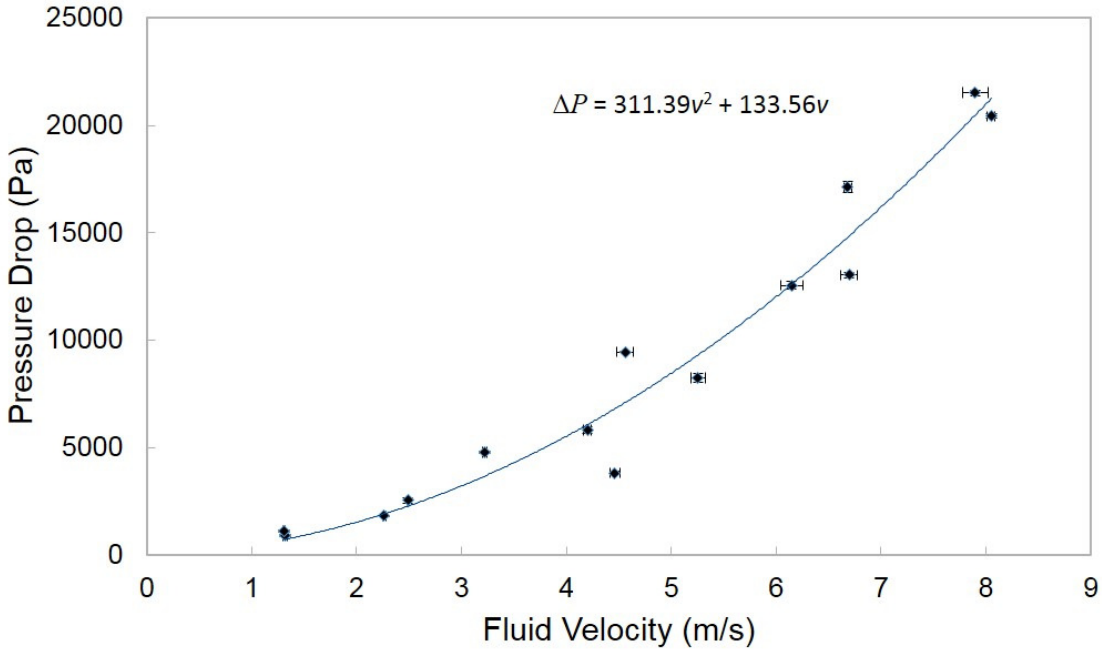

Figure 4.4: Trend used to calculate the inertial and viscous resistance factors

The pressure drop can be related to the source term by simplifying the momentum equation to yield [ANSYS, Inc., 2006],

$$\Delta P = -S \cdot L = -\left(\frac{\mu}{\alpha} + \frac{\rho C_2 |\vec{v}|}{2}\right)\vec{v} \cdot L$$

By comparing $\Delta P = 311v^2 + 134v$ to Equation 2.21, one can see that the viscous and

inertial resistance terms can be calculated by observing the following relationships [ANSYS, Inc., 2006],

$$134v = \frac{\mu}{\alpha} vL \tag{4.3}$$

$$311v^2 = \frac{\rho C_2}{2} v^2 L \tag{4.4}$$

however it is typically assumed that the inertial resistance factor should be zero (see Section 6.1.3). Because the experimental results include the pressure drop due to turbulence in the inlet diffuser and outlet nozzle, and viscous effects from the inlet and outlet pipes, the inertial resistance factor won't be zero as the flow is not strictly laminar in these sections. To correct for the location of the pressure differential sensors, pressure drop data was collected for the DOC with no monolith with the results being subtracted from the DOC containing a monolith. Figure 4.5 shows the results of subtracting the two pressure drop results and indicates a linear trend between the fluid velocity and pressure drop.

The linear trend between the fluid velocity and pressure drop suggests that the assumption of negligible inertial resistance in the monolith is valid. Because the removal of the monolith has a greater effect on the system then just removing the viscous resistance due to the monolith, the results are not exact but provide an estimate. Using Equation 2.21 and setting the inertial resistance factor to zero, the viscous resistance can be found to be $2.2(10)^8 \mathrm{m}^{-2}$. Using this value for the viscous resistance, the numerical analysis returns a pressure drop of 24.6 kPa, larger than the experimental pressure drop of approximately 12.4 ± 0.4 kPa, giving a relative difference between the experimental simulation pressure differential of 50%.

The pressure drop across the monolith can be calculated using Poisseuille's law,

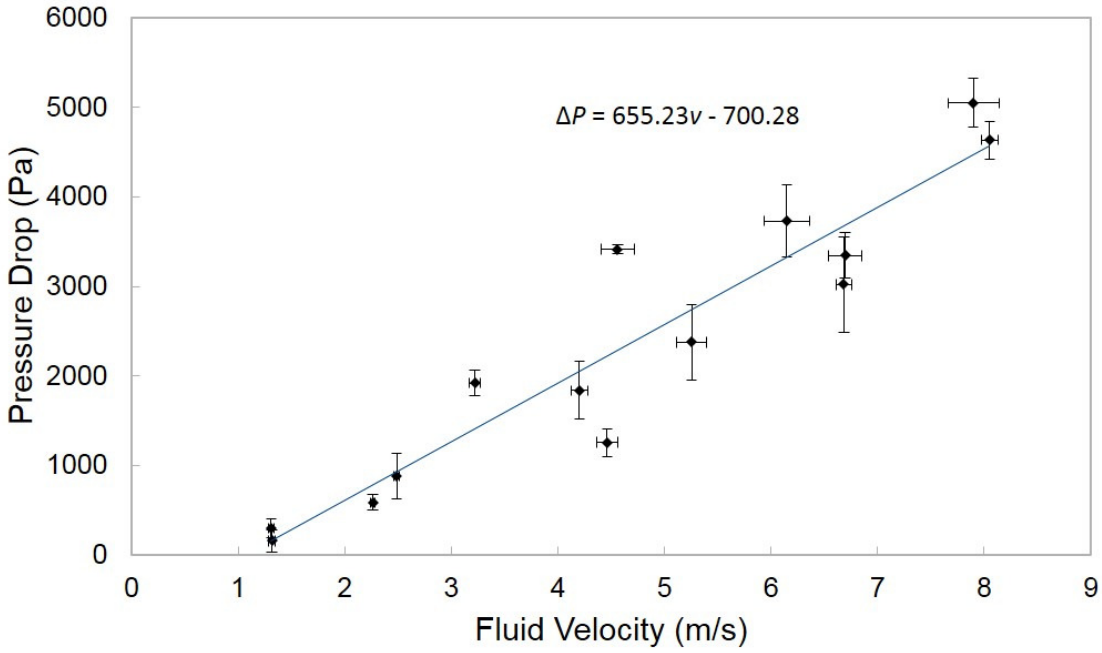

Figure 4.5: Trend used to calculate the viscous resistance factor

Equation 2.19. Combining Equation 2.19 and Equation 2.21 and using the average velocity of exhaust passing through the monolith, the viscous resistance factor can be found to be $2.2(10)^7 \mathrm{m}^{-2}$. This value for the viscous resistance factor gives a differential pressure across the DOC of 18.9 kPa compared to the experimental differential pressure of 12.4 ± 0.4 kPa. A relative difference of 34% between the simulation and experimental pressure differential is much larger than desired however attempts to increase the accuracy of the pressure drop resulted in abnormal flows through the DOC and negatively affected the temperature profile.

The difference in pressure drop between the numerical model and the experimental results can be attributed to the complex flows in the inlet diffuser not being accurately captured by the numerical model. Furthermore, the monolith is being approximated as a porous region and this approximation is likely to introduce error that could reduce the accuracy of the model. To increase the accuracy of the model, more complex models need to be employed to determine the flow characteristics through

the square channels of the monolith.

4.7 Mesh Dependency

To validate the results of the numerical analysis, a mesh dependency was performed to ensure that the mesh size was sufficiently fine so as to not introduce any significant error. The pressure differential across the DOC was found at increasing degrees of freedoms. Figure 4.6 illustrates that the solution converges when the number of elements exceeds 50000.

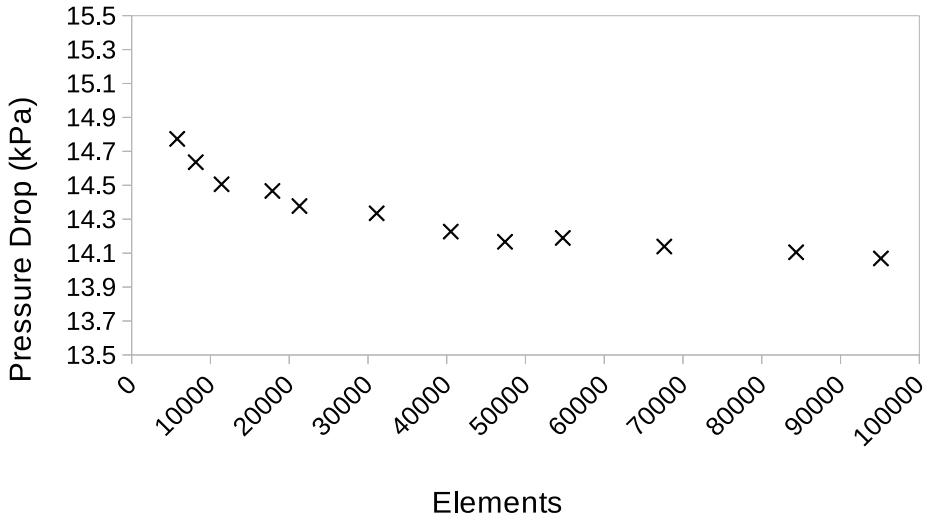

Figure 4.6: Mesh dependency results showing convergence of the solution

This model will be using in Chapter 6 to predict the steady state pressure drop across the DOC, the steady state temperature profile of the monolith, and the transient temperature response of the monolith. The results will be compared to the experimental results to validate the model and to provide further evidence to support the experimental results.

Chapter 5

Experimental Flow Characterization

This Chapter details the flow characteristics through the Diesel Oxidation Catalyst and the temperature characteristics of the Diesel Oxidation Catalyst during heating and cooling.

5.1 Steady State Pressure Drop

Engine tests were carried out to determine what effect adding an insulation ring to the monolith of the DOC would have on the overall pressure drop and the radial temperature profile. It is hypothesized that the insulation ring decreases the pressure drop by reducing the turbulence in the inlet diffuser and outlet nozzle while maintaining a higher temperature in the monolith leading to faster light-off. The greatest reduction in pressure drop is expected for the insulation ring diameter similar to the inlet diameter of the diffuser which aids in maintaining a jet passing through the central portion of the DOC and limiting the turbulence in the inlet diffuser. The pressure drop across the DOC is measured for each of the four DOCs described in Section 3.5 and at each of the operating points listed in Section 3.7.

Steady state operation is achieved when the exhaust temperature downstream of the DOC reaches a constant value $\pm 1°C$. The differential pressure across the DOC is sampled at 1 Hz with the pressure drop calculated as the mean over the subsequent

10 seconds. Each test is repeated six times for each of the 14 operating points and for each of the four DOCs. Since the engine speed can not be precisely controlled and the stock engine controller makes continuous adjustments, the pressure drop is plotted as a function of the exhaust volumetric flow rate. The uncertainty in the pressure drop and flow rate are calculated using a t-distribution with a 95% confidence interval.

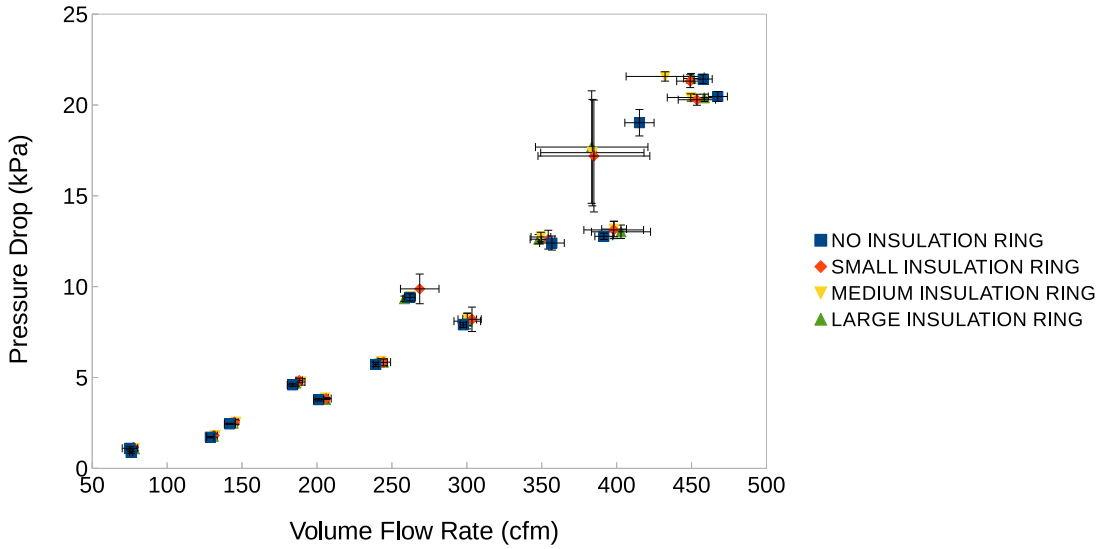

Figure 5.1: Pressure drop for each of the four DOCs connected to the Diesel engine

Figure 5.1 indicates that any effect the insulation ring may have on the overall pressure drop across the DOC is too small to be statistically significant. Pulsations in the exhaust flow, created by the opening and closing of the exhaust valves and continuous changes made by the stock engine controller mask any differences in pressure drop between the various insulation ring sizes.

To eliminate the instabilities caused by the engine, a blower was connected in place of the Diesel engine. A pitot tube is installed upstream of the DOC to measure the flow rate of air and the blower is operated at a constant flow rate of 215 $\pm$ 4 cfm. Each of the four insulation rings were tested to determine whether the cold flow tests using the blower would demonstrate any difference in pressure drop.

The effect of the insulation ring on the pressure drop across the DOC for the blower tests is shown in Figure 5.2. Any difference in pressure drop between the various sizes of insulation ring in the DOC is smaller than the uncertainty in the pressure drop. The effect of the insulation ring on the pressure drop remains inconclusive as neither the engine nor blower tests indicated any statistically significant difference in pressure drop.

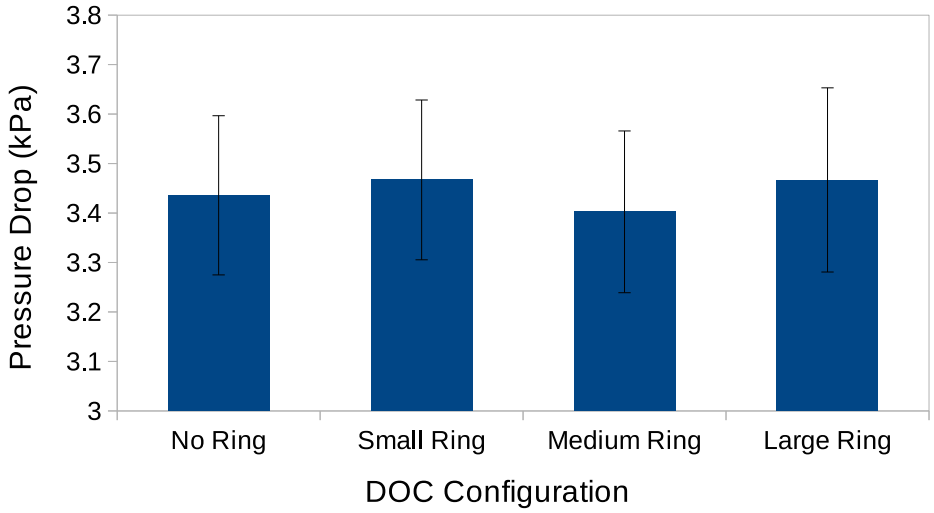

Figure 5.2: Cold flow pressure drop results for each of the four DOCs

5.2 Steady State Temperature Profile

The temperature profile across the DOC is obtained by inserting thermocouples into the exhaust downstream of the DOC and feeding them upwards into the monolith to a depth of approximately 1 cm, at known radial locations in the monolith (see Section 3.6. The tests were performed for each of the 14 operating points and each of the four DOCs.

Figure 5.3 shows that the radial temperature profile during steady state operation is symmetric with the highest temperatures towards the centre of the DOC and lowest temperatures along the exterior wall of the DOC as expected. Figure 6.3d indicates

that the temperature around the centre of the DOC with the large insulation ring tends to plateau rather then having a defined peak, suggesting that the insulation ring acts to retain energy at the centre of the DOC.

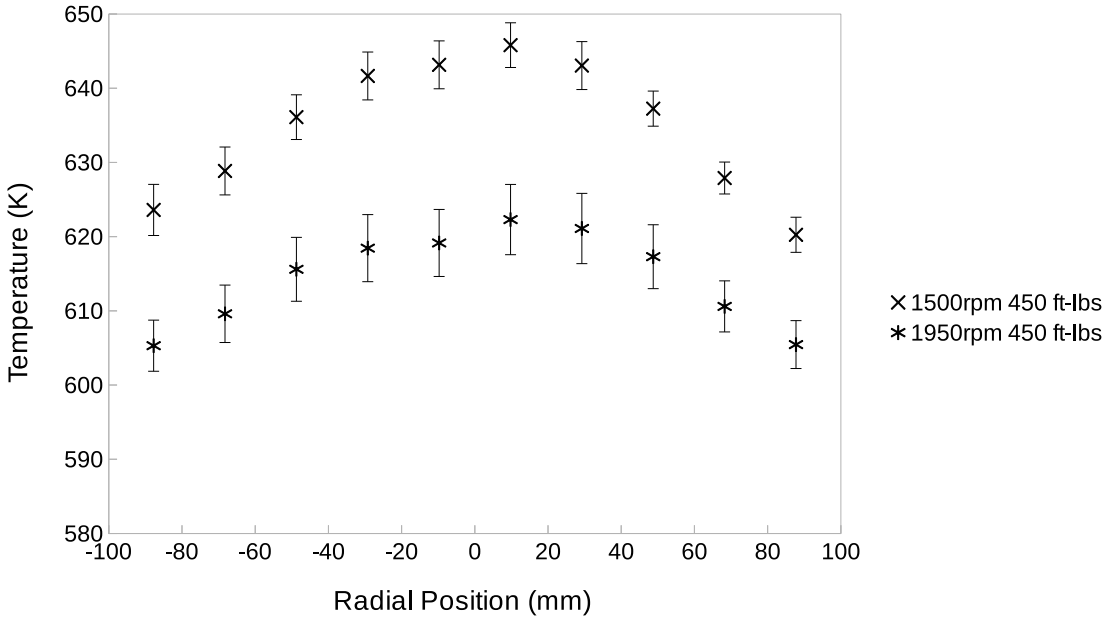

(a) No Insulation Ring

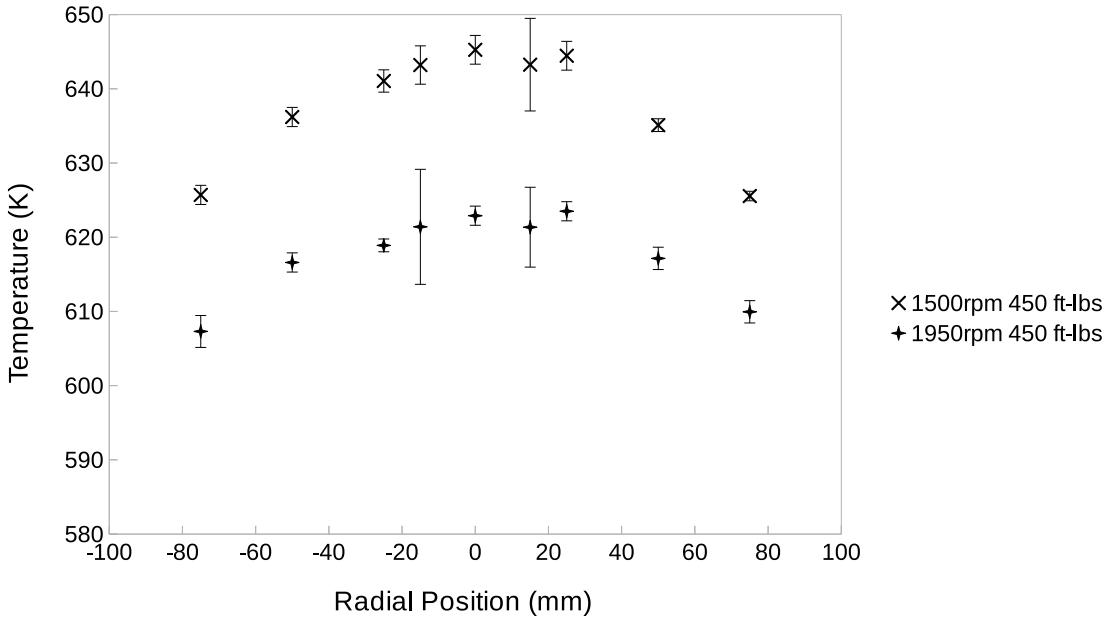

(b) Small Ring at r = 20.5-23 mm

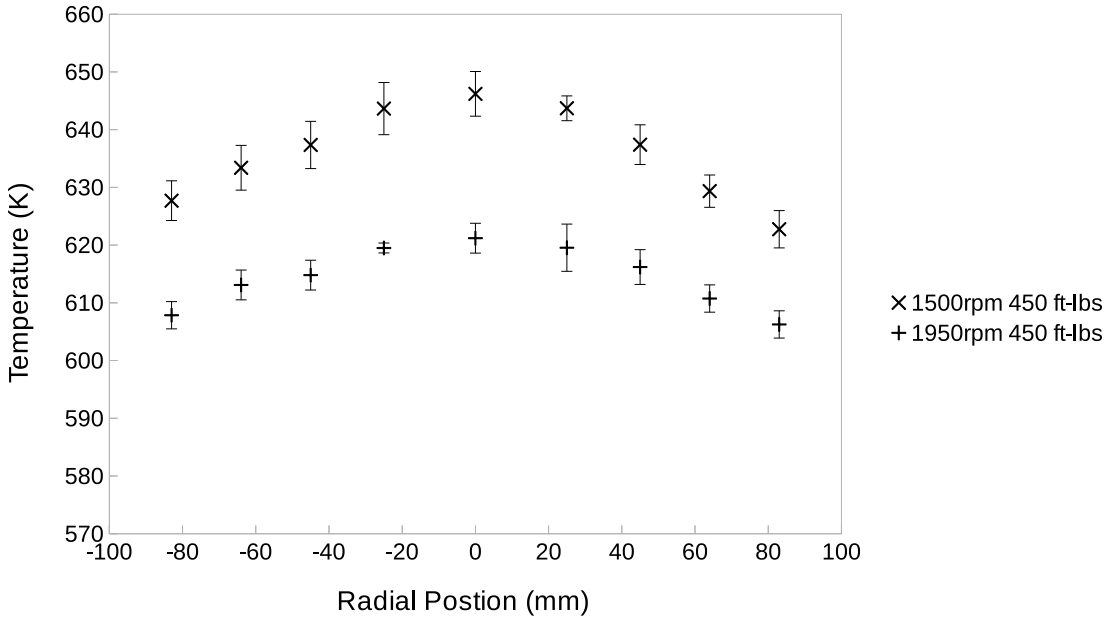

(c) Medium Ring at r = 32.5-35 mm

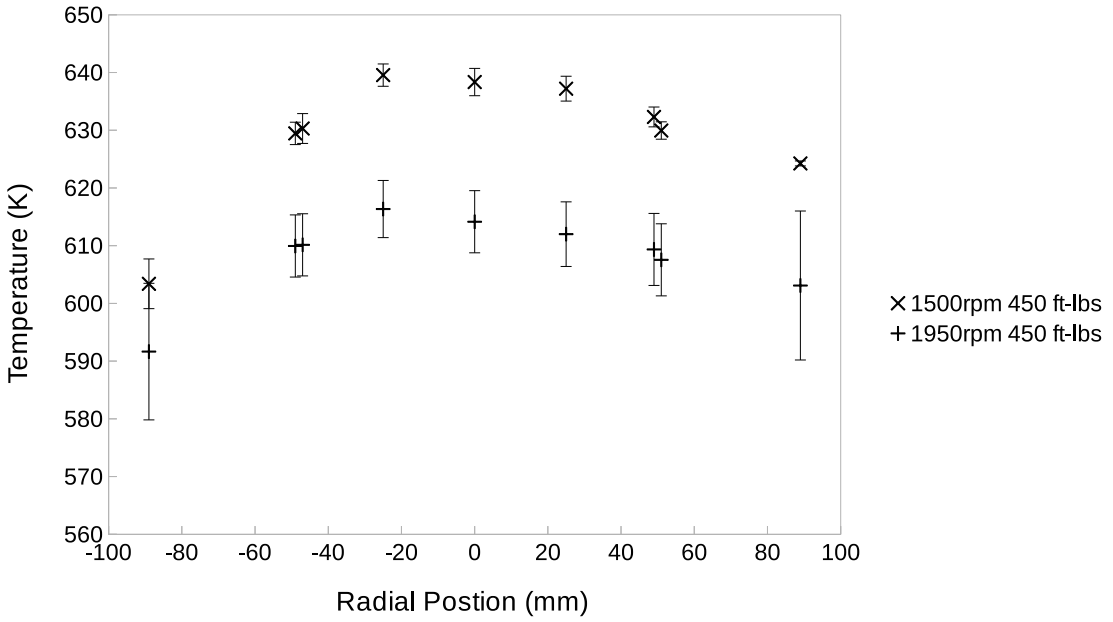

(d) Large Ring at r = 49.5-52 mm

Figure 5.3: Radial temperature profile of the downstream side of the DOC monolith

The maximum temperature achieved by the DOC during steady state testing is shown in Figure 5.4. Each of the four DOCs containing different sized insulation rings

show no noticeable difference in maximum temperature at any of the 14 operating points.

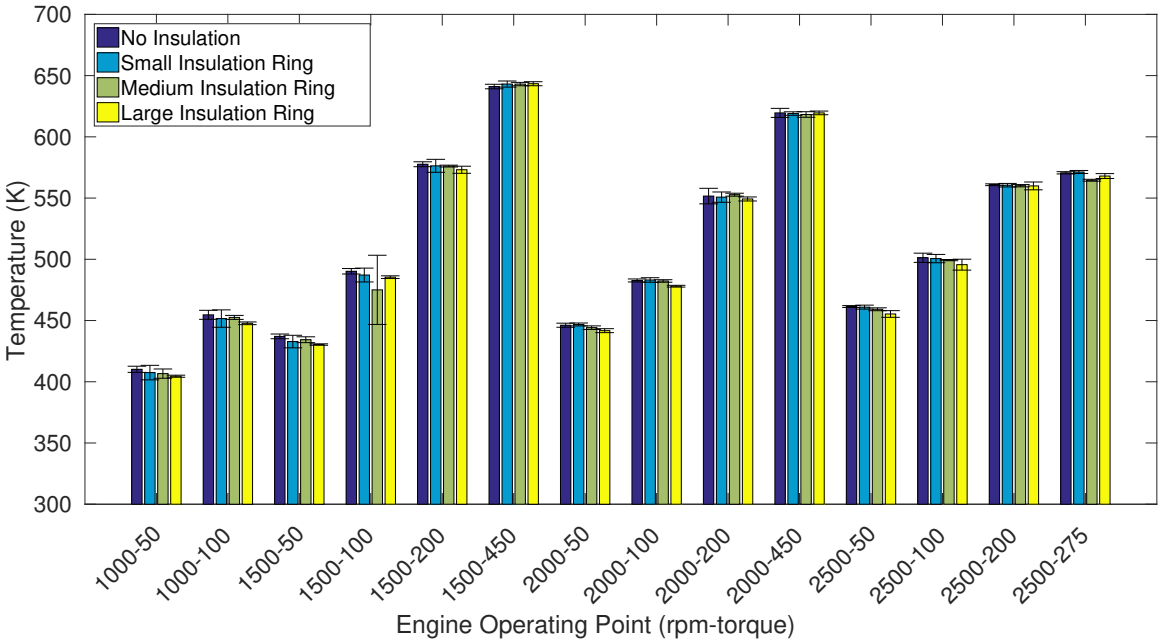

Figure 5.4: Maximum DOC temperature at steady state

The results from the steady state tests indicate the temperature in the DOC demonstrates a symmetrical pattern about the centre of the DOC. Transient temperature tests are reliant on the symmetry of the temperature profile as the thermocouples were located solely on one half of the DOC to maximize the points at which the temperature is measured as the number of thermocouples that can be inserted into the DOC is limited.

5.3 Transient Temperature Profile

The temperature profile of each of the four DOCs is recorded as a function of time for each of the 14 operating points. The temperature of the DOC is recorded on the downstream side of the monolith at 11 radial locations, located along one half of the DOC. The thermocouples are inserted approximately 1 cm into the monolith at known radial locations, as described in Section 3.6, so that the thermocouple's locations are the same for all of the tests. The steady state tests in Section 6.1.4 indicated that the temperature profile is symmetric and it is assumed that a symmetric profile will occur for the transient tests, allowing all thermocouples to be placed on one half of the DOC.

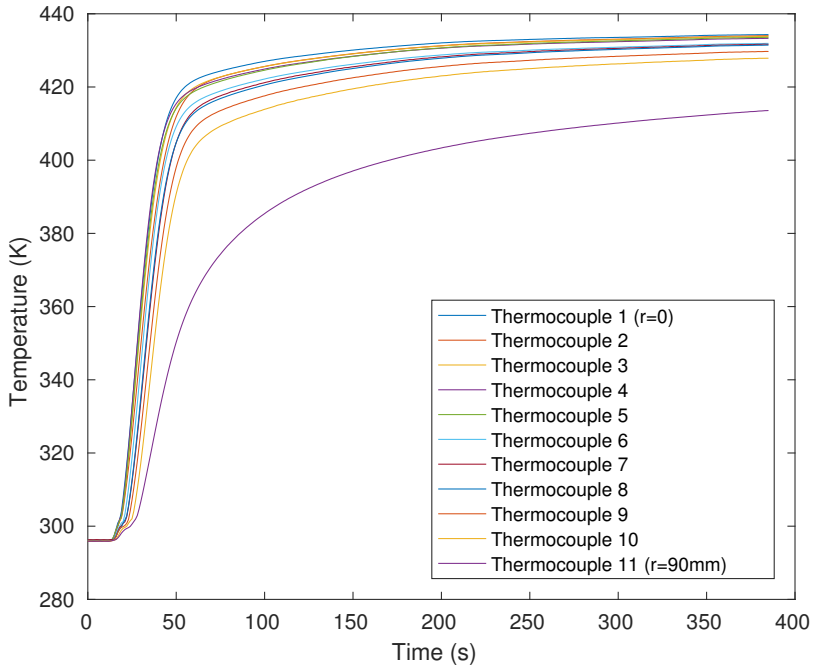

(a) No Insulation Ring

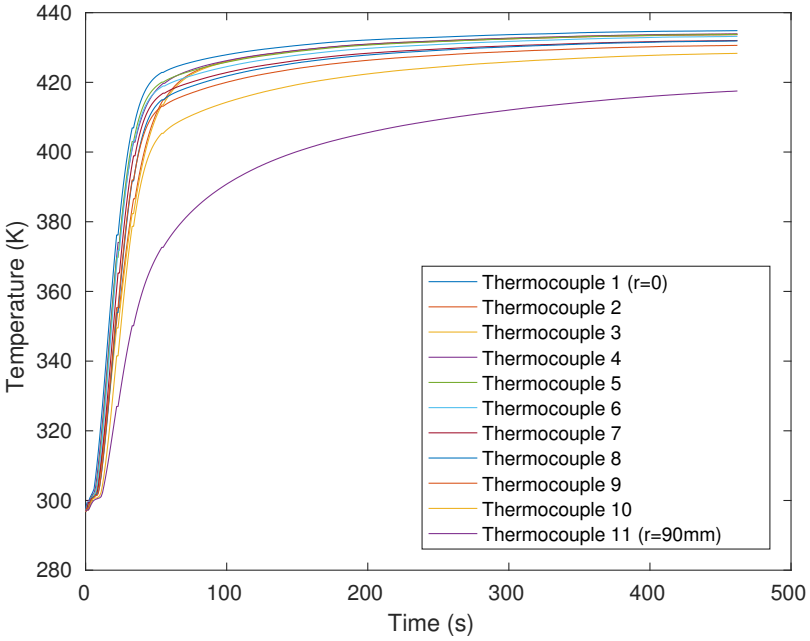

(b) Small Ring at r = 20.5-23 mm

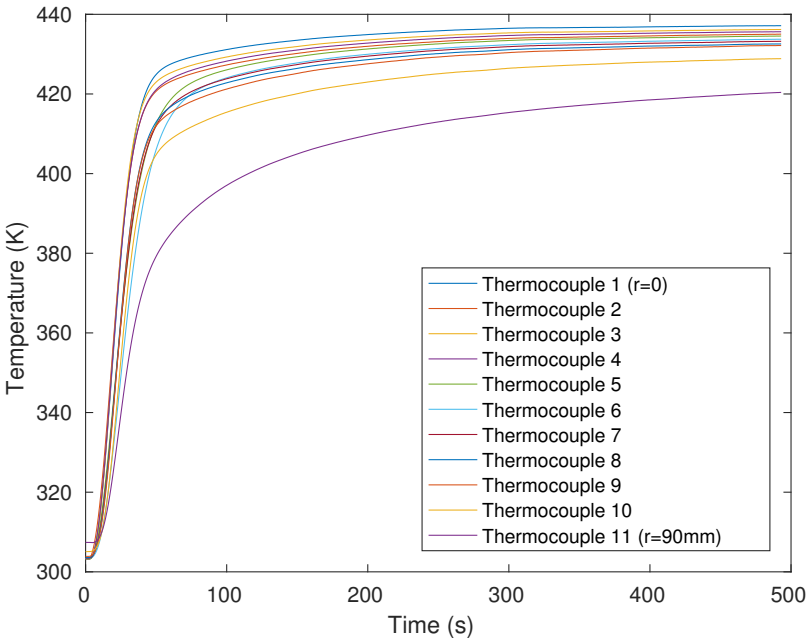

(c) Medium Ring at r = 32.5-35 mm

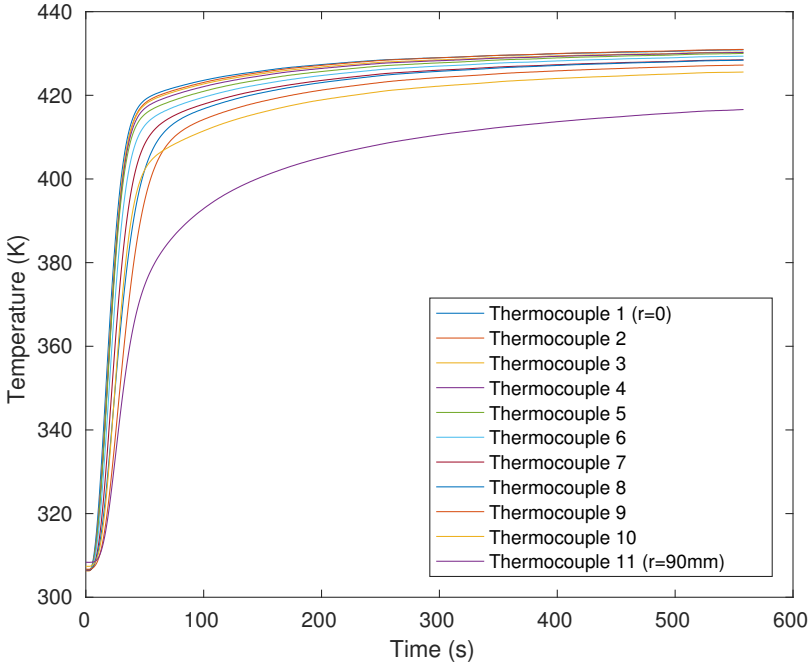

(d) Large Ring at r = 49.5-52 mm

Figure 5.5: Radial temperature profile of monolith at 1500 rpm and 50 ft-lbs (68 Nm)

The temperature profile in Figure 5.5a demonstrates the expected heating trend of the monolith with the thermocouple at the centre of the monolith heating fastest and reaching the highest steady state temperature. The greater the radial distance from the centre of the monolith the slower the heating and the lower the steady state temperature.

The DOCs containing an insulation ring show a different heating profile and the thermocouples located directly adjacent to the insulation ring showing the greatest difference. The thermocouples located directly next to the insulation ring show a slower rate of heating as shown in Figures 5.5b through 5.5d and Table 5.1 lists the thermocouples that are located adjacent to the insulation ring. Despite the slower rate of heating for the thermocouples adjacent to the insulation ring, the steady state temperature remains the same as if there were no insulation ring.

The decreased rate of heating is further demonstrated in Figure 5.6. Figure 5.6a

Table 5.1: List of thermocouples located next to the insulation ring

DOC Configuration	Thermocouple
Small Insulation Ring (Figure 5.3b)	2 and 3
Medium Insulation Ring (Figure 5.3c)	5 and 6
Large Insulation Ring (Figure 6.3d)	9 and 10

shows that the rate of DOC heating does not decrease uniformly from the centre of the DOC to the wall of the DOC but rather the rate of heating occurs fastest at the centre of the DOC and approximately 30 mm from the centre of the DOC. This suggests that there is a larger flow rate of exhaust passing through these two locations of the DOC and increasing the amount of available energy. The increased flow rate at approximately 30 mm corresponds to the inlet diameter of the diffuser and is likely a result of the turbulent flow into the monolith.

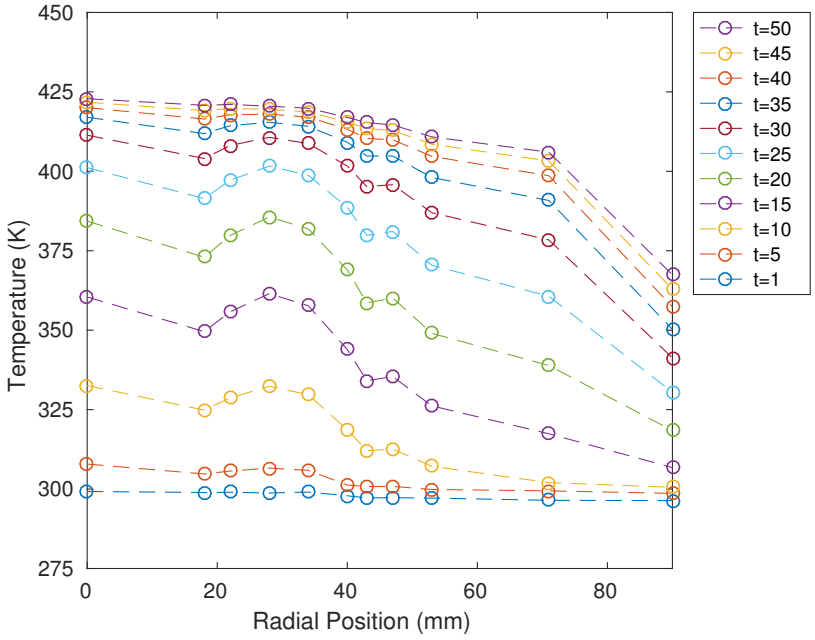

(a) No Insulation Ring

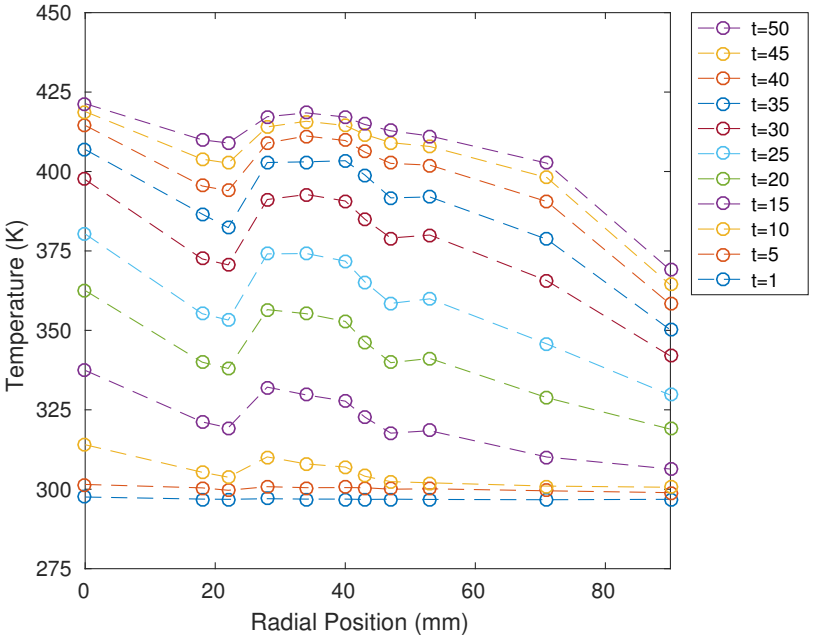

(b) Small Ring at r = 20.5-23 mm

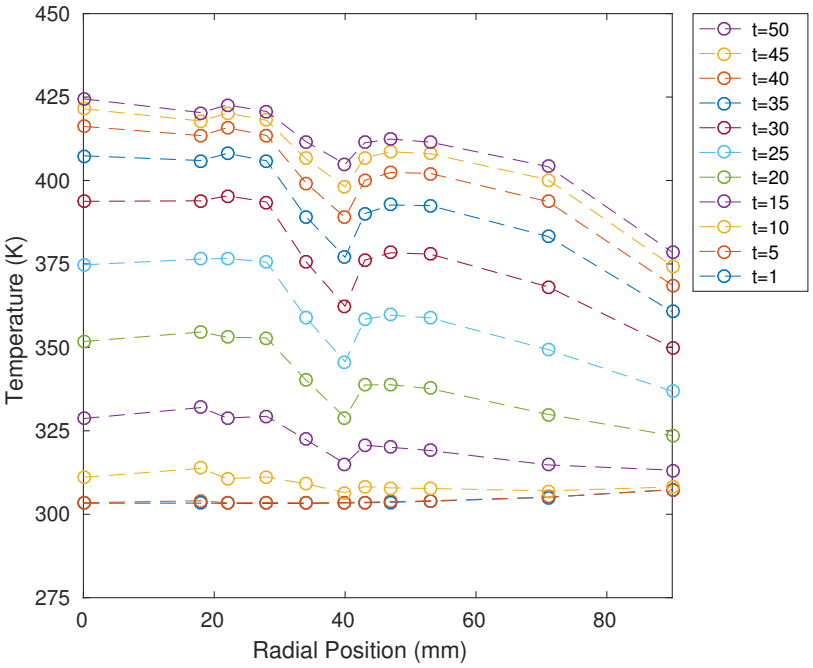

(c) Medium Ring at r = 32.5-35 mm

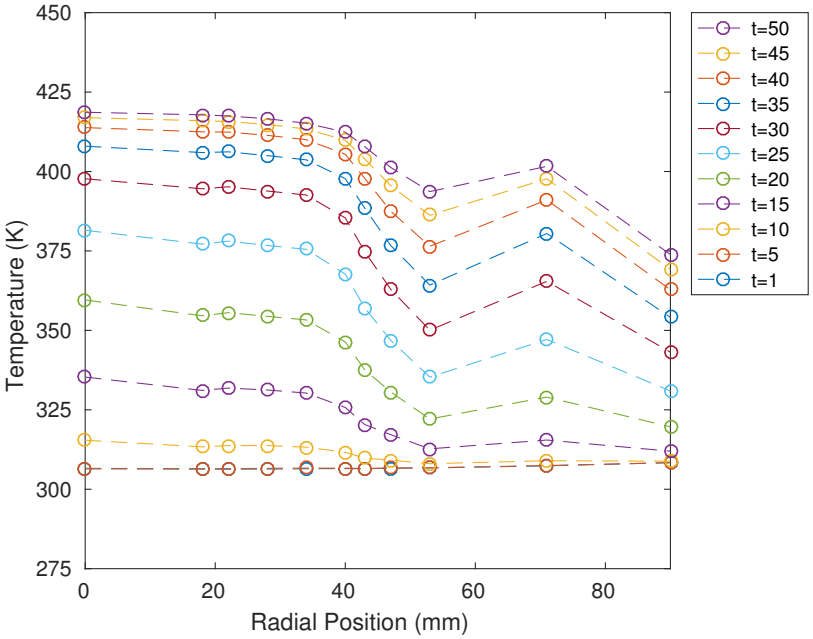

(d) Large Ring at r = 49.5-52 mm

Figure 5.6: Radial temperature profile of DOC during heat up for 50 seconds

5.4 DOC Energy Absorption

To determine the effect of the insulation ring on the energy absorbed by the DOC, the energy absorbed by each of the four DOCs was found for each of the 14 operating points. The energy absorbed by the DOC, $\dot{E}$, is given by,

$$E = \int_0^t C_p(T)\dot{m}\Delta T dt \tag{5.1}$$

where $C_p(T)$ is the temperature dependent specific heat capacity of the exhaust, $\dot{m}$ is the mass flow rate of exhaust through the DOC, ΔT is the temperature difference between the exhaust measured upstream and downstream of the DOC, and t is the time. For a discrete system, the energy absorbed can be calculated by,

$$E = \sum_{0}^{t} C_p(T)\dot{m}\Delta T\Delta t \tag{5.2}$$

where Δt is the sampling step size. The specific heat capacity of the exhaust is approximated using the specific heat of air and calculated using the following [Cengel and Boles, 2011],

$$C_p(T) = a + bT + cT^2 + dT^3 \qquad \text{(kJ/(kmol-K))} \tag{5.3}$$

where the coefficients in Equation 5.3 are given as [Cengel and Boles, 2011]:

Table 5.2: Coefficients used to calculate $C_p(T)$

Coefficient	Value
a	28.11
b	$0.1967(10)^{-2}$
c	$0.4802(10)^{-5}$
d	$-1.966(10)^{-9}$

Energy transfer from the DOC to the surroundings is calculated by determining the rate of energy absorption by the DOC at steady state since the energy absorbed by the DOC at steady state is equal to the energy lost to the surroundings. To calculate the energy transfer to the surroundings during the transient phase, a linear interpolation is used to give an approximate rate of energy transfer. Because the rate of energy transfer to the surroundings is not linear with temperature, some degree of error is introduced, but because the rate of heating is approximately the same for each of the four DOCs for the same operating point, the relative difference between the DOCs can be compared.

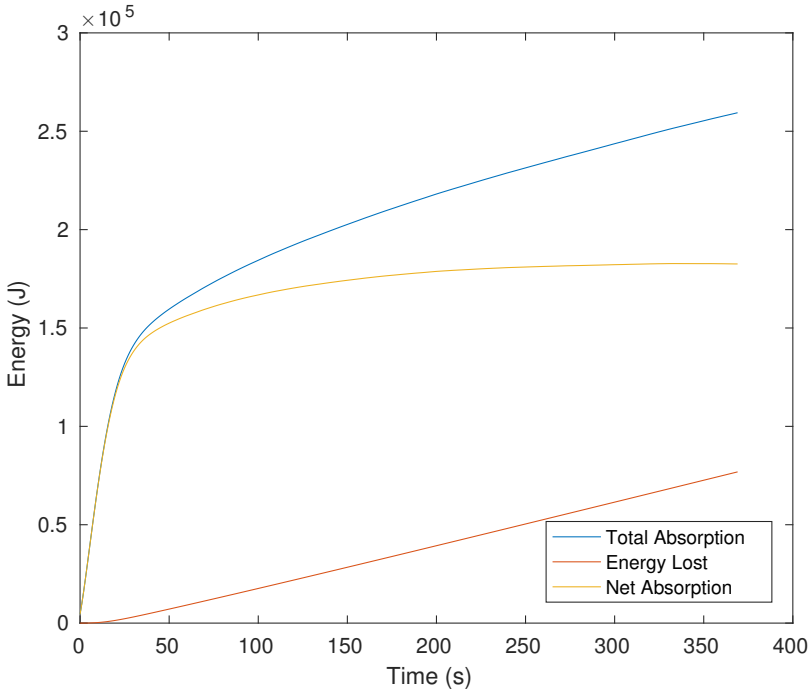

(a) No Insulation Ring

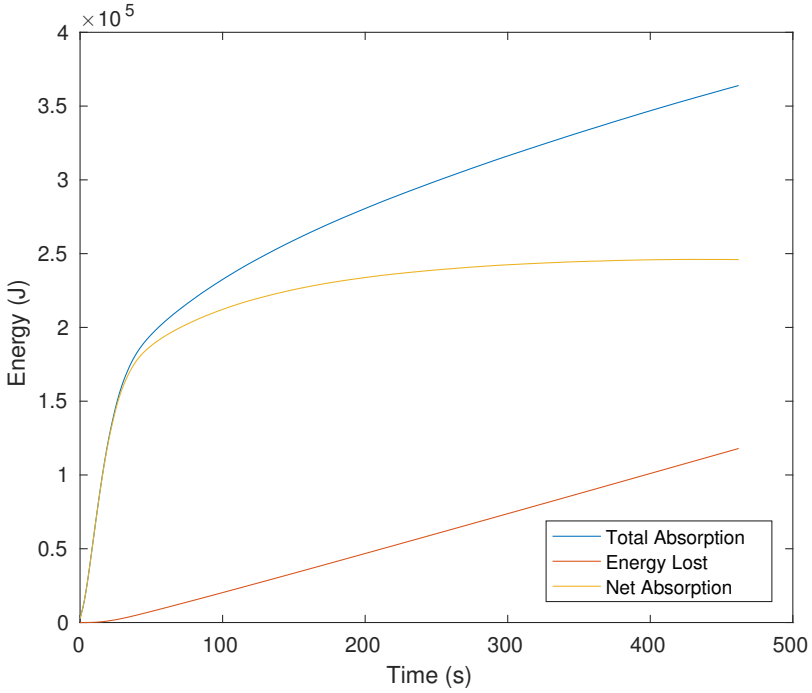

(b) Small Ring at r = 20.5-23 mm

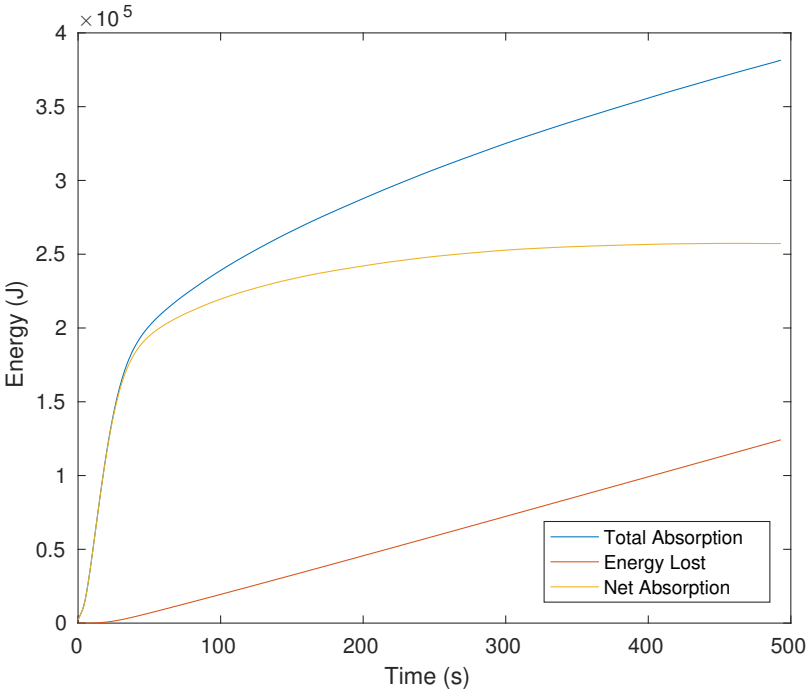

(c) Medium Ring at r = 32.5-35 mm

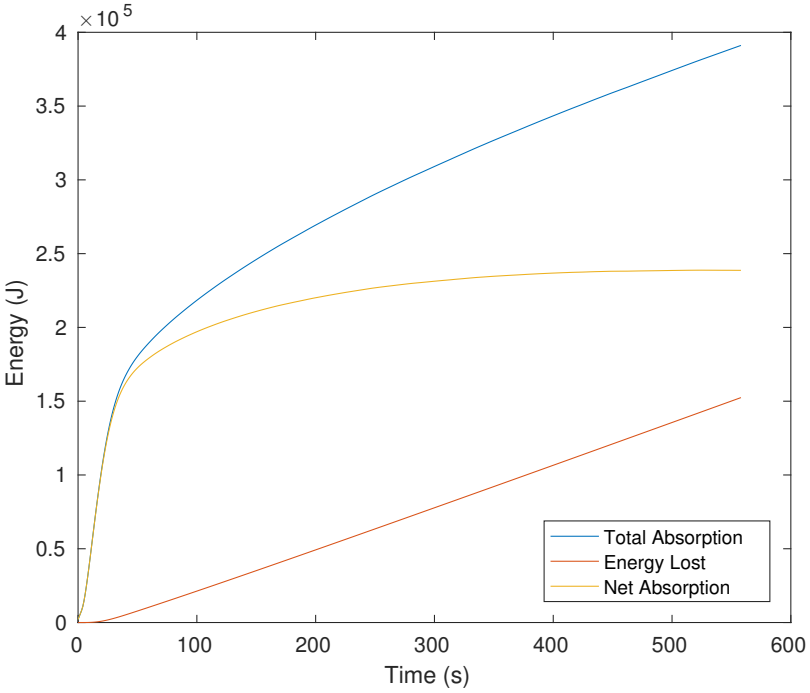

(d) Large Ring at r = 49.5-52 mm

Figure 5.7: Energy absorption of the four DOCs

The cumulative energy absorbed by each of the four DOC configurations and the cumulative estimate of energy lost to the surroundings is shown in Figure 5.7. The energy absorbed by the DOC at steady state is linear as the energy transferred to the surroundings remains constant for a constant temperature differential. Figure 5.8 shows the energy absorbed by each of the four DOC configurations for each of the 14 operating points. The DOC containing no insulation ring absorbs less energy than the three DOC configurations containing insulation rings. This is expected as the insulation ring increases the overall mass of the DOC and subsequently the overall heat capacity of the DOC.

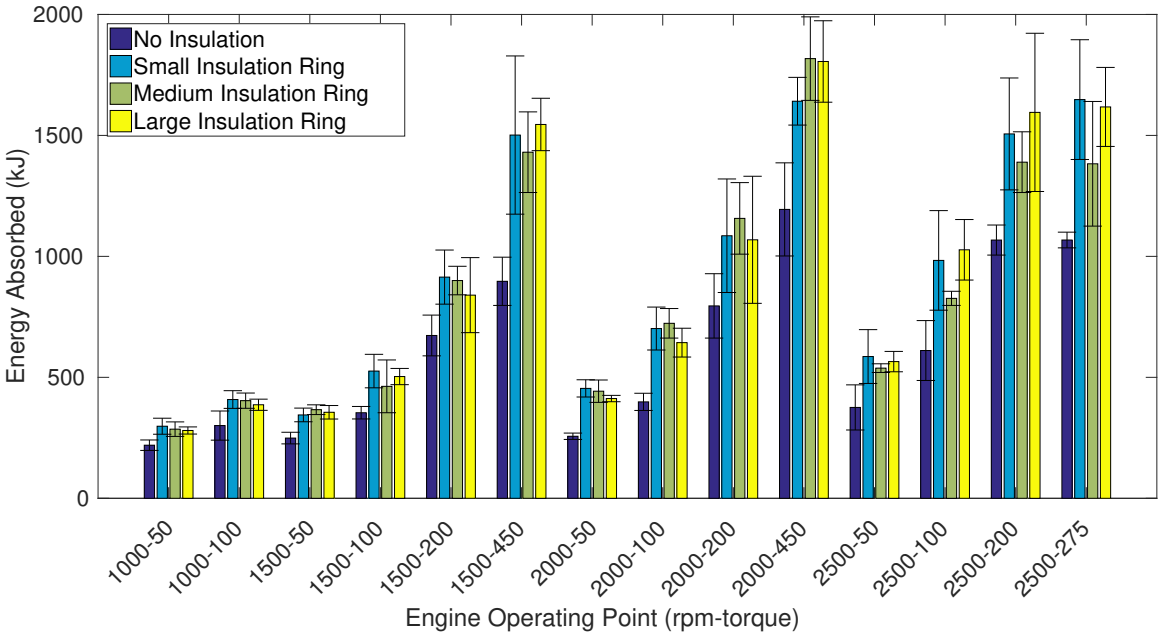

Figure 5.8: Energy absorbed by DOC from cold start to steady state

Figure 5.4 shows the maximum temperature achieved by each of the four DOC configurations at each of the 14 operating points. Each of the four DOC configurations show no significant difference at any of the operating points. This is expected since the maximum temperature of the DOC is a product of the exhaust temperature, however the total energy absorbed by the DOC and the time required to reach the maximum temperature are both expected to increase with the addition of the insulation ring.

Figure 5.9a indicates that the time to reach 95% of the steady state temperature is greater for the three DOC configurations containing an insulation ring. Furthermore, Figures 5.9b through 5.9d illustrate that the time required to reach 85%, 75%, and 50% the steady state temperature are even greater for the DOC configurations containing insulation rings. The delay in heating of the DOC is likely to negatively affect the light-off characteristics of the DOC.

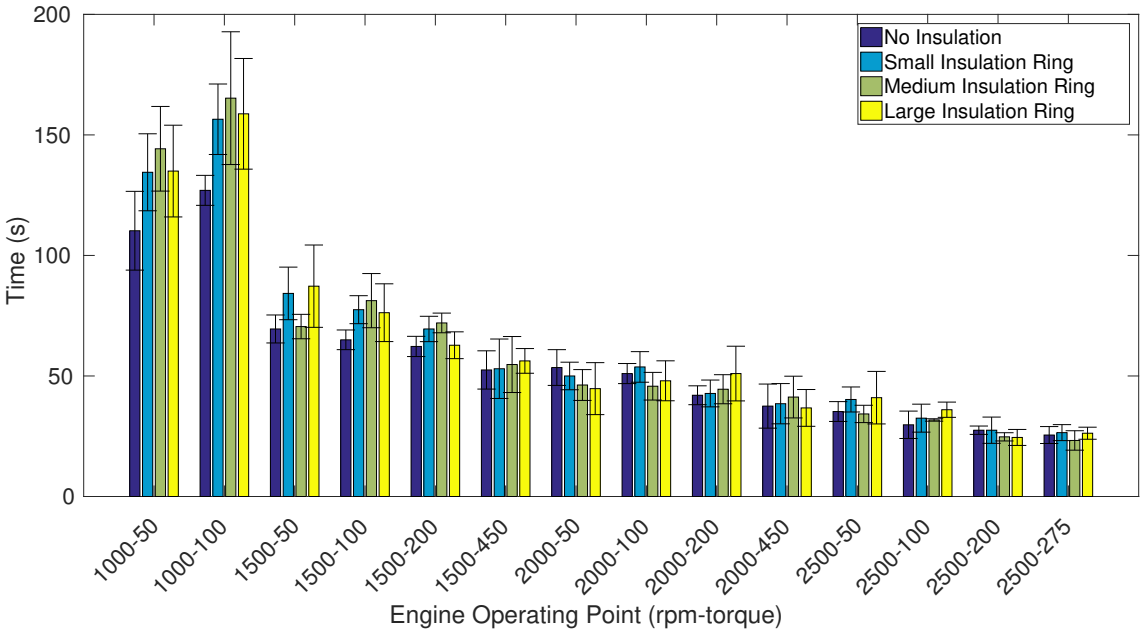

(a) Time required for DOC to reach 95% of steady state temperature

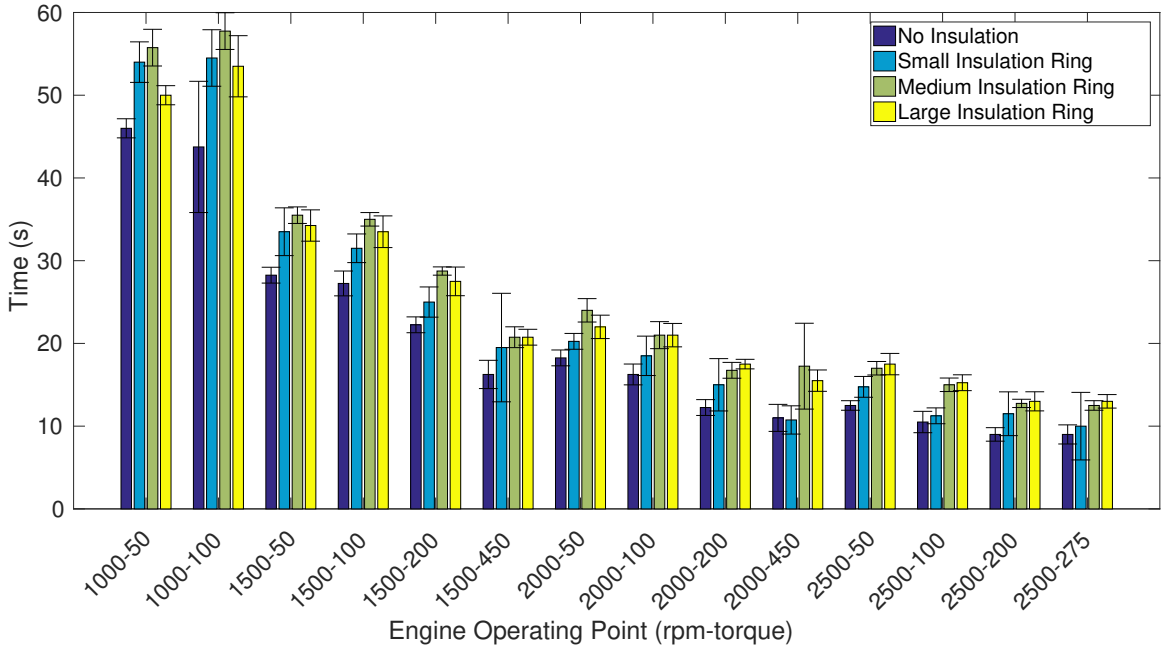

(b) Time required for DOC to reach 85% of steady state temperature

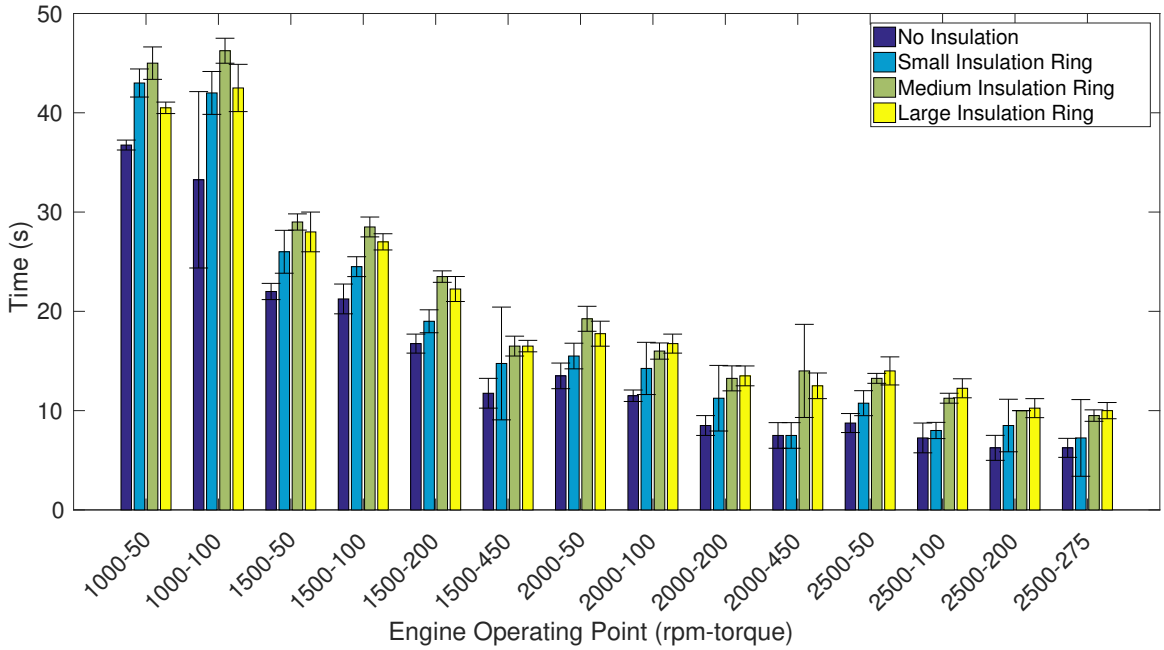

(c) Time required for DOC to reach 75% of steady state temperature

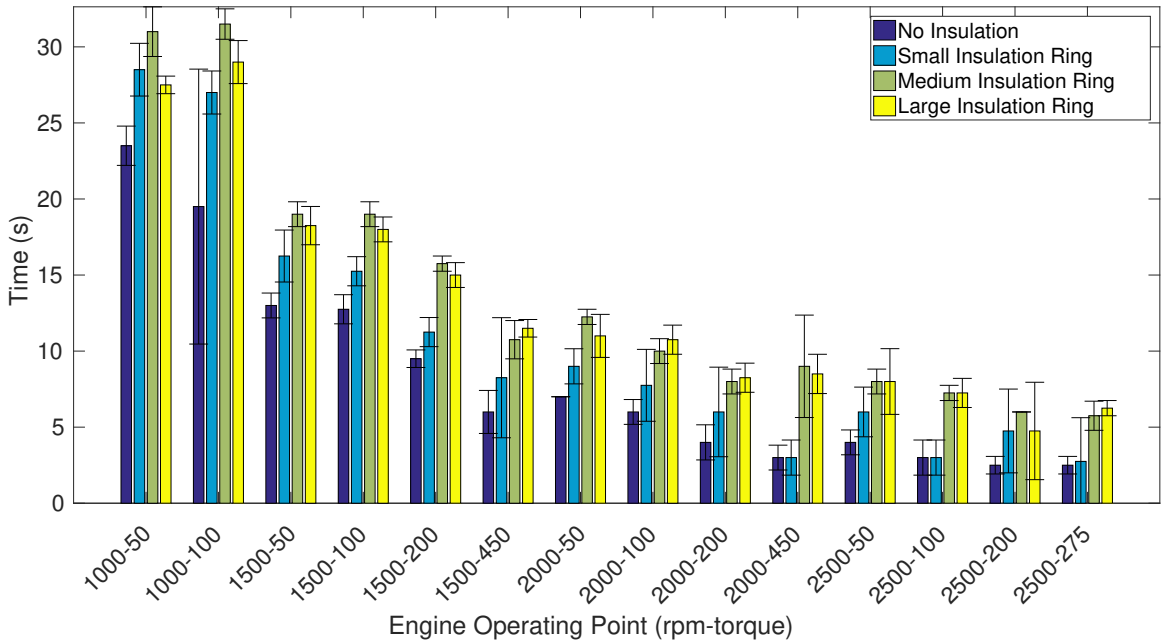

(d) Time required for DOC to reach 50% of steady state temperature

Figure 5.9: Comparison of the heat up time of the DOC

Increasing the time to reach light-off increases the amount of NO_x, CO, and HC being emitted to the atmosphere during cold start. However, it is hypothesized that the insulation ring tends to direct greater amounts of the exhaust flow through the central region of the DOC increasing the rate of heating for the core of the DOC. This in turn decreases the time required to reach light-off as the majority of the emissions will be converted in the central portion of the DOC with only a fraction of the exhaust passing through the radial portions of the DOC. This effect needs to be further explored to fully determine whether the insulation ring increases or decreases the time required to achieve light-off using a monolith with a washcoat and active catalyst.

5.5 Experimental Limitations

The experimental setup demonstrated a number of drawbacks that limited the conclusions that could be formed and will be outlined for future work along with suggested changes. By improving the current experimental setup, future work will be able to draw more definitive conclusions.

The exhaust bypass described in Section 3.4 allows the engine to be warmed to steady state without heating the DOC. When the engine reaches steady state the exhaust valve to the DOC can be opened and the bypass closed. The intended purpose is to creating a step input in the exhaust gas temperature passing through the DOC. The valves were only partially capable of isolating heat transfer to the DOC as under high temperatures (600 K) and high exhaust flow rates (200 g/s) the valves would not seal completely. Although this had little effect on steady state testing, the uncertainty in the transient test results was adversely affected. Valves used for the exhaust bypass should be intended for high temperature application but also be able to handle large variations in temperature (300 K to 600 K).

Pulsations in the exhaust gas occurring due to the opening and closing of the exhaust valves and automatic changes made by the stock engine controller increases the uncertainty in the exhaust gas flow rate. In order to reduce the pulsations it has been suggested that multiple blank catalysts can be used upstream to dampen the pulsations or a hot flow bench with a constant flow rate can be used in place of the engine.

Chapter 6

Simulation Based Flow Characterization

This Chapter details the results of the numerical analysis to define the flow characteristics through the Diesel Oxidation Catalyst, including the pressure drop and heating characteristics. Both steady state and transient numerical models are discussed.

6.1 Steady State Numerical Model

The addition of an insulation ring to the monolith of the DOC is examined to determine if there exists a difference in the overall pressure drop across the DOC and whether the temperature profile is affected. By reducing the pressure drop across the DOC the back pressure on the engine can be reduced leading to increased engine efficiency.

6.1.1 Steady State Setup

The model is setup using an exhaust flow rate of 175 g/s, similar to the exhaust flow rate from the Cummins QSB4.5 Diesel engine at 1500 rpm and 610 N/m (450 ft-lbs) (see Section 3.2). The pulsations that occur in the exhaust due to the opening and closing of the exhaust valves are ignored to simplify the numerical model. The monolith is modeled as a porous region with axial flow being imposed by setting the viscous resistance value in the radial direction to a minimum of three orders of

magnitude larger than the viscous resistance value in the axial direction, as described in Section 4.

The pressure drop across the DOC is calculated by taking the difference of the pressure 150 mm upstream of the diffuser inlet to the pressure 150 mm downstream of the nozzle exit. The locations are similar to the location of the pressure transducers in the experimental setup (see Section 3.6).

6.1.2 Mass Flow Profile

The mass flow profile in the monolith was calculated using the velocity profile from the numerical model, the cross-sectional flow area for each of the DOC configurations, and the exhaust density assuming incompressible flow. Incompressible flow is widely accepted in modeling of exhaust gases in the DOC as the velocity of the exhaust gases do not exceed 1/20th of the speed of sound [Ozhan et al., 2014], acoustic waves have little effect on the overall flow [Chakravarthy et al., 2003], and local pressure fluctuations do not exceed 1/10th of the absolute pressure [Holmgren et al., 1997]. The velocity profile of the exhaust is shown in Figure 6.1 where the locations of zero velocity coincide with the locations of the insulation rings.

The velocity profile shows a slight increase in the velocity at the centre of the monolith, with a pronounced increase for the medium sized insulation ring and a lesser increase for the small insulation ring. The addition of the medium insulation ring to the monolith appears to direct larger amounts of exhaust through the centre of the monolith. The large insulation ring shows little difference to the monolith with no insulation ring, which is likely a result of being larger in diameter than the jet that is created in the inlet diffuser (see Section 2.5.3) decreasing its effect on the exhaust flow through the DOC.

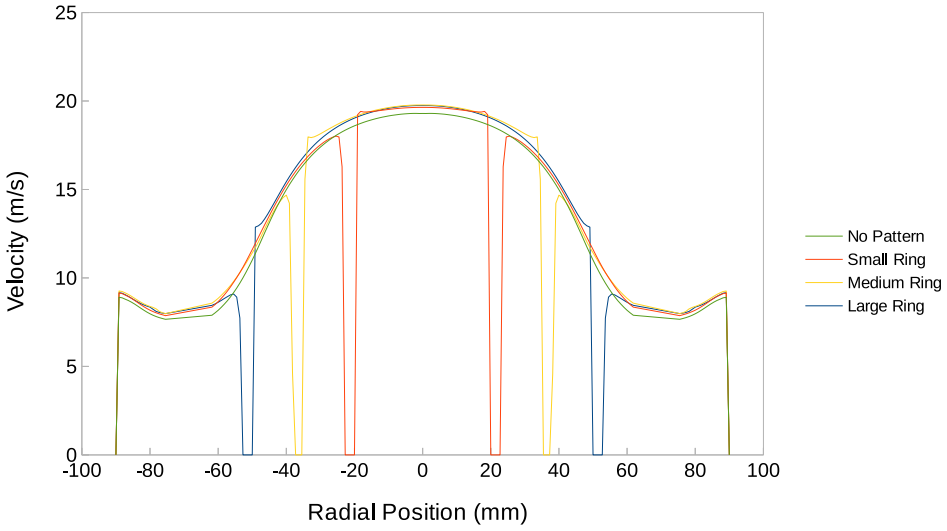

Figure 6.1: Velocity profile of exhaust gases passing through the monolith

6.1.3 Pressure Drop

The pressure drop results for each of the four DOC configurations are taken from the numerical analysis and shown in Figure 6.2. The results indicate that the addition of an insulation ring to the monolith increases the overall pressure drop across the DOC. The increase in pressure drop is expected as the insulation ring decreases the cross-sectional flow area while the overall mass flow rate remains constant. This leads to an increase in the viscous resistance due to the increase in fluid velocity and a corresponding increase in pressure drop.

The large insulation ring shows a slightly lower pressure drop than the medium insulation ring despite the smaller flow area. This is likely due to a lower flow rate through the channels in the radial portion of the monolith, as shown in Figure 6.1, further indicating that the diameter of the large insulation ring is larger than the jet formed in the inlet diffuser limiting its ability to affect the flow.

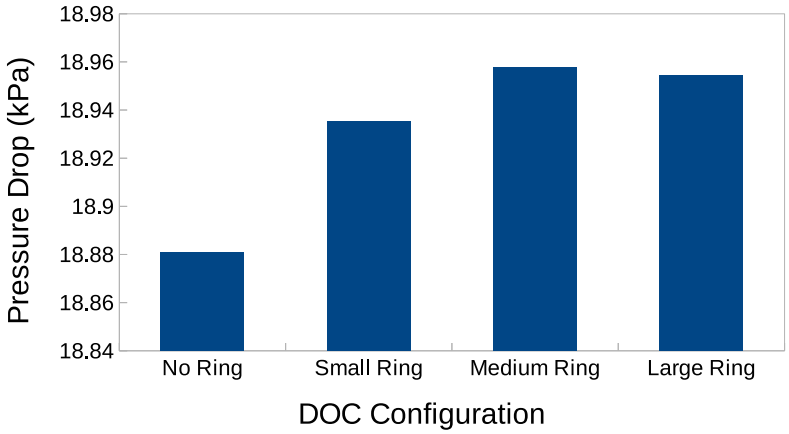

Figure 6.2: Pressure drop across the DOC for each of the DOC configurations

6.1.4 Steady State Temperature Profile

The temperature profile was found 1 cm upstream from the downstream face of the monolith, similar to the location of the thermocouples in the experimental tests, allowing the results to be easily compared (see Section 3.6). The parameters used in the numerical analysis are found in Chapter 4.

The steady state temperature profile was plotted along with the experimental temperature data for the operating point of 1950 rpm and 200 ft-lbs, which produces an exhaust flow rate of 0.18 $\pm$ 0.03 kg/s, similar to the flow rate of 0.175 kg/s used by the numerical model. Figure 6.3 illustrates the ability of the numerical model to accurately predict the temperature profile of the monolith.

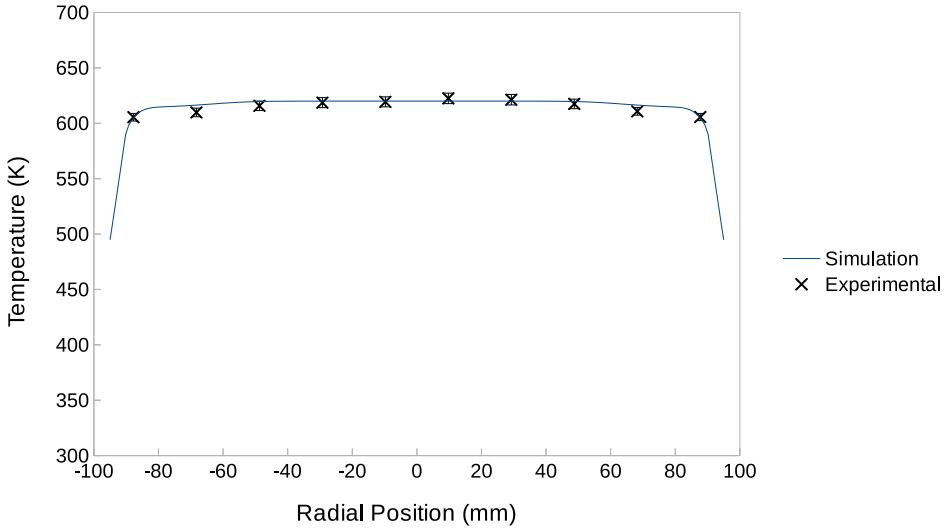

(a) No Insulation Ring

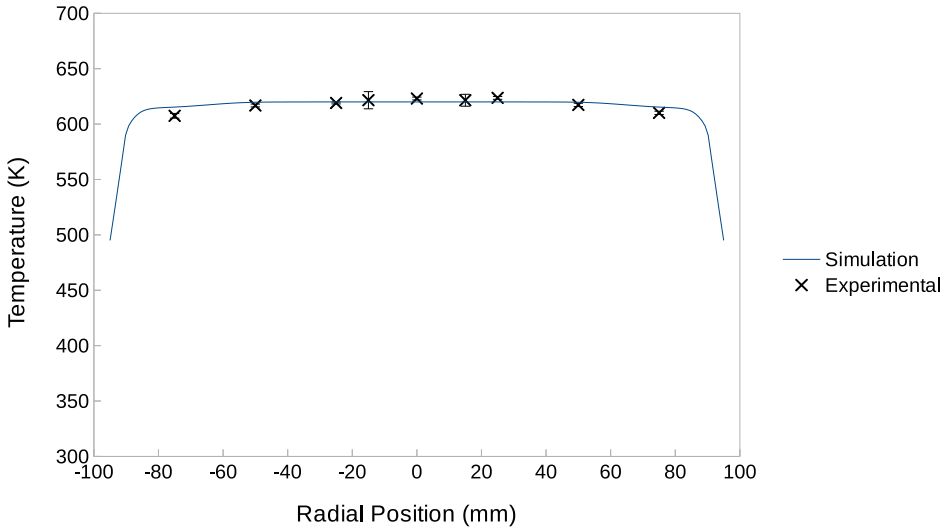

(b) Small Ring at r = 20.5-23 mm

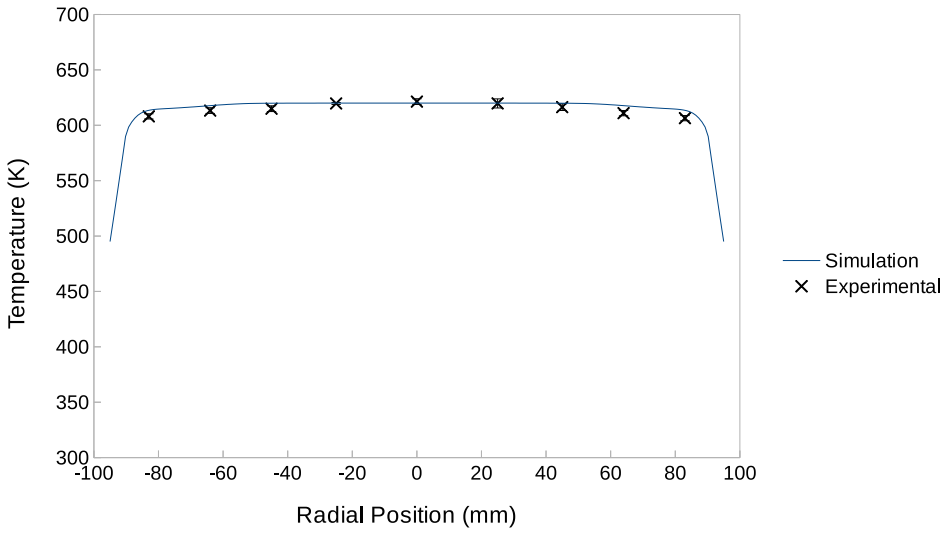

(c) Medium Ring at r = 32.5-35 mm

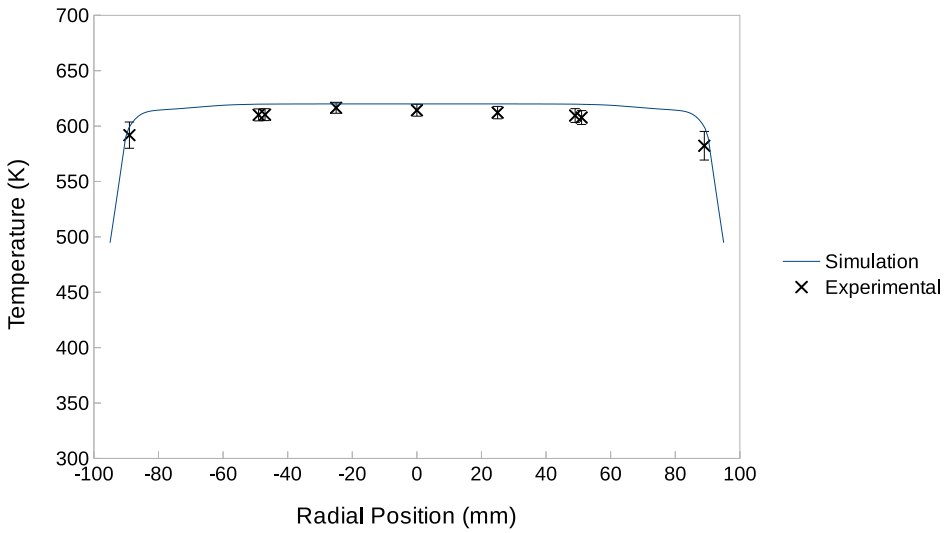

(d) Large Ring at r = 49.5-52 mm

Figure 6.3: Radial temperature profile of the downstream side of the DOC monolith

Comparing the steady state temperature profiles of the four DOC configurations, shown in Figure 6.4, it can be seen that the insulation ring increases the temperature of the monolith 50 to 75 mm from the centre of the monolith without decreasing the temperature at the centre of the DOC. The higher temperature in the radial portions of the DOC due to the addition of the insulation ring illustrates the ability of the

insulation ring to reduce the heat transfer from the DOC. Reducing the heat transfer from the DOC and maintaining a higher temperature towards the centre of monolith will help improve the light-off characteristics of the DOC during low load operation or periods of time when the engine is turned off for short time intervals. With vehicles automatically stopping the engine whenever the vehicle stops, maintaining the catalyst above the light-off for longer will decrease the overall emissions produced.

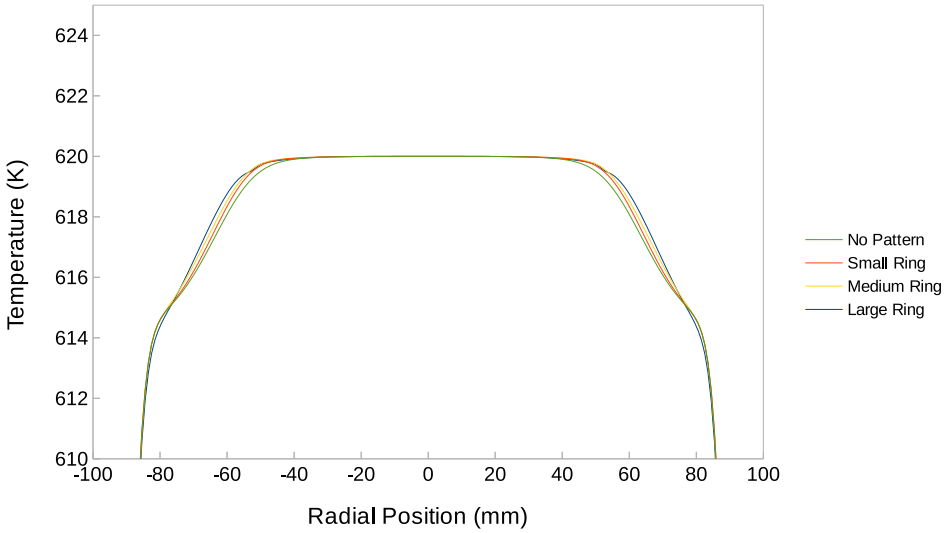

Figure 6.4: Monolith temperature profile for each of the four DOC configurations

6.2 Transient Numerical Model

The heating characteristics of the DOC were examined by developing a numerical model with a step in the temperature input. This section details the time-dependent temperature input and the ability of the numerical model to predict the DOC temperature response.

6.2.1 Temperature Input

The setup of the numerical analysis used the same parameters as the steady state analysis with the exception of the inlet temperature, which was varied using a user-

defined variable input temperature. The following sigmoidal function was used,

$$T_{\text{inlet}} = \begin{cases} 288 \text{ K } + 300 \text{ K } \frac{1}{1+2.2^{-t+5}} & t \leq 20 \text{ s} \\ 590 \text{ K} & t > 20 \text{ s} \end{cases} \tag{6.1}$$

where T_{inlet} is the exhaust inlet temperature in Kelvin and t is the time step in seconds. The inlet temperature starts at 303 K and increases to 590 K in the first 20 time steps and then remains constant at 590 K for the remaining time steps, as shown in Figure 6.5, and is compared with the experimental step in inlet temperature measured just upstream of the DOC for the operating point 1950 rpm and 450 ft-lbs for a flow rate of 176.0 ± 25.5 g/s (see Section 3.6).

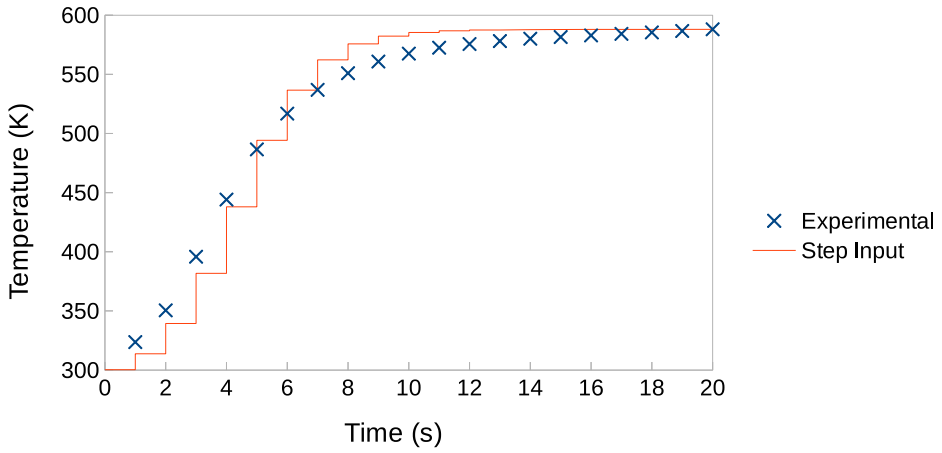

Figure 6.5: Inlet temperature of the exhaust gas used in the numerical analysis

6.2.2 Transient Model Validation

The heating characteristics predicted by the numerical model for each of the four DOC configurations are shown in Figures 6.6. The heating profile demonstrates that the DOC undergoes the highest rate of temperature increase at the centre of the monolith with the rate of heating decaying with increasing radial distance. The insulating ring reduces the rate of heating adjacent to the ring and shown in Figures 6.6b to 6.6d. The

decreased rate of heating next to the insulation ring is expected as the flow directly adjacent to the insulation is reduced (as shown in Figure 6.1) and the thermal capacity of the ceramic ring is higher than the remainder of the monolith requiring a greater amount of energy to reach steady state.

The numerical model is generally able to predict the heating characteristics of the monolith, showing the same steady state temperature and approximately the same heating profile as the experimental results. The numerical model however underestimates the time required for the monolith to reach the steady state temperature, showing a much faster rate of heating than the experimental data. As the numerical model shows a similar profile to the experimental data, the discrepancy is likely due to incorrectly estimating one of the following parameters:

- bulk density of the monolith
- heat capacity of the exhaust
- thermal conductivity of the exhaust

The material properties of the monolith, as listed in Table 4.3, were commonly accepted values for DOC modeling. Improving the numerical model could be accomplished by confirming and correcting the values of the material properties used in the numerical model.

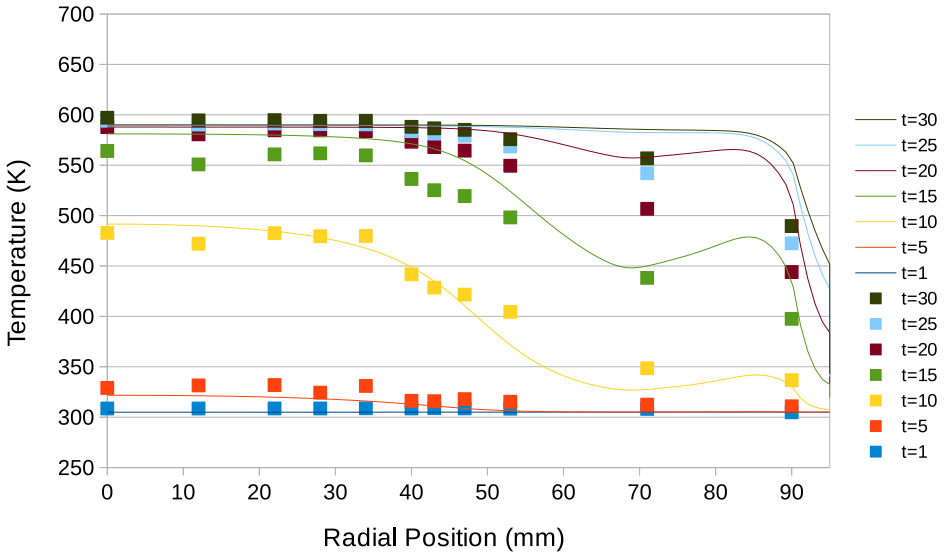

(a) No Insulation Ring

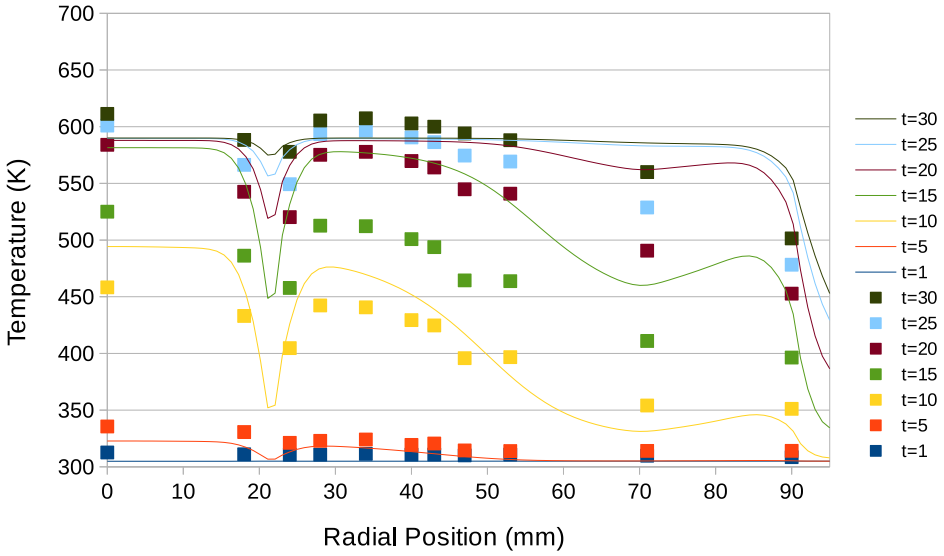

(b) Small Ring at r = 20.5-23 mm

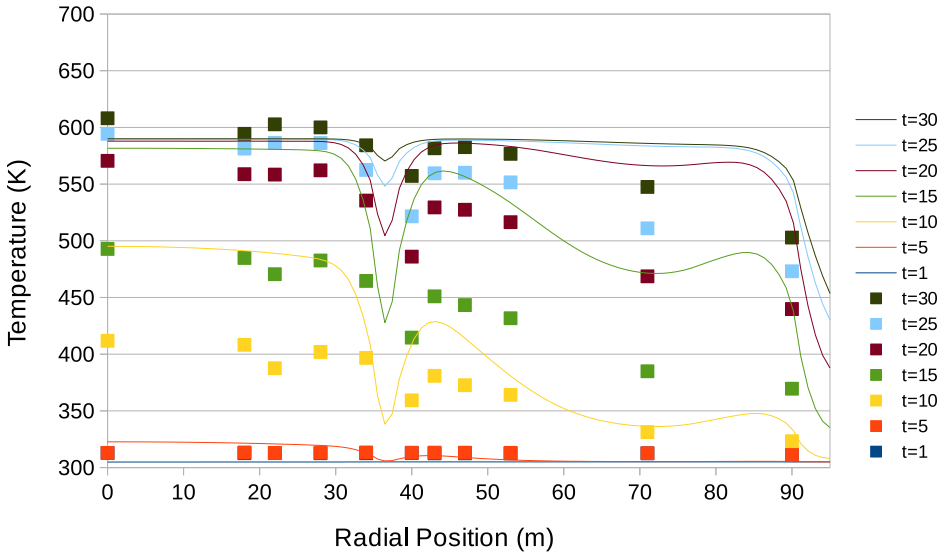

(c) Medium Ring at r = 32.5-35 mm

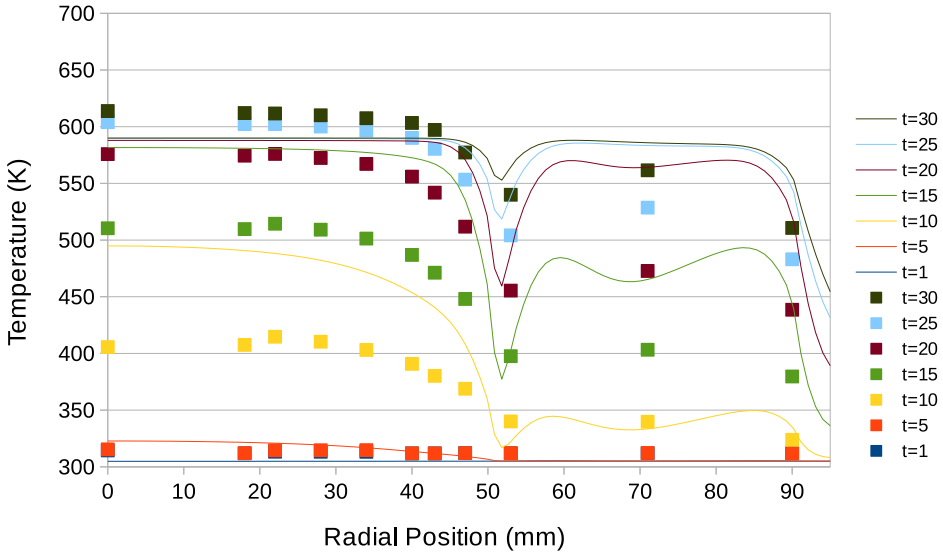

(d) Large Ring at r = 49.5-52 mm

Figure 6.6: Heating characteristics of the DOC monolith

Overall, the ability of the numerical model to predict the transient temperature of the monolith is sufficient for a simple model of the DOC. The ability to use commercial software to obtain good results allows for the optimization of the DOC without requiring each DOC to be tested experimentally.

6.2.3 DOC Heating Characteristics

The heating characteristics of each of the four DOC configurations is important in understanding the effect the insulation ring has on the light-off characteristics. The heating characteristics of the four DOC configurations are shown in Figure 6.7, comparing the temperature of each of the four DOC configurations at 5 s, 10 s, 15 s, and 20 s after the beginning of the step in inlet temperature described in Section 6.2.1.

The addition of an insulation ring shows a reduced temperature adjacent to and within the insulation ring due to the higher heat capacity of the ceramic requiring a greater amount of time for the insulation ring to reach the same temperature as the remainder of the monolith. Despite this decrease in temperature it is interesting to note that the remainder of the monolith heats at a greater rate if an insulation ring is present, which can be seen in both Figures 6.7b and 6.7c.

An increase in the rate of heating due to the addition of an insulating ring occurs at both the centre and radial portions of the DOC. The center of the DOC containing any of the three sizes of insulation ring reaches a temperature of approximately 4 K higher than the DOC containing no insulation ring after 10 s of heating (shown in Figure 6.7b) while the radial portion of the DOC reaches a temperature of up to 20 K higher after 15 s of heating (Figure 6.7c).

The steady state temperature of the DOC is approximately the same with a small increase in temperature in the radial portion of the DOC, as discussed in Section 6.1.4. The temperature of the ceramic ring and the channels directly adjacent however require a much longer time to reach steady state, which is expected due to the higher heat capacity of the ceramic ring and the decreased flow adjacent to the ceramic ring as discussed in Section 6.1.2. The overall ability of the insulation ring to reduce the light-off time of the monolith when both the increase in heating of the centre and radial portions of the monolith is combined with the decrease in temperature next to

the ceramic ring are combined needs to be further examined.

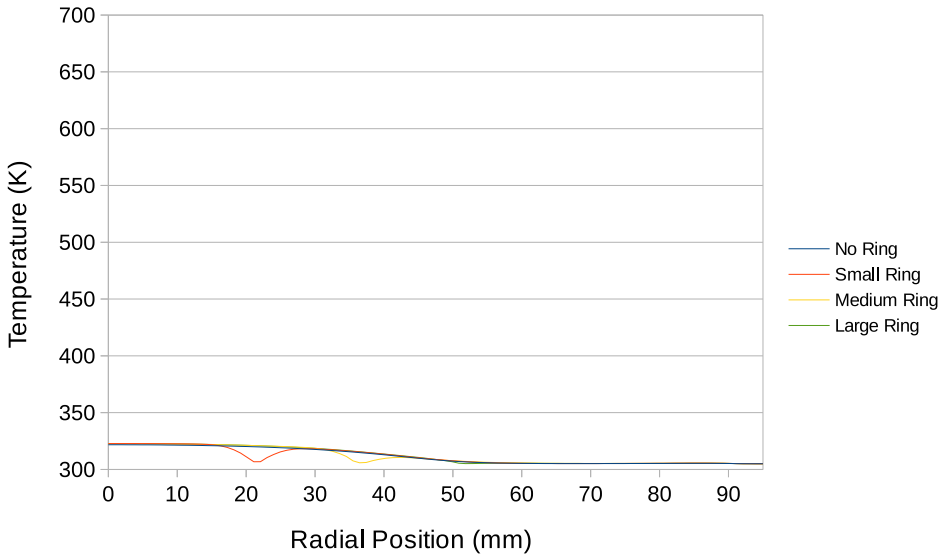

(a) t = 5 s

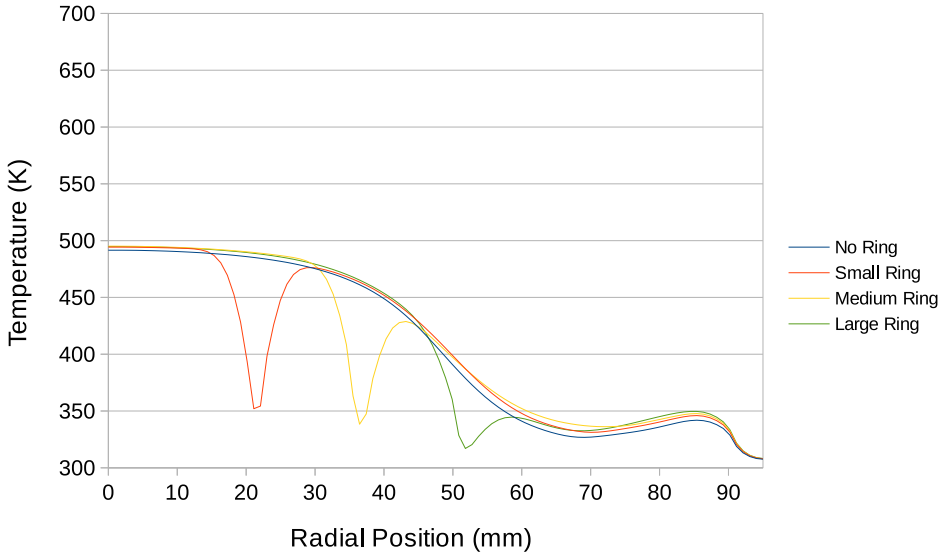

(b) t = 10 s

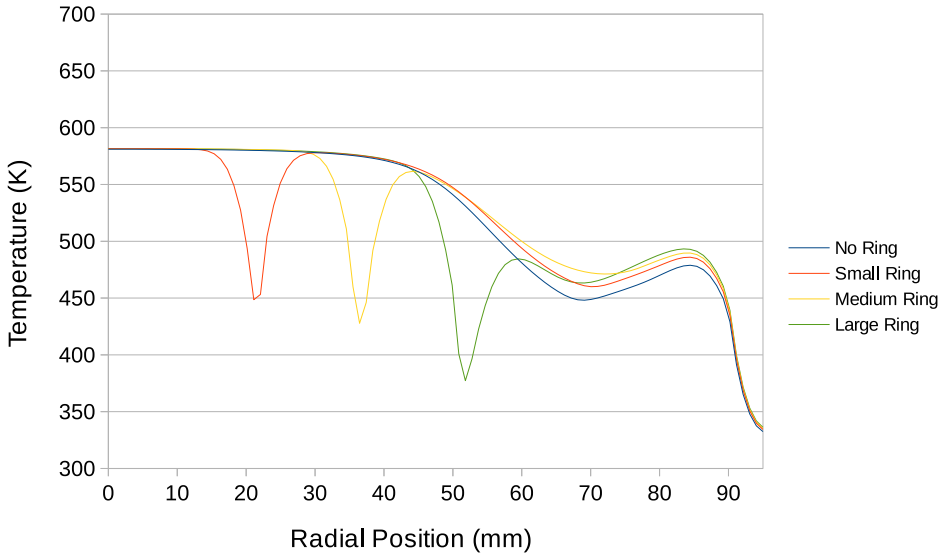

(c) t = 15 s

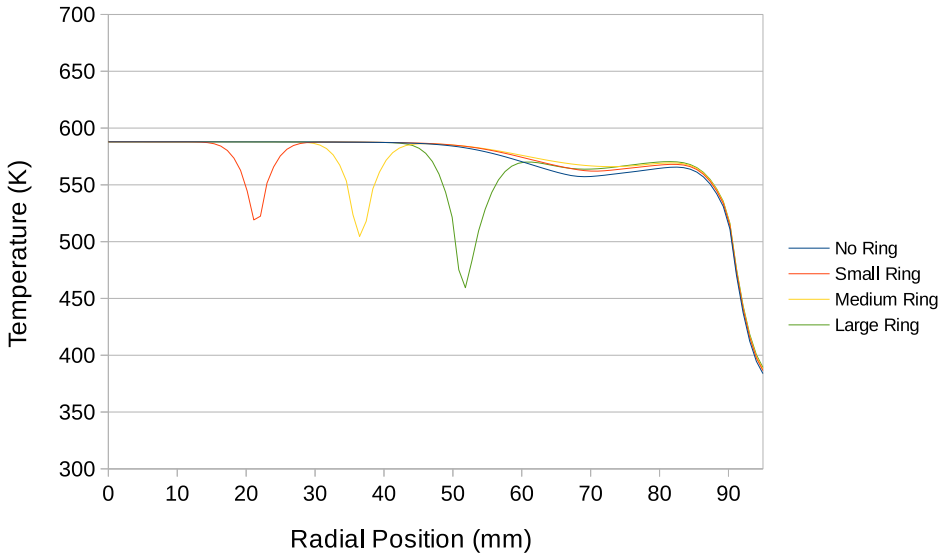

(d) t = 20 s

Figure 6.7: Comparison of the heating characteristics of the four DOC configurations

6.3 Assumptions and Limitations

The numerical model is based on assumptions that allow it to be applied easily. These simplifications however limit the conditions to which the model can be applied.

A limiting assumption used in the numerical model is that the material properties of the DOC and the exhaust gas were considered constant. This decreases the accuracy of the transient numerical model where the temperature varies between 300 and 600 K resulting in material properties that can change by up to 30%. As the material properties were selected for temperatures between 500 and 600 K, it is important to understand that the results will be adversely affected by error introduced in assuming constant properties.

The material properties are estimated using data found in the literature and approximating the exhaust gases from a Diesel engine as air at the desired temperature. Determining the exact properties of the monolith is difficult as it is constructed of extruded cordierite for which the material properties can vary depending on the manufacturing conditions.

The model uses a standard k-omega SST turbulence model and assumes that the flow through the monolith is laminar. The accuracy of the turbulence model in the inlet diffuser is currently assumed to be sufficient, however the effects of turbulence have an effect on the pressure drop and temperature profile in the monolith. Determining the accuracy of the turbulence model and the validity of the laminar flow assumption will further add to the accuracy of the numerical model.

Finally, the monolith in the numerical model does not contain a washcoat or active catalyst. This allows for optimization of the flow through the catalyst by separating the effects of the geometry from chemical reactions but limits the numerical model. Furthermore, the chemical reactions have the ability to change the flow characteristics by increasing or decreasing the pressure drop as the the exhaust chemical composition changes.

Chapter 7

Conclusions

Conclusions for experimental and numerical results are presented here along with recommendations for future work is detailed.

7.1 Pressure Drop

The experimental results were unable to show a statistically significant difference in pressure drop between the DOC without an insulation ring and the DOC configurations containing an insulation ring. Due to the variability of the results, caused primarily from the pulsations in the exhaust flow, the uncertainty in the pressure drop was large while the expected differences are expected to be small, as was shown with the numerical model which indicated a difference of only 1 kPa.

The numerical model was only able to calculate a pressure drop to within 30% of the experimental pressure drop. The pressure drop is dependent on the viscous resistance factor as well as the density and viscosity of the exhaust gas. The viscous resistance was calculated analytically from Poisseuille's law and provided the best estimate of the viscous resistance. Despite a larger pressure drop than the experimental results, the numerical model demonstrated that the addition of an insulation ring tended to increase the pressure drop and captured the same trend as the experiment. The pressure drop was not directly proportional to the decrease in flow area

with the large insulation ring showing a lower pressure drop than the medium insulation ring. This is likely due to the lower flow rate through the individual channels in the radial portions of the monolith.

7.2 Temperature Profile

The steady state temperature profile of the DOC was found experimentally and showed a symmetrical profile across the monolith. The steady state temperature showed a decaying temperature profile with the highest temperature found at the centre of the monolith and the lowest temperature at the wall of the DOC. This is expected as the highest flow rate of exhaust gases per unit area is expected at the centre of the monolith and the heat is dissipated at the wall of the DOC. The experimental results indicate that the time required for the monolith to reach its steady state temperature is increased with the addition of an insulation ring. This has the potential of increasing the time required by the DOC to reach light-off, increasing the pollutants emitted.

The numerical model showed a similar profile to the experimental results further validating the model. The numerical model showed a similar decay in temperature from the centre of the monolith to the DOC walls, with an increased drop in the temperature close to the DOC wall. Although the experimental tests indicated that the addition of an insulation ring increased the time for the DOC to reach steady state, the numerical model indicated that although true, the increase in time is associated with the increased time for the ceramic ring to heat to steady state with the remainder of the monolith heating faster. The benefit of the insulation ring to reducing the time required for the DOC to reach light-off needs to be determined as there is a decrease in temperature directly adjacent to the insulation ring which has the potential of offsetting the benefits.

The experimental transient temperature profile showed a non-uniform rate of heating with two maximums between the centre of the monolith and the wall of the DOC. The first peak was at the centre of the monolith while the second peak was approximately 30 mm from the centre. The second peak corresponds approximately to the radius of the inlet to the diffuser and is likely the result of flow maldistribution caused by the inlet diffuser. The addition of the insulation ring results in a drop in heating rate adjacent to the insulation ring with the temperature recovering as the monolith reaches steady state.

The transient numerical model showed similarities to the experimental results apart from the differences in the rate of heating. The rate of heating in the numerical model was greater than the experimental results showed and is likely the result of underestimating the bulk density of the monolith or the heat capacity of the exhaust.

7.3 Insulation Ring

Under the current experimental setup, the results showed no statistical difference in pressure drop between the DOC configurations as the variation in the data associated with the setup, primarily from pulsations in the exhaust flow, was greater than the expected difference in pressure drop. The numerical model indicates that the expected difference in pressure drop between the DOC configurations is approximately 1 kPa, with the addition of an insulation ring increasing the pressure drop.

The numerical model indicates the ability of the insulation ring to maintain the heat within the monolith and decrease the time required to reach light-off. The increased time for the DOC to reach steady state shown in the experimental tests is shown by the numerical model to be a result of the insulation ring requiring a greater time to reach steady state. Although the numerical model indicates that the majority of the monolith heats faster with the addition of an insulation ring, the area directly

adjacent to the insulation ring shows a slower rate of heating. The combined effect of the slower heating adjacent to the insulation ring and the increased rate of heating throughout the remainder of the monolith needs to be determined.

7.4 Future Work

- Testing of the four DOC configurations on an improved experimental setup that eliminates the pressure fluctuations in the exhaust flow to determine the effect of adding an insulation ring on the pressure drop.
- Determine whether the insulation ring decreases the time required for the DOC to reach light-off by measuring the exhaust composition after a step in inlet temperature downstream of the DOC.
- Investigate the differences between various DOC geometries, including the angle of the inlet diffuser and outlet nozzle.
- Demonstrate that numerical models of the DOC without an active catalyst is a valid simplification for DOC flow optimization.
- Improvement of the numerical model to the effects of turbulence in the inlet diffuser and verification of the laminar flow assumption in the monolith.
- Testing of the DOC with an active catalyst to determine the validity of using models containing no catalyst to characterize the flow of exhaust gases through the DOC.

References

Andersson, B., Andersson, R., Håkansson, L., Mortensen, M., Sudiyo, R., and Van Wachem, B. (2012). *Computational fluid dynamics for engineers*. Cambridge University Press, 1 edition.

Andrews, G. E., Ahamed, F. M., and Li, H. (2007). Condensable and Gaseous Hydrocarbon Emissions and Their Speciation for a Real World SI Car Test. Technical report, SAE Technical Paper.

ANSYS, Inc. (2006). *FLUENT 6.3 Users Guide*. ANSYS, Inc., 275 Technology Drive, Canonsburg, PA 15317, 6.3 edition.

Barbosa, F. C. (2016). Heavy Duty Emission Standards Assessment-An Engine and Aftertreatment Technological Approach. Technical report, SAE Technical Paper.

Bartley, G. J. (2015). Identifying Limiters to Low Temperature Catalyst Activity. Technical report, SAE Technical Paper.

Bond, T. C. and Bergstrom, R. W. (2006). Light absorption by carbonaceous particles: An investigative review. *Aerosol science and technology*, 40(1):27–67.

Bond, T. C., Doherty, S. J., Fahey, D., Forster, P., Berntsen, T., DeAngelo, B., Flanner, M., Ghan, S., Kärcher, B., Koch, D., et al. (2013). Bounding the role of black carbon in the climate system: A scientific assessment. *Journal of Geophysical Research: Atmospheres*, 118(11):5380–5552.

Bowman, C. T. (1975). Kinetics of pollutant formation and destruction in combustion. *Progress in energy and combustion science*, 1(1):33–45.

Cappa, C. D., Onasch, T. B., Massoli, P., Worsnop, D. R., Bates, T. S., Cross, E. S., Davidovits, P., Hakala, J., Hayden, K. L., Jobson, B. T., et al. (2012). Radiative absorption enhancements due to the mixing state of atmospheric black carbon. *Science*, 337(6098):1078–1081.

Carpenter, L., Clemitshaw, K., Burgess, R., Penkett, S., Cape, J., and McFadyen, G. (1998). Investigation and evaluation of the NOx/O3 photochemical steady state. *Atmospheric Environment*, 32(19):3353–3365.

Cavataio, G., Girard, J., Patterson, J. E., Montreuil, C., Cheng, Y., and Lambert, C. K. (2007). Laboratory testing of urea-SCR formulations to meet tier 2 bin 5 emissions. Technical report, SAE Technical Paper.

Cengel, Y. A. and Boles, M. A. (2011). *Thermodynamics: an engineering approach*. McGraw-Hill.

Chakravarthy, V., Conklin, J., Daw, C., and DAzevedo, E. (2003). Multi-dimensional simulations of cold-start transients in a catalytic converter under steady inflow conditions. *Applied Catalysis A: General*, 241(1):289–306.

Chen, P., Ibrahim, U., and Wang, J. (2014). Experimental investigation of diesel and biodiesel post injections during active diesel particulate filter regenerations. *Fuel*, 130:286–295.

Cho, Y.-S., Kim, D.-S., Han, M., Joo, Y., Lee, J.-H., and Min, K.-D. (1998). Flow distribution in a close-coupled catalytic converter. Technical report, SAE Technical Paper.

Clague, A., Donnet, J., Wang, T., and Peng, J. (1999). A comparison of diesel engine soot with carbon black. *Carbon*, 37(10):1553–1565.

Cornejo, I., Nikrityuk, P., and Hayes, R. (2017). Turbulence Decay Inside the Channels of an Automotive Catalytic Converter Monolith. *Emission Control Science and Technology*, pages 1–8.

Deissler, R. G. (1998). *Turbulent fluid motion*. CRC Press.

Dhal, G. C., Mohan, D., and Prasad, R. (2017). Preparation and application of effective different catalysts for simultaneous control of diesel soot and NOx emissions: An overview. *Catalysis Science & Technology*, 7(9):1803–1825.

Dyne Systems (2014). MW-1014W/Engine Dynamometer. Available at `http://dynesystems.com/wp-content/uploads/pdfs/DS2325-MW-1014W.pdf` (2017/12/11).

Ebrahimi, K. and Koch, C. (2015). Model predictive control for combustion timing and load control in hcci engines. Technical report, SAE Technical Paper.

EPA (2012). 2017 and Later Model Year Light-Duty Vehicle Greenhouse Gas Emissions and Corporate Average Fuel Economy Standards. Regulatory Announcement, EPA-HQ-OAR-2010-0799;FRL-9706-5;NHTSA-2010-0131.

Ford Motor Company (2014). 2015 MY OBD System Operation Summary for Diesel Engines. Available at `http://www.fordservicecontent.com/ford_content/catalog/motorcraft/DOBDSM1501.pdf` (2017/31/10).

Fox, R. W. and Kline, S. (1962). Flow regimes in curved subsonic diffusers. *Journal of Basic Engineering*, 84(3):303–312.

Ghazi, R. and Olfert, J. (2013). Coating mass dependence of soot aggregate restructuring due to coatings of oleic acid and dioctyl sebacate. *Aerosol Science and Technology*, 47(2):192–200.

Ghazimirsaied, A. and Koch, C. R. (2012). Controlling cyclic combustion timing variations using a symbol-statistics predictive approach in an HCCI engine. *Applied energy*, 92:133–146.

Goralski, C. T. and Chanko, T. (2001). Modeling the effect of substrate cell shape on conversion in monolith catalysts. Technical report, SAE Technical Paper.

Hadavi, S. A., Li, H., Andrews, G., Dizayi, B., Khalfan, A., et al. (2013). Diesel Cold Start into Congested Real World Traffic: Comparison of Diesel, B50, B100 for Gaseous Emissions. Technical report, SAE Technical Paper.

Hayes, R., Fadic, A., Mmbaga, J., and Najafi, A. (2012). CFD modelling of the automotive catalytic converter. *Catalysis today*, 188(1):94–105.

Hayes, R., Rojas, A., and Mmbaga, J. (2009). The effective thermal conductivity of monolith honeycomb structures. *Catalysis Today*, 147:S113–S119.

Hernández, J., Pérez-Collado, J., and Sanz-Argent, J. (2007). Role of the chemical kinetics on modeling NOx emissions in diesel engines. *Energy & Fuels*, 22(1):262–272.

Heywood, J. B. et al. (1988). *Internal combustion engine fundamentals*, volume 930. Mcgraw-hill New York.

Hilliard, J. C. and Wheeler, R. W. (1979). Nitrogen dioxide in engine exhaust. Technical report, SAE Technical Paper.

Holmgren, A. and Andersson, B. (1998). Mass transfer in monolith catalysts–CO oxidation experiments and simulations. *Chemical engineering science*, 53(13):2285–2298.

Holmgren, A., Grönstedt, T., and Andersson, B. (1997). Improved flow distribution in automotive monolithic converters. *Reaction Kinetics and Catalysis Letters*, 60(2):363–371.

Jeong, S.-J. and Kim, W.-S. (1998). A numerical approach to investigate transient thermal and conversion characteristics of automotive catalytic converter. Technical report, SAE Technical Paper.

Karvounis, E. and Assanis, D. N. (1993). The effect of inlet flow distribution on catalytic conversion efficiency. *International journal of heat and mass transfer*, 36(6):1495–1504.

Katsouyanni, K., Touloumi, G., Spix, C., Schwartz, J., Balducci, F., Medina, S., Rossi, G., Wojtyniak, B., Sunyer, J., Bacharova, L., et al. (1997). Short term effects of ambient sulphur dioxide and particulate matter on mortality in 12 European cities: results from time series data from the APHEA project. *Bmj*, 314(7095):1658.

Kline, S. and Johnston, J. (1986). Diffusers: flow, design, and performance prediction, Part 1: Diffuser-flow phenomena and design. *Advanced topics in turbomachinery technology*.

Konstandopoulos, A. G., Kostoglou, M., Skaperdas, E., Papaioannou, E., Zarvalis, D., and Kladopoulou, E. (2000). Fundamental studies of diesel particulate filters: transient loading, regeneration and aging. Technical report, SAE Technical Paper.

Kotrba, A., Gardner, T. P., Bai, L., and Yetkin, A. (2013). Passive regeneration response characteristics of a DPF system. Technical report, SAE Technical Paper.

Künzli, N., Kaiser, R., Medina, S., Studnicka, M., Chanel, O., Filliger, P., Herry, M., Horak, F., Puybonnieux-Texier, V., Quénel, P., et al. (2000). Public-health impact of outdoor and traffic-related air pollution: a European assessment. *The Lancet*, 356(9232):795–801.

Leung, K. K., Schnitzler, E. G., Dastanpour, R., Rogak, S. N., Jager, W., and Olfert, J. S. (2017). Relationship between Coating-Induced Soot Aggregate Restructuring and Primary Particle Number. *Environmental Science & Technology*, 51(15):8376–8383.

Litto, R., Mmbaga, J. P., Hayes, R., Plati, S., Blagojevic, V., et al. (2016). Exhaust emissions and fuel economy improvements through thermal performance control in a novel three-way catalytic converter. *The Canadian Journal of Chemical Engineering*, 94:905–912.

MacMillan, D. J., Law, T., Shayler, P. J., and Pegg, I. (2012). The influence of compression ratio on indicated emissions and fuel economy responses to input variables for a DI diesel engine combustion system. Technical report, SAE Technical Paper.

Manente, V., Johansson, B., and Cannella, W. (2011). Gasoline partially premixed combustion, the future of internal combustion engines? *International Journal of Engine Research*, 12(3):194–208.

Martin, A., Will, N., Bordet, A., Cornet, P., Gondoin, C., and Mouton, X. (1998). Effect of flow distribution on emissions performance of catalytic converters. Technical report, SAE Technical Paper.

Mazda (2017). Mazda Announces Long-Term Vision for Technology Development, 'Sustainable Zoom-Zom 2030'. Available at `http://www2.mazda.com/en/publicity/release/2017/201708/170808a.html` (2017/27/11).

Merryman, E. L. and Levy, A. (1975). Nitrogen oxide formation in flames: the roles of NO2 and fuel nitrogen. In *Symposium (international) on combustion*, volume 15, pages 1073–1083. Elsevier.

Mladenov, N., Koop, J., Tischer, S., and Deutschmann, O. (2010). Modeling of transport and chemistry in channel flows of automotive catalytic converters. *Chemical Engineering Science*, 65(2):812–826.

Moffat, R. J. (1988). Describing the uncertainties in experimental results. *Experimental thermal and fluid science*, 1(1):3–17.

Muilwijk, C., Schrijvers, P., Wuerz, S., and Kenjereš, S. (2016). Simulations of photochemical smog formation in complex urban areas. *Atmospheric Environment*, 147:470–484.

Nishiyama, H., Tanaka, Y., Adachi, T., Kawamura, S., Daisho, Y., Suzuki, H., Ishii, H., and Yamaguchi, K. (2015). A Study on the Improvement of NOx Reduction Efficiency for a Urea SCR System. Technical report, SAE Technical Paper.

Noehre, C., Andersson, M., Johansson, B., and Hultqvist, A. (2006). Characterization of partially premixed combustion. Technical report, SAE Technical Paper.

Ozhan, C., Fuster, D., and Da Costa, P. (2014). Multi-scale flow simulation of automotive catalytic converters. *Chemical Engineering Science*, 116:161–171.

Pachauri, R. K., Allen, M. R., Barros, V. R., Broome, J., Cramer, W., Christ, R., Church, J. A., Clarke, L., Dahe, Q., Dasgupta, P., et al. (2014). *Climate change 2014: synthesis report. Contribution of Working Groups I, II and III to the fifth assessment report of the Intergovernmental Panel on Climate Change*. IPCC.

Pope III, C. A. and Dockery, D. W. (2006). Health effects of fine particulate air

pollution: lines that connect. *Journal of the air & waste management association*, 56(6):709–742.

Price, P., Stone, R., Misztal, J., Xu, H., Wyszynski, M., Wilson, T., and Qiao, J. (2007). Particulate emissions from a gasoline homogeneous charge compression ignition engine. Technical report, SAE Technical Paper.

Russell, A. and Epling, W. S. (2011). Diesel oxidation catalysts. *Catalysis Reviews*, 53(4):337–423.

Shen, H., Shamim, T., and Sengupta, S. (1999). An investigation of catalytic converter performances during cold starts. Technical report, SAE Technical Paper.

Shum-Kivan, F., Santiago, J. M., Verdier, A., Riber, E., Renou, B., Cabot, G., and Cuenot, B. (2016). Experimental and numerical analysis of a turbulent spray flame structure. *Proceedings of the Combustion Institute*, 36:2567–2575.

Stone, R. (2012). *Introduction to internal combustion engines*. Palgrave Macmillan, 4 edition.

Strandh, P., Bengtsson, J., Johansson, R., Tunestål, P., and Johansson, B. (2004). Cycle-to-cycle control of a dual-fuel hcci engine. Technical report, SAE Technical Paper.

Valério, M., Raggi, K., and Sodré, J. R. (2003). Model for Kinetic Formation of CO Emissions in Internal Combustion Engines. Technical report, SAE Technical Paper.

Warsi, Z. U. (2005). *Fluid dynamics: theoretical and computational approaches*. CRC press.

Watling, T. C., Ahmadinejad, M., Ţuţuianu, M., Johansson, Å., and Paterson, M. A. (2012). Development and validation of a Pt-Pd diesel oxidation catalyst model. *SAE International Journal of Engines*, 5(2012-01-1286):1420–1442.

WHO (2006). *Air Quality Guidelines: Global Update 2005. Particulate Matter, Ozone, Nitrogen Dioxide and Sulfur Dioxide*. World Health Organization.

WHO, W. H. O. et al. (2012). *Health effects of black carbon*. WHO.

Wilcox, D. C. (2010). *Turbulence modeling for CFD*. DCW Industries La Canada, CA, 3 edition.

Yao, M., Zheng, Z., and Liu, H. (2009). Progress and recent trends in homogeneous charge compression ignition (HCCI) engines. *Progress in Energy and Combustion Science*, 35(5):398–437.

Yunus, A. C. and Cimbala, J. M. (2006). Fluid mechanics fundamentals and applications. *International Edition, McGraw Hill Publication*, 185201.

Appendix A

CFD Background

A description of the differential equations, constants, and solution methods used by ANSYS Fluent.

A.1 Turbulent Flow

Modeling of the DOC has become an increasingly popular area of research for two reasons: computers have become capable of solving complex flows in reasonable lengths of time and flow optimization through the DOC is becoming a requirement to meet emissions regulations. As the maximum velocity in the DOC gives a Mach number of approximately 0.3, the flow can be considered to be incompressible. Numerical analysis of the flow involves solving the continuity and momentum equations, given as (respectively),

$$\frac{\partial u_i}{\partial x_j} = 0 \tag{A.1}$$

$$\frac{\partial u_i}{\partial t} + u_j \frac{\partial u_i}{\partial x_j} = -\frac{1}{\rho}\frac{\partial p}{\partial x_i} + \nu \frac{\partial^2 u_i}{\partial x_j \partial x_j} \tag{A.2}$$

Because solving Equation A.2 at every scale is not feasible for most turbulent flows

with the current processing power of computers, Reynolds averaging is applied to Equation A.2. This is possible because at the smallest scales, turbulence is considered to be ergodic rather then deterministic. Through averaging, the smallest scales can be eliminated without affecting the results of the overall bulk motion of the fluid. Reynolds averaging of Equation A.2 gives the Reynolds Averaged Navier Stokes (RANS) equation as [Andersson et al., 2012],

$$\frac{\partial \bar{u_i}}{\partial t} + \bar{u_j}\frac{\partial \bar{u_i}}{\partial x_j} = -\frac{1}{\rho}\frac{\partial}{\partial x_j}\left[\bar{p}\delta_{ij} + \mu\left(\frac{\partial \bar{u_i}}{\partial x_j} + \frac{\partial \bar{u_j}}{\partial x_i}\right) - \rho\overline{u_i{}'u_i{}'}\right] \tag{A.3}$$

where $\bar{u}$ is the time-average velocity, u' is the fluctuating component of the velocity, μ is the dynamic viscosity, $\bar{p}$ is the time-average velocity, and δ is the Kronecker delta [Deissler, 1998]. The Reynolds stresses, given by $-\rho\overline{u_i{}'u_j{}'}$, introduces additional unknowns into the equation leading to the closure problem, a result of having more unknowns then equations. To find a solution to the problem, the Reynolds stresses need to be modeled. The most common method to close the equations is through the Boussinesq hypothesis, which postulates that the terms comprising the Reynolds stresses are proportional to the mean velocity components [Andersson et al., 2012]. The Boussinesq hypothesis suggest that the Reynolds stresses can be modeled using turbulent viscosity, as the momentum associated with the turbulence components is diffusive [Andersson et al., 2012]. The Boussinesq approximation is given by [Andersson et al., 2012],

$$-\overline{u_i{}'u_j{}'} = \nu_{\mathrm{T}}\left(\frac{\partial \bar{u_i}}{\partial x_j} + \frac{\partial \bar{u_j}}{\partial x_i}\right) - \frac{2}{3}k_{\mathrm{T}}\delta_{ij} \tag{A.4}$$

where k_{T} is half the trace of the Reynolds stress tensor, $k_{\mathrm{T}} = \frac{1}{2}\overline{u_i{}'u_j{}'}$ [Andersson

et al., 2012]. Finally, the kinematic turbulent viscosity needs to be specified to close the equations and determine a solution, the two-equation Shear-Stress Transport (SST) $k-\omega$ turbulence model expresses the dynamic turbulent viscosity in terms of the turbulent kinetic energy, k, and the specific dissipation rate, ω [Warsi, 2005]. Two equation models are able to calculate both k and the length scale of the flows [Wilcox, 2010]. For the $k-\omega$ model, k is computed directly while the length scale calculates ω which is related to the length scale, l, by $\omega = k/l^2$, known as the vorticity scale [Andersson et al., 2012; Wilcox, 2010]. This gives two-equation models the advantage of modeling turbulent flows without requiring prior information about the flow [Wilcox, 2010]. The SST portion of the equation builds from the standard $k-\omega$ model to blend the benefits obtained in using the $k-\omega$ model for calculations close to the wall with the benefits of the $k-\epsilon$ model in the free stream regions [Andersson et al., 2012]. Effectively, the $k-\omega$ model dominates the near-wall regions while the $k-\epsilon$ model dominates the freestream areas [Andersson et al., 2012]. The SST $k-\omega$ model is given by the following two equations,

$$\frac{\partial}{\partial t}(\rho k) + \frac{\partial}{\partial x_i}(\rho k u_i) = \frac{\partial}{\partial x_j}\left[\left(\mu + \frac{\mu_T}{\sigma_k}\right)\frac{\partial k}{\partial x_j}\right] + G_k - Y_k + S_k \tag{A.5}$$

$$\frac{\partial}{\partial t}(\rho \omega) + \frac{\partial}{\partial x_i}(\rho \omega u_i) = \frac{\partial}{\partial x_j}\left[\left(\mu + \frac{\mu_T}{\sigma_k}\right)\frac{\partial \omega}{\partial x_j}\right] + G_\omega - Y_\omega + D_\omega + S_\omega \tag{A.6}$$

where σ_k and σ_ω are the turbulent Prantl numbers, μ_{T} is the turbulent viscosity, G_k is the production of turbulent kinetic energy, G_ω is the production of the specific dissipation rate, Y_k is the dissipation of turbulent kinetic energy, Y_ω is the dissipation of the specific dissipation rate, D_ω is the cross-diffusion term, and S_k and S_ω are user-defined source terms.

A.1.1 Production of Turbulent Kinetic Energy, G_k

The production of turbulent kinetic energy, G_k, needs to be calculated to satisfy Equation A.5. The production of G_k can be calculated by the following,

$$G_k = -\rho\overline{u_i{}'u_j{}'}\frac{\partial u_j}{\partial x_i} \tag{A.7}$$

where $-\rho\overline{u_i{}'u_j{}'}$ is the Reynolds stresses as discussed in Section A.1. The Boussinesq hypothesis postulates that the Reynolds stresses are proportional to the mean velocities and that the transport of momentum is a diffusive process [Andersson et al., 2012]. Calculating G_k in a manner consistent with the Boussinesq hypothesis gives the following [Warsi, 2005],

$$G_k = \mu_t S^2 \tag{A.8}$$

where S is the modulus of the mean rate-of-strain tensor, defined as,

$$S \equiv \sqrt{2S_{ij}S_{ij}} \tag{A.9}$$

$$S_{ij} = \frac{1}{2}\left(\frac{\partial u_j}{\partial x_i} + \frac{\partial u_i}{\partial x_j}\right) \tag{A.10}$$

A.1.2 Production of Specific Dissipation Rate, G_ω

The production of ω is given by,

$$G_\omega = \frac{\alpha}{\nu_t} G_k \tag{A.11}$$

where α is given by,

$$\alpha = \frac{\alpha_\infty}{\alpha^*}\left(\frac{\alpha_0 + Re_t/R_\omega}{1 + Re_t/R_\omega}\right) \tag{A.12}$$

The variables that make up Equation A.12 are given as,

$$\alpha^* = {\alpha^*}_\infty\left(\frac{{\alpha^*}_0 + Re_t/R_k}{1 + Re_t/R_k}\right) \tag{A.13}$$

$$Re_t = \frac{\rho k}{\mu \omega} \tag{A.14}$$

$${\alpha_0}^* = \frac{\beta_i}{3} \tag{A.15}$$

$$\alpha_\infty = F_1 \alpha_{\infty,1} + (1 - F_1)\alpha_{\infty,2} \tag{A.16}$$

$$\alpha_{\infty,1} = \frac{\beta_{i,1}}{{\beta_\infty}^*} - \frac{\kappa^2}{\sigma_{\omega,1}\sqrt{{\beta_\infty}^*}} \tag{A.17}$$

$$\alpha_{\infty,2} = \frac{\beta_{i,1}}{{\beta_\infty}^*} - \frac{\kappa^2}{\sigma_{\omega,2}\sqrt{{\beta_\infty}^*}} \tag{A.18}$$

where $R_k = 6$, $\beta_i = 0.072$, $\kappa = 0.41$, $\sigma_{\omega,1} = 2$, $\sigma_{\omega,2} = 1.168$, $\beta_{\infty,1} = 0.075$, $\beta_{\infty,2} = 0.0828$, and ${\beta_\infty}^* = 0.09$.

A.1.3 Dissipation of Turbulent Kinetic Energy, Y_k

The dissipation of turbulent kinetic energy, Y_k, is calculated by

$$Y_k = \rho\beta^* k\omega \tag{A.19}$$

where,

$$\beta^* = {\beta_i}^*[1 + \zeta^* F(M_t)] \tag{A.20}$$

$${\beta_i}^* = {\beta_\infty}^* \left(\frac{4/15 + (Re_t/R_\beta)^4}{1 + (Re_t/R_\beta)^4} \right) \tag{A.21}$$

where $\zeta^* = 1.5$, $R_\beta = 8$, ${\beta_\infty}^* = 0.09$, and $F(M_t)$ is the compressibility function and is discussed in Section A.1.6.

A.1.4 Dissipation of Specific Dissipation Rate, Y_ω

The dissipation of specific dissipation rate, ω, is calculated by,

$$Y_\omega = \rho\beta\omega^2 \tag{A.22}$$

where,

$$\beta = \beta_i \left[1 - \frac{\beta_i^*}{\beta_i} \zeta^* F(M_t) \right] \tag{A.23}$$

$$\beta_i = F_1 \beta_{i,1} + (1 - F_1) \beta_{i,2} \tag{A.24}$$

$$F_1 = \tanh(\phi_1^4) \tag{A.25}$$

$$\phi_1 = min \left[max \left(\frac{\sqrt{k}}{0.09\omega y}, \frac{500\mu}{\rho y^2 \omega} \right), \frac{4\rho k}{\sigma_{\omega,2} {D_\omega}^+ y^2} \right] \tag{A.26}$$

$${D_\omega}^+ = max \left[2\rho \frac{1}{\sigma_{\omega,2}} \frac{1}{\omega} \frac{\partial k}{\partial x_j} \frac{\partial \omega}{\partial x_j}, 10^{-10} \right] \tag{A.27}$$

A.1.5 Compressibility Function, $F(M_t)$

The compressibility function used in Equations A.19 and A.22 is calculated by the following,

$$F(M_t) = \begin{cases} 0 & M_t \leq M_{t0} \\ {M_t}^2 - {M_{t0}}^2 & M_t > M_{t0} \end{cases} \tag{A.28}$$

where,

$${M_t}^2 \equiv \frac{2k}{a^2} \tag{A.29}$$

$$M_{t0} = 0.25 \tag{A.30}$$

$$a = \sqrt{\gamma R T} \tag{A.31}$$

A.1.6 Cross-Diffusion, D_ω

The SST $k-\omega$ model blends the benefits of the k-ω model with the k-ϵ model. The k-ω is susceptible to the freestream value of ω, and to reduce the sensitivity the cross-diffusion term is added [Wilcox, 2010]. The cross-diffusion term is given as,

$$D_\omega = 2(1-F_1)\rho\frac{1}{\omega\sigma_{\omega,2}}\frac{\partial k}{\partial x_j}\frac{\partial \omega}{\partial x_j} \tag{A.32}$$

A.2 Porous Flow

Flow through the monolith is normally simulated as flow through a porous zone. This is accomplished by adding a source term to the momentum equation, which is based on Forchheimer's modified formulation of Darcy's equation [Mladenov et al., 2010], and is given as,

$$\vec{S} = \left(\frac{\mu}{\alpha} + \frac{\rho C_2|\vec{u}|}{2}\right)\vec{u} \tag{A.33}$$

where $1/\alpha$ and C_2 are the viscous and inertial resistance factors. The viscous and inertial resistance factors can be easily calculated for a packed bed reactor using Ergun's formula [Mladenov et al., 2010], given as,

$$C_2 = \frac{3.5}{d_\mathrm{m}}\frac{(1-\epsilon)}{\epsilon^3} \tag{A.34}$$

$$\alpha = \frac{{d_\mathrm{m}}^2}{150}\frac{\epsilon^3}{(1-\epsilon)^2} \tag{A.35}$$

The validity of these equations is not well understood for use with the honeycomb

structure of the monolith. Empirical methods of determining the viscous and inertial terms are discussed in Section 4.6.

A.3 Heat Transfer

Exhaust gases exit the engine at between 400 K and 650 K, requiring the heat transfer from the DOC to the surroundings to be modeled to obtain accurate results. Heat transfer from the system is given by [Warsi, 2005],

$$\frac{\partial}{\partial t}(\rho E) + \nabla \cdot (\vec{u}(\rho E + p)) = \nabla \cdot \left(k_{eff} \nabla T - \sum_j h_j \vec{J}_j + (\bar{\bar{\tau}}_{eff} \cdot \vec{u}) \right) + S_h \qquad \text{(A.36)}$$

where k_{eff} is the effective conductivity and is equal to the sum of the heat transfer coefficient, k, and the turbulent heat transfer coefficient, k_t. The turbulent heat transfer coefficient can be approximated by the ratio of the product of the fluid specific heat, c_p, and turbulent viscosity, μ_t, to the turbulent Prandtl number, Pr_t. The effective thermal conductivity is then given by,

$$k_{eff} = k + \frac{c_p \mu_t}{Pr_t} \qquad \text{(A.37)}$$

The energy, E, in Equation A.36 is defined as,

$$E = h - \frac{p}{\rho} + \frac{u^2}{2} \qquad \text{(A.38)}$$

and for incompressible flows the pressure work and kinetic energy terms are not included in the simulation so that,

$$E = h = \sum_j Y_j h_j \tag{A.39}$$

$$h_j = \int_{T_{ref}}^{T} c_{p,j} dT \tag{A.40}$$

where h_j is the enthalpy of species j, Y_j is the mole fraction of species j, $c_{p,j}$ is the specific heat of species j, and T_{ref} is the reference temperature.

Appendix B

Uncertainty

A description of the method used to calculate uncertainty in the experimental results.

B.1 Theory

The error is defined as the difference between the true value and the measured value [Moffat, 1988]. Since the true value is almost never known, the uncertainty in the experimental value is calculated using standard statistical methods, where the measured value is used as a basis for defining a range in which the actual value may fall. The range represents the likelihood of containing the actual value with the probability typically being called the confidence level [Moffat, 1988].

For any measurement using any measurement system, the uncertainty is a combination of the bias and precision uncertainty. The bias uncertainty is the accuracy of the measurement device or the maximum expected error introduced by the device within a given confidence interval. the desired value and is usually small in comparison to the precision uncertainty where the precision uncertainty is the result of random error components that affect the measurement of the desired value, for example random changes in environmental conditions that result in an inability to exactly replicate the results from one test to the next [Moffat, 1988].

The precision uncertainty represents the random error components beyond the

error of the measuring device. For a measured variable, X_i, the precision uncertainty, δX_i, is calculated using the following,

$$\delta X_i = t\frac{S_x}{\sqrt{N}} \tag{B.1}$$

where t is the corresponding Student's t-distribution statistic, S_x is the sample standard deviation, and N is the number of samples [Moffat, 1988].

The overall uncertainty is calculated as the as the root sum of squares of the bias and precision uncertainty. In cases where the precision uncertainty is a minimum of an order of magnitude larger than the bias uncertainty, the overall uncertainty is taken simply as the precision uncertainty.

Using measured variables to further calculate parameters results in a need to propagate the uncertainty through the calculations. When the calculation involves a single measured variable, the uncertainty in the calculated variable, R_{X_i}, is calculated by [Moffat, 1988],

$$\delta R_{X_i} = \frac{\partial R}{\partial X_i}\delta X_i \tag{B.2}$$

For calculations involving multiple independent measured variables, the overall uncertainty, δR, is calculated by [Moffat, 1988],

$$\delta R = \left[\sum_{i=1}^{N}\left(\frac{\partial R}{\partial X_i}\delta X_i\right)^2\right]^{\frac{1}{2}} \tag{B.3}$$

where the contribution in uncertainty of each measured variable, δX_i, contributes to the overall uncertainty [Moffat, 1988].